SPARK IGNITION OF PARTIALLY STRATIFIED GASEOUS FUEL-AIR MIXTURES

by

Edward C. Chan

B.A.Sc., Systems Design Engineering, University of Waterloo, 1998
M.A.Sc., Mechanical Engineering, University of Waterloo, 2001

A THESIS SUBMITTED IN PARTIAL FULFILLMENT OF
THE REQUIREMENTS FOR THE DEGREE OF

DOCTOR OF PHILOSOPHY

in

The Faculty of Graduate Studies
(Mechanical Engineering)

THE UNIVERSITY OF BRITISH COLUMBIA

(Vancouver)

October, 2010

Abstract

The Partially Stratified Charge (PSC) strategy aims to stabilize the spark ignition of lean-burn natural gas fueled internal combustion engines. This results in an extension of unthrottled load control, as well as a reduction in regulated pollutant and carbon dioxide emissions. While engine experiments demonstrated the feasibility of this technology, its fundamental enabling mechanisms have yet to be identified.

An experimental / numerical approach was taken for the current investigation, using an idealized PSC ignition system. The PSC injection took place in a constant volume combustion chamber (CVCC) into an initially quiescent bulk mixture. A customized injection system was also developed. Experimental results indicated that stable combustion could be achieved with PSC at an air-to-fuel ratio of $\lambda = 2.0$. Furthermore, the use of double PSC injection facilitated additional consumption of the bulk fuel. The experiments also identified three primary enabling mechanisms under which PSC assists in ultra-lean spark ignited combustion.

Additional insights were provided through numerical modeling. The PSC jet was modeled using the standard $k-\epsilon$ model and was found to be in excellent agreement with the experimental results in terms of penetration and entrainment. Meanwhile, the Eddy Dissipation Concept (EDC) model was used to simulate the combustion under PSC. While the computational model lacked the ability to properly predict combustion rates in the turbulent-to-laminar flame transition, the ignition and early combustion phases were properly captured.

The numerical framework was applied to engine conditions, and the modeled data were validated using existing experimental results. A semi-analytical ignition model was developed using detailed chemical kinetic mechanisms. A turbulent ignition parameter was derived accordingly to characterize the likelihood of an ignition event leading to combustion. The engine simulation results also provided further information in PSC charge formation, as well as flame propagation. The results of this research gave rise to an improved design for future generation PSC injection / ignition devices.

Table of contents

List of tables

List of figures

Abbreviations

AFR	Air-to-fuel ratio [ ]
BMEP	Brake mean effective pressure [bar]
BSFC	Brake-specific fuel consumption [g/kWh]
CDI	Capacitive discharge ignition
CAD	Crank angle degree [°]
CERC	Clean Energy Research Centre
CFD	Computational fluid dynamics
CNG	Compressed natural gas
CoV	Coefficient of variations [ ]
CVCC	Constant volume combustion chamber
DNS	Direct numerical simulation
EDC	Eddy dissipation concept
EGR	Exhaust gas recirculation
EOI	End of injection [s]
FEA	Finite element analysis
HHV	Higher heating value [MJ/kg fuel]
ICE	Internal combustion engine
IMEP	Indicated mean effective pressure [bar]
LES	Large-eddy simulation
LHV	Lower heating value [MJ/kg fuel]
LML	Lean misfire limit
LPG	Liquefied petroleum gas
MFB	Mass fraction burnt [ ]
PLIF	Planar laser-induced fluorescence
PSC	Partially Stratified Charge
RANS	Reynolds-averaged Navier-Stokes
RPM	Revolutions per minute [rev/min]
SCRE	Single cylinder research engine
SD	Standard deviation
SOI	Start of injection [s]
TCI	Transistorized coil ignition
TDC	Top dead center [°]
UDF	User-defined function
UHC	Unburnt hydrocarbons
WOT	Wide open throttle

Nomenclature

Roman symbols

A	Arrhenius pre-exponential factor [1/s]
	Empirical constant for spark energy transfer efficiency [ ]
A_k	Flame kernel surface area [m^2]
a	Cut-off width (Schlieren) [m]
B	Luminance [candella/m^2]
$C_{\epsilon 1}$	Constant for the production of ϵ [ ]
$C_{\epsilon 2}$	Constant for the destruction of ϵ [ ]
C_μ	Constant for turbulent viscosity [ ]
c_p	Specific heat at constant pressure [J/kg·K]
c_V	Specific heat at constant volume [J/kg·K]
D_T	Turbulent diffusion coefficient [m^2/s]
E	Total fuel energy content [J]
	Edge graph
f_i	Focal length of optical element i [m]
f, g	Generic functions
H	Enthalpy [J]
h	Heat transfer coefficient [W/K·m^2]
	Height [m]
	Specific enthalpy [J/kg]
I	Illumination level [candella]
	Image space [ ]
I_0	Flame stretch factor [ ]
	Quiescent illumination level [candella]
i, j, k	Generic iterator indices [ ]
	Cartesian tensor components [ ]
k	Rate of reaction [1/s]
	Turbulent kinetic energy [m^2/s^2]
L	Length [m]
L_b	Markstein length [m]
L_e	Turbulent integral length scale [m]
L^*	Turbulent molecular length scale [m]
l_T	Turbulent Taylor microscale [m]

Roman symbols (continued)

M	Magnitude of image gradient [ ]
m	Image magnification factor [ ]
	Mass [kg]
$\dot{m}$	Mass flow rate [kg/s]
$\dot{m}^*$	Specific mass transfer among turbulent scales [1/s]
N	Sample size [ ]
n	Refractive index [ ]
p	Pressure [Pa]
p_0	Reference pressure [103.325 kPa]
Q	Combustion energy release [J]
Q_{sp}	Ignition energy [J]
Q_{ht}	Energy transferred as heat [J]
R	Specific gas constant [J/kg·K]
$\mathbb{R}$	Universal gas constant [8.314472 J/K·mol]
r_k	Flame kernel radius [m]
S	Sample standard deviation
S_b	Burning velocity [m/s]
S_L	Laminar flame speed [m/s]
S_p	Plasma expansion speed [m/s]
S_T	Developing turbulent flame speed [m/s]
T	Temperature [K]
T_0	Reference temperature [298.15 K]
T_{ad}	Adiabatic flame temperature [K]
T_f	Threshold for image feature [ ]
T_t	Threshold for image texture [ ]
t	Standardized random variable [ ]
	Time [s]
t_{inj}	Injection duration [s]
t_k	Flame kernel maturity period [s]
U	Internal energy [J]
U'	Turbulent ignition parameter [ ]
u	Velocity [m/s]
u'	Velocity fluctuation [m/s]
u''	Density (Favre) weighted velocity fluctuation [m/s]
u^*	Turbulent molecular velocity scale [m/s]
V	Volume [m^3]
V_k	Flame kernel volume [m^3]
$\dot{V}_{\text{fl}}$	Flame kernel expansion due to flame propagation alone [m^3/s]
w	Width [m]
X	Statistical random variable
x, y, z	Coordinate components [m]
$\boldsymbol{x}$	Generic vector variable
Y	Mass fraction [ ]

Greek symbols

α	Pressure-dependent correlation for flame speed
	Statistical level of significance
β	Temperature-dependent correlation for flame speed
γ	Ratios of specific heats [ ]
γ^*	Mass ratio between smallest and largest turbulent scales [ ]
δ_{ij}	Kronecker delta [ ]
δ_L	Laminar flame thickness [m]
ϵ	Dissipation rate of turbulent kinetic energy [m^2/s^3]
η	Efficiency [ ]
	Linear signal noise component [ ]
Θ	Direction of image gradient normal [rad]
κ	Flame stretch [ ]
λ	Relative air-to-fuel ratio [ ]
μ	Statistical mean [ ]
μ_T	Dynamic eddy viscosity [Pa·s]
ν	Kinetic viscosity [kg/m^2]
	Statistical degrees of freedom [ ]
ξ	Non-linear signal noise component [ ]
ϕ, φ	A generic scalar variable
ϕ	Equivalence ratio (relative fuel-to-air ratio) [ ]
ρ	Density [kg/m^3]
$\overline{\rho}$	Mean density [kg/m^3]
$\tilde{\rho}$	Change in density from ambient levels []
σ	Statistical standard deviation
σ_ϵ	Turbulent Prandtl number for ϵ [ ]
σ_k	Turbulent Prandtl number for k [ ]
τ	Characteristic combustion time scale [s]
χ	Fraction of reacting fine structures.
ω	Instrumentation uncertainty
	Frequency [rad/s]
$\dot{\omega}$	Reaction rate [kg/s]

Dimensionless numbers

Da	Damköhler number
Ka	Karlovitz number
M	Mach number
Le	Lewis number
Pr	Prandtl number
Re	Reynolds number
Sc	Schmidt number

Acknowledgments

This research would not be possible without the involvement and support of my colleagues, friends, and family.

First of all, I owe a heartfelt gratitude to my supervisor, Prof. R.L. Evans. His timeless ideas and support have been instrumental throughout my research project. I have learnt many valuable lessons from him.

I would also like to acknowledge the involvement from the members of my doctoral examination committee, Profs. J.D. Dale, S.G. Hatzikiriakos, C.J. Lim, W.J. Poole, S.N. Rogak, and K.J. Smith. Their inputs helped shape this thesis into its current form.

Profs. S. Cordiner and V. Mulone, my correspondence at the Università degli Studi di Roma "Tor Vergata", have provided generous assistance in the modeling component of this research, during and after my tenure as visiting scientist at their research group in Rome, Italy.

The technical staff at UBC Mechanical Engineering: S.A. Buxton, S. Carey, M. Fengler, R. Genshorek, and G. Jolly, and R. Parry – have been tolerant to overly inquisitive minds like myself. Their phenomenal ability to fabricate and repair the necessary experimental equipment must not be overlooked, as well as their willingness to provide extended loans on tools and gadgets.

To the many generations of doctoral colleagues: C.C.B. Reynolds, Wu Ning, M.L. Shield, M.M. Salehi, P. Darabi, A.A. Aliabadi, J.E.A. Saunders, and B. Günzel, who brought mutual joy and agony that made my stay at UBC much more enjoyable. I would also like to extend my thanks to my many master-level colleagues: J.-M.S. Logan, A.S. Chicka, E.J. Kastanis, V.R. Klapotcz, B.S. Brown, A.Z. Mezo, C.A. Laforet, and K.J. Gould.

Maja and Alan, I have not forgotten about the pitot tube. You two brought light in darkness.

I would also like to give my many thanks to my parents, Chan Boon Lak and Ma Chak Fung, for their understanding and unconditional support of this undertaking, as well as Siegrid "Mutti" Ketzler, who also provided many encouragements and optimisim along the way.

Finally, for Sabine, who stood by me and silently endured the hardship over the years, carrying my burden as her own. While words are not enough, I have reserved this paragraph as the keystone of my thesis.

Le talent, ça n'existe pas.
Le talent, c'est avoir l'envie de faire quelque chose.
Tout le reste, c'est du travail, de la sueur.

– Jacques Brel (1929 - 1978)

Statement of collaboration

Section 6.4 of this thesis is a modified version of the journal article entitled "Numerical and experimental characterization of a natural gas engine with partially stratified charge spark ignition" by E.C. Chan, M.H. Davy, G. de Simone, and V. Mulone, to appear in the ASME Journal of Engineering for Gas Turbine and Power in 2010. I was responsible for the implementation of the ignition code, and the meshing of the PSC spark plug. The open geometry engine simulations were performed by Ms. Giovanna de Simone. The original experimental data were collected by Mr. Conor Reynolds. The author was also the correspondant of the article and, along with Prof. Mulone, was responsible for the preparation of the manuscript.

Chapter 1

Introduction

Spark ignition is a common method for initiating combustion. An electrical discharge in an air-fuel mixture induces the growth of a high temperature flame kernel, which aims to establish a self-sustaining flame front that propagates through the remaining unburnt mixture. It can be found in many applications, from power generators to passenger vehicles. One of the major goals of the spark ignition system in an automotive engine is to produce stable combustion over a wide operating range. This is particularly important in lean-burn engines, since the increased likelihood of misfires offsets the benefits in fuel economy and emission levels.

The stability of the spark kernel has an immediate effect to the overall combustion quality (Abdel-Gayed and Bradley, 1985; Johansson et al., 1995; Peters and Quader, 1978). Methods for flame kernel stabilization usually involve some form of fuel stratification (Chung et al., 2003; Dale and Oppenheim, 1981; Hotta et al., 2007; Kettner et al., 2004; Lawrence and Watson, 1998; Murase et al., 1994; Robinet et al., 1999). A patented technology, called *Partially Stratified Charge* (PSC), injects a small amount of natural gas directly in the vicinity of the spark plug electrodes, creating a small fuel-rich pocket that fosters kernel growth. Laboratory engine experiments (Reynolds and Evans, 2004a,b) and computer simulations (Andreassi et al., 2003b, 2004) have demonstrated significant improvements in combustion stability and emission control under ultra lean-burn conditions.

While the physics for spark ignition have been well studied for homogeneous air-fuel mixtures in the past, spark ignition in stratified fuel conditions has only recently received some

interest. The present research attempts to identify the fundamental enabling mechanisms of stratified spark ignition, and derive the necessary mathematical models, verified under laboratory settings. Although the study concerns mainly with PSC, the same principles can be applied to all stratified ignition systems, as well as effects of fuel inhomogeneity in spark ignition.

1.1 Partially stratified charge (PSC)

The partially stratified charge (PSC) spark ignition technology (Evans, 2000) aims to reduce fuel consumption and stabilize lean combustion by injecting a small fuel plume near the ignition zone. The enriched fuel pocket facilitates spark ignition, allowing stable flame kernel growth. Experimental (Reynolds and Evans, 2004a; Reynolds et al., 2005) and numerical (Andreassi et al., 2004; Chan et al., 2011) studies have shown to have successfully extend the lean operating limit of spark-ignited natural gas combustion engines by about 10%. This represents an additional flexibility in throttless load control, as well as lower power-specific regulated and non-regulated emission levels.

Although existing research has so far demonstrated the feasibility of PSC, there still exists a need to better understand the fundamental enabling mechanisms behind this technology. In particular, there is an interest in providing answers to the following questions:

1. How does the presence of the PSC jet alter the local flow and air-to-fuel ratio,
2. How does PSC affect flame kernel growth, *and*
3. Can this behavior be predicted using measurable parameters?

The topic of PSC ignition presents a challenge and an opportunity. While the enabling mechanisms for spark ignition in premixed air-fuel mixtures have been well studied, spark ignition under stratified air-fuel environments has only gained attention very recently. In the

few existing works that involve experimentation and numerical simulations, expressions are yet to be developed to succinctly describe this phenomenon. This shall be the direction of the present work.

1.2 Research objectives

The goal of the present research is to identify the enabling mechanisms for the PSC technology, using a number of quantifiable and adjustable parameters. These relationships provide a means to produce an optimized and stable ignition behavior. The considerations below define the scope of this project:

Homogeneous bulk charge. The initiation of combustion through PSC spark ignition is the focus of the proposed research. The stratification must take place solely between the PSC injection and the bulk mixture in order to determine the contribution of the PSC in the ignition event. This can be achieved by using a homogeneous bulk charge.

No exhaust gas recirculation. Exhaust gas recirculation (EGR) systems are introduced in some automotive models to reduce fuel consumption and NO_x production. For simplicity in mixture preparation and analysis, issues related to EGR have been precluded from this study.

Minimized bulk charge movement. In premixed spark-ignition studies, bulk charge movements were introduced to examine their effects on flame kernel growth. This is most commonly produced using a reciprocating engine (Herweg and Maly, 1992), a fan-stirred combustion chamber (Abdel-Gayed and Bradley, 1985; Gillespie et al., 2000; Mandilas et al., 2007), or a moving perforated plate (Ting and Checkel, 2001). In the current study, however, the effects of the PSC charge movement were isolated from those of the bulk charge. As a result, care should be taken to minimize the bulk charge movement.

Minimized geometric effects. Spark ignition geometry has been one of the major influencing factors on flame kernel growth (Alger et al., 2006; Daniels and Scilzo, 1996). In that sense, a minimal geometry serves to minimize the possibility of flow impingement and heat loss. This allows the study to be focused on the interaction between PSC injection and the surrounding bulk mixture. Under this context, a mathematical model pertaining to the physical phenomena will be developed based on existing models. Complementary experimental and numerical data will be obtained to validate the model.

1.3 Thesis organization

The thesis examines the enabling mechanisms of the PSC technologies from the analytical, experimental, and numerical viewpoints, and the following chapters attempt to succinctly summarize the corresponding activities and findings.

Chapter 2 provides background information related to the current research. Particular focus would be placed on existing research on the PSC technology, fluid turbulence and spark ignition, as well as spark ignition in a stratified fuel environment.

Chapters 3 and 4 will be devoted to the experimental component of the current study. A constant volume combustion chamber (CVCC) was commissioned for the study, along with a customized PSC injection system. The specifications, as well as the implementation and verification of the experimental framework will be described in Chapter 3. The experimental program and corresponding results and discussion will be the subject of Chapter 4.

The analytical and numerical aspects of this study will be described in detail in Chapters 5 and 6. In the same way as the previous two chapters, the development and verification of the model will be contained in Chapter 5, while the results will be presented in Chapter 6. The

simulation results for internal combustion engines will also be included to partially address the relevance of this study to engine conditions.

A summary of research findings, as well as potential ideas for future research, will be presented in Chapter 7. A number of appendices follow, which present any supporting information deemed relevant to the proposed research.

Chapter 2

Literature review

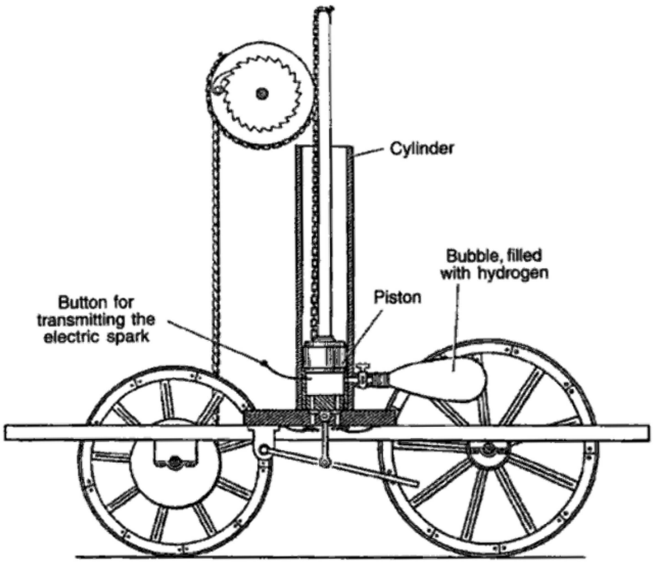

The above drawing is the 1807 vehicle prototype of François de Rivaz (1752-1828). The air-fuel mixture is ignited with an electrical spark. The ignited charge hurls up the piston, and drives the wheels on its way down through a ratcheted pulley. In addition to being the first hydrogen-fueled vehicle, it was also the first spark-ignited internal combustion engine ever built (Eckermann and Albrecht, 2001). More than two centuries have passed since the de Rivaz prototype, but little has changed in the operating principles of spark ignition. Despite recent advances in laser spark ignition (Beduneau et al., 2003; Ma et al., 1998), electrical spark ignition remains the most accessible method in automotive applications.

Early efforts in understanding spark ignition were concerned with the physical behavior of the electrical discharge and the initiation of the flame kernel. The particular interests are

the modes of energy transfer from the spark electrodes to the air-fuel mixture (Maly, 1984), and the bifurcation of the flame kernel development towards expansion or extinction, resulting from hydrodynamic and thermo-diffusive perturbations (Deshaies and Joulin, 1984). Generally speaking, a flame kernel is considered "mature" when it is large enough to be propagated to the remaining unburnt mixture (Eichenberger and Roberts, 1999). Turbulence can have a significant influence on kernel growth, and is thus integral in defining the criterion of maturation. A number of detailed and simplified models have been proposed to simulate the process (Herweg and Maly, 1992; Jenkins et al., 2006).

In the context of PSC, spark ignition takes place in a non-premixed environment. The intermittent nature of fuel pocket distribution is reflected in the stochastic treatment of ignition behavior (Birch et al., 1981). Further, the flammability of the local mixture is also affected by flame stretch (Ahmed et al., 2007). The investigation in non-premixed spark ignition is still a relatively new topic, and research efforts have so far been focused on establishing the probability of successful ignition with local pre-ignition hydrodynamic and thermodynamic conditions.

2.1 Natural gas as an alternative energy carrier

Natural gas (NG; CNG for the compressed variety) is a fossil fuel primarily composed of methane (CH_4), some heavier hydrocarbons (HCs), and trace amounts of inert gases. The volumetric CH_4 composition of NG varies from 70% to 99%, while in British Columbia it is between 91% to 97%. The volumetric compositions of several local CNG samples are presented on Table 2.1, while the corresponding samples around the world are provided on Table 2.2 for comparison.

The relationship between NG and other conventional and alternative fuels is also explored to better understand the its role as an automotive fuel. The major properties of some commercially available fuels are listed on Table 2.3. Since these fuels are often blends of many different hydrocarbons, it is acceptable to describe a fuel through its representative component, such as methane (for CNG), propane (for LPG) and iso-octane (for gasoline). Their properties are also included in Table 2.3. Finally, a brief discussion has been accommodated for hydrogen.

Table 2.1: CNG samples in British Columbia, by percentage volume.

Sample	**CH_4**	**C_2H_6**	**C_3H_8**	**C_4H_{10}**	**C_5H_{12}**	**CO_2**	**N_2**	**Others**[a]
1993 May[b]	95.50	3.00	0.50	0.15	0.04	0.20	0.60	0.01
2001 May[b]	96.36	1.91	0.41	0.15	0.04	0.20	0.89	0.04
2002 Oct[c]	95.95	1.95	0.55	0.18	0.05	0.42	0.87	0.03
2005 Oct[d]	91.43	6.60	0.32	0.12	0.04	0.40	1.09	0.01
2008 Oct[e]	94.91	1.62	0.38	0.14	0.04	0.16	0.63	0.01
2009 Jan[f]	96.44	1.86	0.49	0.15	0.04	0.25	0.72	0.04

[a]Includes higher HCs.
[b]Source: Terasen Gas Tilbury Station (Reynolds, 2001).
[c]Source: Terasen Gas Tilbury Station (Brown, 2003).
[d]Source: Westport Innovations Inc. (Gorby, 2007).
[e]Source: Westport Innovations Inc. (Brown and Veliath, 2008).
[f]Source: Terasen Gas Tilbury Station (Cox, 2009).

Table 2.2: CNG samples around the world, by percentage volume.

Sample	**CH_4**	**C_2H_6**	**C_3H_8**	**C_4H_{10}**	**C_5H_{12}**	**CO_2**	**N_2**	**Others**
BC[a]	95.80	2.10	0.45	0.15	0.04	0.20	0.71	0.03
USA[b]	81.34	4.69	6.12	0.53	0.11	0.91	5.11	1.18
North Sea[c]	93.25	4.54	0.78	0.15	–	0.63	0.61	n/a
Pakistan[d]	93.48	0.24	0.24	0.10	0.41	n/a	4.02	n/a
Qatar[d]	76.60	12.59	2.38	0.32	0.02	n/a	0.24	n/a

[a]Mean average from Table 2.1.
[b]Sources: Maxwell and Jones (1995), and King (1992).
[c]Sources: Dicks (1996) and Bosch (2007).
[d]Source: Dicks (1996).

Table 2.3: Typical properties of relevant commercial and reference fuels.

Property	**CNG**[a]	**LPG**[b]	**Gasoline**	**Methane**	**Propane**	**Iso-octane**	**Hydrogen**
Effective composition	$C_{1.04}H_{4.07}$	$C_{3.03}H_{7.95}$	$C_{7.88}H_{15.3}$	CH_4	C_3H_8	C_8H_{18}	H_2
Mean molecular weight [g/mol]	16.6	44.4	110[c]	16.0	44.1	114	2.02
Total HC content [% vol.]	98.0	97.5	99.9	100	100	100	100
Density[d] **at 20° and 1 bar** [kg/m^3]	0.763	1.89	747.5	0.662	1.84	690	0.0828
Ignition temperature[d] [K]	875	670	570	920	740	680	830
Stoichiometric AFR	16.8	15.2	14.7	17.2	15.7	15.1	34.3
Stoichiometric volume fraction [%]	9.42	4.11	1.76	9.48	4.02	1.65	29.5
Stoichiometric mass fraction [%]	5.61	6.16	6.37	5.48	6.00	6.20	2.83
Lower/upper flammability limits[d] [% vol.]	4.3/16.2	1.5/15	0.6/8.0	5.0/15	1.9/9.5	1/6	4.0/77
Lower/upper flammability limits [% wt.]	2.50/9.95	2.28/21.3	2.24/24.8	2.83/8.90	2.86/13.8	3.83/20.1	0.298/18.9
Lower heating value[d] [MJ/kg]	49.9	45.0	41.6	50.0	46.3	44.6	120
Stoichiometric mixture energy [MJ/m^3]	3.13	3.35	3.41	2.91	3.29	3.55	2.07

[a]Based on average CNG composition on Table 2.1.
[b]Based on a volumetric composition of 90% propane, 5% propylene (C_3H_6), 2.5% butane, and 2.5% residual components (Wallace, 1989).
[c]Source: Heywood (1988).
[d]Source: Bosch (2007).

2.1.1 Comparison with gasoline

Natural gas has a number of advantages over conventional liquid fuels such as gasoline. In gaseous form at atmospheric pressure, NG requires no prior vaporization to facilitate combustion. Further, with methane as its representative component, natural gas has a high effective hydrogen-to-carbon ratio (see Table 2.1). As a result, NG produces much lower amounts carbon dioxide (CO_2,) than gasoline, as well as other regulated emissions such as carbon monoxide (CO), nitrogen oxides (NO_x), and unburnt hydrocarbons (UHC).

In a comparative study, Maji et al. (2004) demonstrated a significant improvement with CNG over gasoline under the same equivalence ratios. The thermal efficiency was increased by three to five per cent, based on the lower heating value. In terms of emission levels, CO production was reduced by up to 80% for a relative air-to-fuel ratio (λ) of 0.7, and the corresponding UHC emissions also decreased by about 10%. Under lean-burn operation (λ = 1.2), the NO_x production was reduced by up to 12%. Similarly, a reduction of CO_2 emissions of between 25% and 33% was also observed under stoichiometric conditions, which was also noted in a well-to-wheel analysis by Prieur and Tilagone (2007).

While the benefits of using CNG are significant, its gaseous nature reduces the air-fuel energy density, which is expected to be about eight per cent lower compared to gasoline at stoichiometric proportion. This figure is consistent with the experimental observations of 10 to 12 per cent in laboratory and field settings (Maji et al., 2004; Thomas and Staunton, 1999; Weaver, 1989). The loss in power output can be compensated by elevating the intake manifold pressure or the compression ratio. With a higher octane number than gasoline, CNG is a suitable fuel for this purpose.

A small of improvement in energy efficiency can be obtained by increasing the compression ratio. In its simplest form, this involves physically reducing the clearance volume of the combustion chamber. The associated ease and low cost make this a popular method among small CNG engine owners in developing nations (Khan, 2001). However, such modifications are often unanticipated by the engine design, and the increase in friction and engine stress are likely to cause premature component failures.

Forced induction (i.e, supercharging or turbocharging) provides a more substantial and stable improvement for CNG engines. Moreover, additional reduction in direct exhaust emissions can be achieved by using a lean mixture, while maintaining engine power (Thomas and Staunton, 1999; Umiersky and Hüchtebrock, 2003), as presented on Table 2.4. The implementation of this technology in commercial passenger vehicles, such as the Ford Focus C-Max (2007), Opel Zafira (2008) and the Honda Civic GX (2009), is indicative of its maturity and anticipated commercial success.

Table 2.4: Performance of similarly sized engines running on gasoline and CNG, after Umiersky and Hüchtebrock (2003).

Fuel	**Gasoline**	**CNG** ($\lambda = 1$)	**CNG** ($\lambda > 1$)
Displacement [dm^3]	1.8	1.6	1.9
Compression ratio	10.5	12.5	14.5
Supercharger	No	No	Yes
Peak power [kW] (@RPM)	92 (5600)	71 (5800)	100 (4000)
Peak torque [N·m] (@RPM)	170 (3800)	145 (4000)	300 (2000)

2.1.2 Comparison with liquefied petroleum gas (LPG)

A liquefied commercial fuel containing propane and butane in various ratios as principal constituents is marketed as liquefied petroleum gas (LPG). The automotive fuel grade for LPG is HD-5*, and typically contains a minimum of 90% propane by volume (Wallace, 1989). There

*The numerical designation denotes the maximum allowable volumetric propylene (C_3H_6) content. Propylene is used in the manufacture of plastics, and propylene build-up in an engine may cause components to gum up.

are approximately 10 million vehicles operating on LPG worldwide* (WLPGA, 2007), compared to 5.3 million CNG vehicles (Bosch, 2007).

The stoichiometric mixture energy content for LPG is slightly higher than CNG. In gaseous form, the reduction in engine power by switching from LPG to CNG can be significant, to up to 17% (Saraf et al., 2008). This figure, however, also depends on the actual fuel composition†. Production of CO_2 in CNG engines is also expected to be about 10% lower than similar sized LPG engines (Bosch, 2007). Further, Whitney and Bailey (1994) observed a decrease in CO and UHC emissions with CNG over LPG under lean-burn ($\lambda = 1.25$) conditions. The corresponding UHC emissions for lean-burn CNG is less than half that for LPG. This indicates higher combustion stability.

Despite definite advantages in fuel economy and emission production, there is still a strong populist preference for LPG over CNG to fuel their vehicles. In a comprehensive multi-year study on converted LPG and CNG light-duty vehicles, Dardalis et al. (1998) showed that the initial conversion and life-time maintenance costs for a typical CNG vehicle were about 2.2 times higher than those for a LPG vehicle. However, the increase in operating costs can be compensated through the price margin between CNG and LPG.

2.1.3 Comparison with hydrogen

Hydrogen combustion is an inherently "clean" process. It involves no carbon, and therefore there is no concern for CO and CO_2 emissions. Its supplies can be replenished through electrolysis from water or through reformation of hydrocarbons or biomass. A majority of hydrogen supply today comes from steam reforming of fossil fuels (Kolb, 2008), in which case, of course,

*Still, this figure represents less than five per cent of the global transportation energy demand.

†According to Table 2.3, the stoichiometric reduction in energy density from LPG to CNG is about 6.57%. However, the 17% reduction reported in Saraf et al. (2008) can be achieved through a slight and simultaneous content elevation of methane for CNG, and butane for LPG.

CO_2 becomes a necessary by-product. Hydrogen has a wider flammability limit and a lower ignition energy than CNG and other fossil fuels (White et al., 2006). This facilitates combustion at λ values of four to five (Glassman, 1996).

On the other hand, hydrogen flames also propagate much faster than fossil fuels*, so there is an increased risk of backfire and premature detonation. Moreover, having the lowest density of all gaseous substances, hydrogen is prone to leakage, and has a tendency to displace a large amount of air during port injection. These two issues pose concerns on engine operation and passenger safety, but can be partially addressed with direct injection technologies.

Due to its low volumetric energy content (see Table 2.3), hydrogen must be stored at very high pressures, between 350 to 700 bar, compared to CNG, which is typically stored at 200 bar (Bosch, 2007). If the weight of the storage tank is also considered, a vehicle operating on LPG will provide a higher net power output than the same vehicle with hydrogen (Muradov, 2003). These factors together impose very stringent design and manufacturing constraints on the hydrogen vehicle. As a result, as a commercial combustible fuel, hydrogen is currently limited to a support role, either as a secondary fuel in "flex-fuel" vehicles, or in a blend with other gaseous fuels.

2.2 Partially stratified charge (PSC)

As mentioned in the previous section, CNG lends itself to lean-burn operations. Running lean, however, also increases the likelihood for misfires, and it is a principal cause for poor engine performance and UHC emissions. The quality of combustion can be evaluated by inspecting the magnitude of the indicated mean effective pressure (IMEP) as well as the timing at which the peak pressure occurs. Figure 2.1 shows a distinction between normal and poor combustion.

*The laminar flame speed (S_L) for H_2 is about 200 cm/s, and only between 30 cm/s and 40 cm/s for fossil fuels (Glassman, 1996).

With normal combustion, the pressure peak typically takes place at about 10 to 20 crank angle degrees (CAD) after top dead center (TDC). Poor or incomplete combustion will have the peak occurring closer to TDC, and with lower magnitudes of IMEP. A magnitude of IMEP near zero indicates that no fuel was consumed, and are therefore misfires.

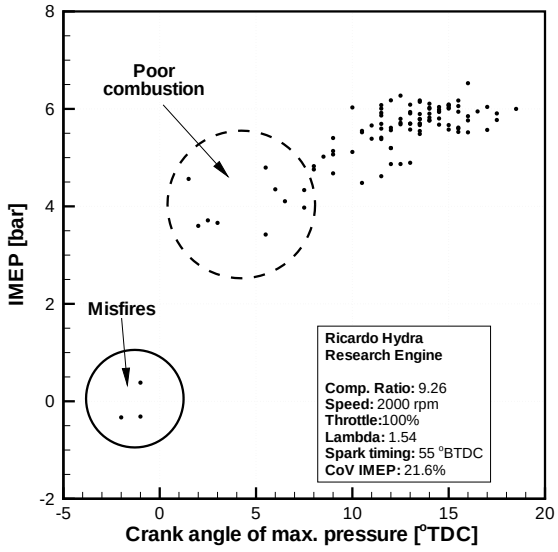

Figure 2.1: Distribution of IMEP over 100 engine cycles with respect to crank angle at $\lambda = 1.54$, identifying regions of misfire and poor combustion events. The working fuel is CNG (Reynolds and Evans, 2004b).

The stochastic limit at which the occurrences of poor combustion events become significant is termed the lean misfire limit (LML). It is often identified using the coefficient of variation (CoV) on the IMEP. Typically, the LML is defined at 10% CoV on IMEP (Heywood, 1988), although it can also be more rigorously defined at 5% (Reynolds and Evans, 2004b). It is generally believed that the quality of combustion is closely related to the stability of the ignition process. Peters and Quader (1978) further asserted that ignitability was also dependent on mixture preparation, and vaporized (or gaseous) fuels exhibited diminished probability to successfully ignite, which was also observed by Ahmed and Mastorakos (2006), and Ahmed et al. (2007).

During the initial stages spark ignition, the electrical energy produces a high temperature plasma. The energy within is then conducted as heat to the surrounding mixture, which

initiates combustion. This developing flame front is known as the flame kernel. The ignition process is considered complete (and successful) when the flame kernel is sufficiently large to be advected to the bulk unburnt mixture.

The rate of flame kernel expansion and its ability to propagate to the bulk mixture are sensitive to the local flow and mixture conditions at the ignition zone (Abdel-Gayed and Bradley, 1985; Johansson et al., 1995). This uncertainty presents a challenge for igniting a lean mixture, as the probability of having a ignitable fuel "pocket" near the ignition site decreases as the mixture is further leaned out. So the key to a better combustion quality, and therefore a better load control, lies in a stable, ignitable fuel and flow conditions at the ignition zone to foster kernel growth.

A number of technologies have been developed to promote kernel growth (Chung et al., 2003; Dale and Oppenheim, 1981; Hotta et al., 2007; Kettner et al., 2004; Murase et al., 1994; Robinet et al., 1999), all of which involve fuel stratification in some form of prechamber. The Partially Stratified Charge (PSC) concept (Evans, 2000, 2006), injects a small fraction of fuel directly near the ignition site, while the bulk premixed mixture is inducted through the intake manifold. Its premise is similar to the hydrogen assisted jet ignition concept (Dober and Watson, 2000; Lawrence and Watson, 1998), which stabilized combustion for values of λ up to 2.0. Both systems feature a self-contained injection / ignition unit. Unlike hydrogen assisted jet ignition, which has separate injection and ignition sections, PSC utilizes a co-located ignition and injection section, which allows the localized rich mixture to be introduced without a prechamber.

There are a number of advantages in adapting the PSC technology for spark-ignited engines. First, this technology has been demonstrated, in a research engine setting, to extend operating range by about 10% (Reynolds and Evans, 2004a,b). The immediate implication is that, stable

operation can be achieved at an ultra-lean level, at which the power output of the engine can be adjusted by altering mixture composition, as opposed to throttling, which introduces additional power loss. Furthermore, under ultra-lean conditions, the production level of regulated emissions in untreated exhaust gas will be substantially lower than stoichiometric levels. When carefully monitored, PSC engines could operate without the use of exhaust aftertreatment strategies, as they have the drawback of increasing fuel consumption. Lastly, due to its non-intrusive design, the PSC system can easily be retrofitted into conventional engines, which reduces implementation costs. The PSC ignition system is currently implemented on a Ricardo Hydra single cylinder research engine at the University of British Columbia Clean Energy Research Centre. The PSC charge is introduced using a modified spark plug, and the injection is metered by a solenoid valve through a capillary tube, as shown on Figure 2.2.

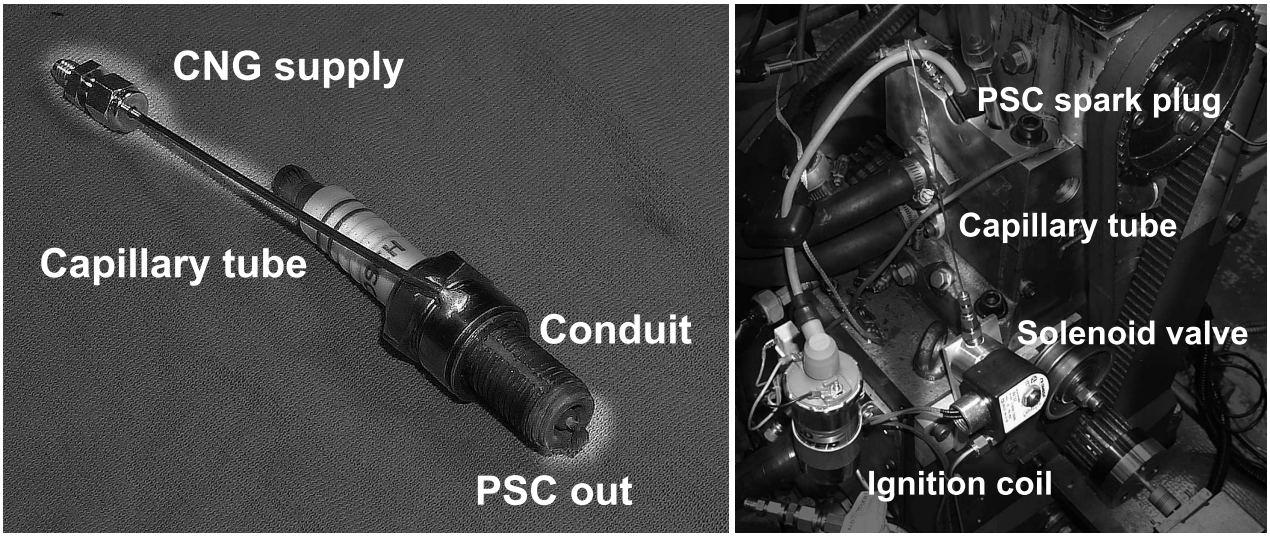

Figure 2.2: (Left) A PSC spark plug, modified from an automotive spark plug. (Right) The PSC spark ignition system, implemented on the Ricardo Hydra research engine.

2.2.1 Existing research

Experiments conducted on the Ricardo Hydra (Reynolds and Evans, 2004a,b) indicated an extension of the LML by up from $\lambda = 1.54$ to $\lambda = 1.71$ with PSC, a 10% increase from homogeneous

charge operation. The increase in operating range can also be observed in terms of the brake mean effective pressure (BMEP), with little penalty on efficiency, as presented in Figure 2.3. The trend in power-specific CO emission does not seem to be affected significantly by PSC, as with all lean-burn engines. However, a marked reduction can be observed in NO_x production. This is a departure from conventional stratified charge technologies, where elevated NO_x emissions limited their widespread use (Thomas and Staunton, 1999). Nevertheless, a significant increase was noted in UHC emissions. PSC visualization experiments by Mezo (2008) observed a long lag between the injection signal and the injection duration, which might account for the increase in UHC emission. Current efforts are being devoted to minimize the injection duration.

In addition to experimental work, collaborative research is also being conducted in an attempt to fully characterize and optimize the current PSC system through numerical modeling. Using KIVA-3V, Andreassi et al. (2003a) simulated the Ricardo Hydra for homogeneous operation. The work was later extended to include PSC (Andreassi et al., 2004), and the injection characteristics were modeled as a one-dimensional compressible flow problem. Both works were in excellent agreement with the experimental data. The first detailed modeling of PSC charge formation was performed by Chan et al. (2007). The results were also found to be consistent with the corresponding Schlieren images. The detailed injection model was subsequently deployed to model PSC combustion in a simulated engine environment (de Simone, 2008; Parisini, 2008).

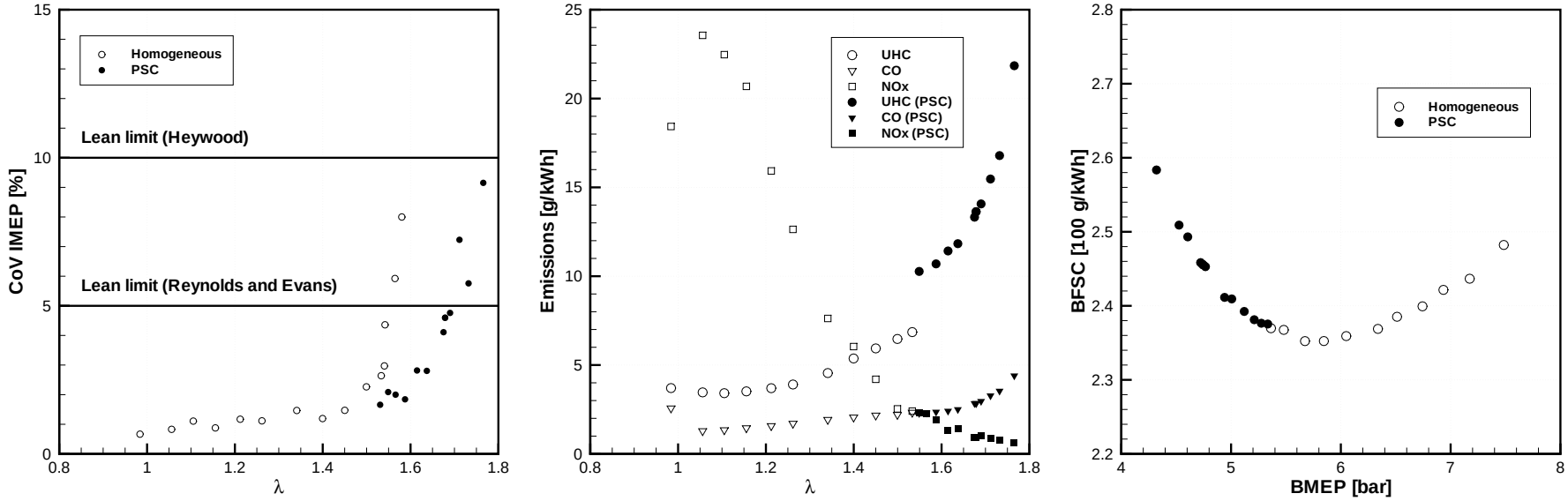

Figure 2.3: Performance with and without PSC, after Reynolds and Evans (2004a): (Left) CoV on IMEP, showing an extension in LML; (Middle) Brake specific emissions. (Right) BMEP and BSFC, with extended operating range; Note the increased UHC emissions under PSC.

Other aspects of PSC were also explored. Brown (2003) modified the PSC system for gasoline operation, and found that a more sophisticated design was essential to promote optimal mixing and fuel stratification for liquid fuels. Reynolds et al. (2005) investigated the potential benefits in using a premixed PSC injection, and found that optimal performance could be achieved with natural gas PSC injection. Williams and Evans (2006) incorporated exhaust gas recirculation (EGR) into PSC, and reported a significant reduction in NO_x emission. In collaboration with Westport Innovations Inc., Gorby (2007) adapted the PSC system for natural gas direct injection. Despite difficulties in igniting the mixture due to high concentration gradients in both the PSC and direct injections, late direct injection timings with PSC stabilized engine operation.

2.3 Phases of spark ignition

Spark ignition is a form of electrical discharge, which results from the creation of a conducting path between two points of different electrical potentials (i.e., the electrode anode and cathode), separated by a gaseous medium. The discharge is temporary, and serves to equalize the potentials. The electrical charge is carried across the gap through the migration of electrons, although ions may also carry charge. The process can be divided into three phases: *breakdown*, *arc discharge*, and *glow discharge*. Each phase is identified with distinctive time scales and energy transfer mechanisms.

2.3.1 Breakdown

The breakdown phase is the fast formation of a conducting path across the electrodes, a phenomenon only observed when the gas pressure is "high", such as atmospheric pressures (Bazelyan and Paizer, 1998). A sufficiently strong electric field liberates electrons from the cathode and accelerates them as they migrate towards the anode. Electronic collision with surrounding gas molecules results in ionization, which releases additional electrons. In turn, the additional electrons cause more electrons to be released through ionization. This chain

reaction is known as an electron *avalanche*, and serves to increase the available electrical current (Starikovskaia et al., 2004).

Meanwhile, the avalanche also creates positively-charged ions that move towards the cathode, albeit at a much slower speed than electrons. The ions undergo recombination at the cathode surface, which releases additional electrons. The process thus becomes self-sustaining, provided that sufficient ions can be produced through electron avalanche. The electron-ion distribution forms a highly conductive channel of about 40 μm in diameter between the electrodes (Maly, 1984). The potential across the gap at this point is called the *sparking potential*, and is regarded as the minimum required supply voltage to produce a spark. Paschen (1889) developed an empirical relationship to estimate the sparking potential, based on the density of the gaseous medium, as well as the distance between the spark electrodes.

With the establishment of the conducting channel, the electrical resistance across the spark gap drops significantly, even lower than voltage supply resistance (Bazelyan and Paizer, 1998). Hence the current flow across the gap is effectively limited by the external circuit (Heywood, 1988). Typically, the breakdown phase lasts no more than a few nanoseconds. At this point, electron-electron collisions become the primary mode of energy transfer (Spreadbury, 1954). The electron acceleration also causes an increase in electron temperature, to up to 60000K (Barrington-Leigh, 2000), resulting in an audible spherical shock wave at atmospheric pressure.

2.3.2 Arc discharge

The continual ion bombardment heats up the cathode surface, which becomes incandescent. Hot spots, however, develop and tend to become hotter as more electrons draw more positive ions. Therefore, ionization is thermally sustained, and the plasma temperature at 6000 K can be attained (Ekici et al., 2007). The intense heat results in a visible arc, after which this phase

is named. Electrical energy transfer still takes places across the spark electrodes, but at a much lower voltage and current than the breakdown phase, shown in Figure 2.4.

The abundance of high-energy but slow-moving particles in the plasma decelerates the plasma growth rate considerably. Heat conduction from the plasma to the surrounding mixture initiates combustion, and the flame kernel is formed. At this point, the kernel is sufficiently small that it is insensitive to local turbulence. So the early flame kernel growth is defined by a spherical, laminar flame front (Bradley et al., 1994; Johansson et al., 1995). It is also at this point that the expansion rate of combined plasma and flame kernel is at its minimum. The arc phase persists for a few microseconds, but can be prolonged, as long as the discharge current can be accommodated by the ignition circuit.

2.3.3 Glow discharge

The glow discharge phase sees a further decrease in discharge current, compensated by an increase in electric potential across the electrodes. The remaining electrical energy is dumped into the gas mixture as heat. Since the degree of ionization has been decreased substantially since the spark onset, the efficiency of energy transfer also decreases significantly in this phase. The core kernel temperature is further decreased to about 3000 K (Maly, 1984).

Of the three ignition phases, the glow discharge phase takes the longest to complete, typically between 0.3 ms to 3 ms. During this time, the flame kernel continues to grow by consuming the unburnt mixture in the vicinity, and increasingly influenced by the flow field. The energy transfer and propagation of the flame kernel can be considered as problems in the framework of classical thermodynamics, fluid mechanics, and heat transfer. For this reason, many spark ignition models effectively regard the glow discharge phase as the starting point (Herweg and Maly, 1992; Lipatnikov and Chomiak, 2002; Tan and Reitz, 2006).

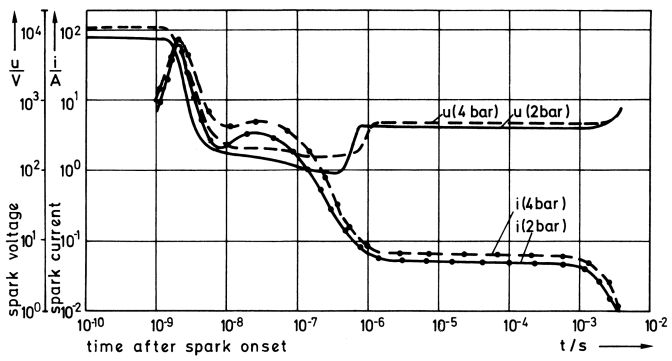

Figure 2.4: Typical output profiles for a TCI ignition system (Maly, 1984).

2.4 Source of spark energy

The spark ignition energy in vehicles is provided by the ignition coil, which supplies an electrical potential between 30 to 45 kV across the spark gap. The ignition energy and duration are dictated by the type of ignition system used. The traditional, transistorized coil ignition (TCI) system typically delivers 60 mJ of energy over a period of two milliseconds, while the capacitive discharge ignition (CDI) system, designed for use with higher RPM engines, provides 6 mJ of energy for 0.2 ms (Herweg and Maly, 1992). During the breakdown phase, the plasma is relatively small, so energy loss is at its minimum. As the plasma and flame kernel develop, interaction with the spark electrodes results in significant heat loss. An approximate distribution of heat loss is shown in Table 2.5.

Table 2.5: Estimated heat loss for the three ignition phases under idealized conditions, after Maly (1984).

	Breakdown	**Arc**	**Glow**
Radiation heat loss	1%	5%	trace
Conduction to electrodes	5%	45%	70%
Total losses	6%	50%	70%

The mean flow through the spark gap increases the amount of heated charge, hence increasing the energy transfer efficiency. This is shown in Figure 2.5. For a TCI system, the long electrical discharge duration also results in a very low total transfer efficiency from heat loss

(mainly to the electrodes) in the arc and glow discharge phases. Meanwhile, the efficiency for the arc discharge phase, prolonged with a high current spark discharge, is between 35% to 40%. While the electrical discharge still takes place, reignition of fresh charge is possible at the spark gap when the mean flow velocity is sufficiently high, but the energy transfer from subsequent plasma is much weaker, so the expansion rate is also correspondingly much lower. The reignition forms a horn-shaped entity, which Herweg and Maly (1992) termed *cornucopia*.

2.5 The flame kernel

Following spark ignition, the localized deposition of energy raises the local temperature, initiating combustion. Zel'dovich et al. (1984) postulated this initial phase as a "flame ball" known as the flame kernel. The flame kernel is an inherently unstable state due to differences in hydrodynamic and thermo-diffusive properties between the burnt and unburnt mixtures (Jomaas et al., 2007), leading to a bifurcation between *stable* (extinction) or *unstable* (propagation) equilibria, formulated by Deshaies and Joulin (1984), as well as Vázquez-Espí and Liñán (2002).

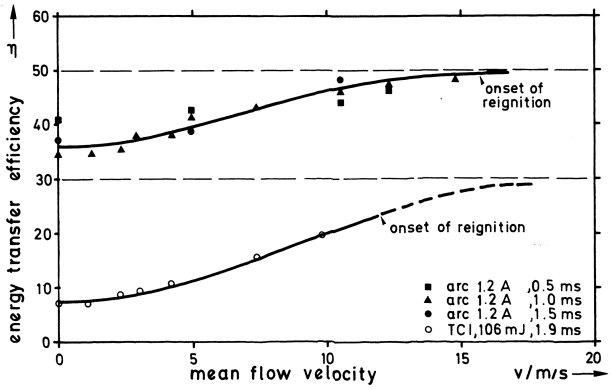

Figure 2.5: Energy transfer efficiency for arc and glow discharges in flowing air at 300 K, 1 bar, 1 mm gap (Maly, 1984).

The term *ignition delay* is used to describe this period of kernel development, to draw analogy from diffusion flames. However, the same term may also refer to the time between the spark onset and the first appearance of the flame kernel (Herweg and Maly, 1992). To avoid this ambiguity, the duration of flame kernel development will be termed *flame kernel maturity*,

coined by Eichenberger and Roberts (1999). There is currently no universal, formal definition for flame kernel maturity, though there are number of commonly accepted criteria, depending on the type of analysis and the data that are available.

2.5.1 Definition of kernel maturity

In a rudimentary sense, the maturity of the flame kernel can be inferred by the fuel consumption history of the combustion event, which can be derived from the corresponding pressure trace. The duration of the flame kernel growth can be defined by a reasonable but arbitrary level of initial mass fraction burnt (MFB). The generally accepted criterion for flame kernel growth is the first 5% or 10% MFB (Aleiferis et al., 2003; Heywood, 1988; Ozdor et al., 1994), though figures as low as two per cent are also used (Daniels and Scilzo, 1996; Eichenberger and Roberts, 1999; Kalghatgi, 1985). The MFB criterion is the preferred (and often the only) definition for engine and combustion chamber experiments, where the cylinder pressure trace is the only instantaneous data available. This criterion, however, is more a reflection on the quality of the pressure data than on the physics of kernel growth (Hacochen et al., 1993), since the pressure rise attributed to flame kernel growth is small.

Alternatively, the flame kernel can be viewed as a transitional phase from the spark onset to a fully developed flame. Therefore the kernel development process is deemed mature, when the expansion rate of the flame kernel reaches the fully developed flame speed. This definition has been mentioned in Herweg and Maly (1992), Bradley et al. (1994), and Aleiferis et al. (2003). While this approach brings analytical elegance (and some analogy to the boundary layer theory), the fully developed flame speed becomes difficult to evaluate in the presence of turbulence*. Moreover, the fully-developed turbulent flame speed, for which models are numerous (Fan and Reitz, 2000; Gillespie et al., 2000; Lipatnikov and Chomiak, 2002), is only

*Lipatnikov and Chomiak (2002) presented a 75-page article devoted to the relationship between the fully developed turbulent flame speed and the corresponding flame brush thickness.

an approximation to the actual flame kernel expansion speed, where the influence of plasma expansion is still dominant.

A third approach concerns the physical size of the flame kernel. It is generally accepted that the kernel reaches maturity, when it has grown sufficiently large to be advected to the remaining air-fuel mixture. This is supported from the notion that a critical size must be reached for the flame kernel to become self-sustaining (Chen and Ju, 2007; Deshaies and Joulin, 1984). This critical scale can be defined either based on length (Herweg and Maly, 1992; Tan and Reitz, 2006), or volume (Andreassi et al., 2003b; Kuo and Reitz, 1992). Due to the visual prerequisite to this definition, it is favored by studies involving optical characterization or numerical simulation of the combustion process. In the presence of turbulence, as it is almost always the case, the critical length scale can be defined according to the integral length scale (Fan and Reitz, 2000; Herweg and Maly, 1992; Song and Sunwoo, 2000; Tan and Reitz, 2006).

The above definitions implicitly assume a progression from the electrical spark to a fully developed flame through the flame kernel, and preclude an underdeveloped or an extinguished kernel as a possible outcome. This is important as the quality of the flame kernel dictates the quality of the overall combustion. The cycle-by-cycle peak pressure in a spark ignition engine was successfully replicated based on the fraction of flame kernel surface supporting flame propagation (Hacochen et al., 1993). Peters and Borman (1970) determined the quality of combustion based on cycle-by-cycle mass burning rates. Using the integral length approach, Chan et al. (2011) extended the flame kernel growth definition to include instances of quenching.

2.5.2 Effects of turbulence

Bradley et al. (1994) captured exactly the process of flame kernel growth under turbulence:

> "At first, the turbulent components of the flow act on the small kernel as a convective flow field, but the aerodynamic strain soon begins to stretch the flame and the higher-frequency components of the turbulent spectrum begin to wrinkle it. As the flame grows the wrinkling progressively is created by ever lower frequencies, with associated increase in the turbulent burning velocity, until eventually a fully developed turbulent flame ensues."

The evolution of the flame kernel can be conceptualized to be bounded by the Kolmogorov and integral length scales (Herweg and Maly, 1992). Due to the small initial size, the emerging flame kernel grows as a linear combination between a laminar flame and the radial expansion of the plasma (Ho and Santavicca, 1987). Turbulent effects will quickly follow, as early as 100 μs after the spark onset (Eichenberger and Roberts, 1999). The flame kernel geometry, initially spherical, will then undergo deformation as a result of turbulent interaction with the surrounding fluid. This is known as *wrinkling*. The PLIF data of Eichenberger and Roberts (1999) showed that enhancement can be achieved through "weak" turbulent vorticies, that is, those in the turbulent spectrum to which the kernel are relatively insensitive. This also means, that the likelihood for extinction also increases as the flame kernel grows, as indicated by the DNS simulation performed by Jenkins et al. (2006).

It is also found that, turbulence is more likely to hinder flame kernel development under lean-burn conditions than in stoichiometric conditions (Ho and Santavicca, 1987). This is intuitive, as the turbulent flame speed is, in part, dependent on the laminar flame speed, which decreases when the mixture concentration deviates from stoichiometric proportions. Abdel-Gayed and Bradley (1985) identified the fully developed quenching limit using the Karlovitz number (dimensionless flame stretch) and the Lewis number (ratio between thermal and mass diffusivities). These limits were subsequently identified on the Borghi diagram (Abdel-Gayed et al., 1989). How these limits affect flame kernel growth are, again, subjects that will be addressed later in this thesis.

2.5.3 Modeling

Flame kernel development represents only up to the first 10 % MFB, but it occupies as much as 30% of the total combustion duration (Eichenberger and Roberts, 1999), so an accurate model is of paramount importance. Though fundamental studies have been carried out using detailed modeling techniques (Bastiaans et al., 2007; Ekici et al., 2007; Jenkins et al., 2006; Thiele et al., 2002; Yaşar, 2001), such approaches are often impractical for internal combustion engine simulations, for the spatial and temporal resolution required to resolve the ignition event results in issues in numerical efficiency and stability. Therefore, the majority of ignition models are executed separately from the main flow and combustion simulation, often as zero or one dimension models. In addition, as the combined time scale for the breakdown and arc discharge phases is very small, the glow discharge phase is effectively regarded as the starting point of the ignition models, and the outcomes of the earlier two phases are represented through initial and boundary conditions.

The simplest form of such model is of the *energy deposition* type. The ignition energy is represented as a source term in the energy equation, while the formation of the ignition kernel is resolved explicitly within the main computational framework. This technique is found in DNS (Chakraborty et al., 2007; Vázquez-Espí and Liñán, 2002) or LES studies (Lacaze et al., 2009b), where the computational time step is small enough to resolve the evolution of the flame kernel. While the only phenomenological considerations are the profile and geometry of the spark energy distribution, the energy deposition method is computationally expensive, since reactions in the entire computational domain must be considered at the moment of the spark onset.

Another approach is to treat the growth of the flame kernel as a level-set problem (Osher and Sethian, 1988), similar to the G-equation (Peters, 2000) that is used for flame-front tracking.

The model of Zimont and Lipatnikov (1995) is among the most commonly used, due to its association with commercial CFD packages. Phenomenological models for flame kernel velocity are required for closure, however. These models are derived from empirical expressions for fully-developed turbulent flames, as indicated in Lipatnikov and Chomiak (2002). Since flame kernel growth is a transitional process, and that the contribution of turbulence only becomes prominent at the later stages, the insistence on a using a fully-developed turbulent closure model is questionable.

It is commonly accepted that the local turbulence level, fuel type, air-to-fuel ratio, and the thermodynamic state of the fluid at the time of ignition are contributing factors in flame kernel development (Aleiferis et al., 2004; Herweg and Maly, 1992). The space and time aspects for kernel maturation can be related with a model for kernel growth rate, which can be effectively regarded as a linear combination between the plasma expansion speed and the developing flame speed of the kernel. The integral length scale definition of flame kernel maturity, discussed in Section 2.5.1, can be used to determine the critical flame kernel size. Meanwhile, the temperature and energy of the mature kernel can be inferred from the spark energy transfer and chemical kinetics, such as GRI-Mech 3.0 (Smith et al., 1999) for natural gas. This approach has been demonstrated in numerous studies of this nature, including Kuo and Reitz (1992), Andreassi et al. (2003b), and Tan and Reitz (2006).

2.6 Non-premixed spark ignition

The discussion on spark ignition has so far been focused on premixed combustion. In fact, non-premixed spark ignition is considered a more general form of spark ignition combustion, particularly for lean combustion, where stratification and inhomogeneity in fuel distribution is all but certain. Despite practical significance of non-premixed spark ignition, investigation in this area remains sparse. Due to fluctuations in mixture concentration, a stochastic approach is

often employed to describe non-premixed spark ignition. The probability of flame kernel maturation is directly related to the probability of finding a mixture within its flammability limits (Birch et al., 1981; Smith et al., 1986). The choice of probability density function is therefore essential, for intermittency at the fuel pocket boundary is particularly problematic, even for simple flow configurations such as round jets. The β and δ functions are typically employed to model the bimodal boundary region (Alvani and Fairweather, 2002), and a composite of different probability distributions are needed to model the transition from the core region to the boundary (Effelsberg and Peters, 1983).

Using a bluff-body configuration, Ahmed and Mastorakos (2006) and Ahmed et al. (2007) further asserted the influence of flame stretch, which could lower the probability of kernel maturation. This was confirmed by the numerical laminar ignition analysis of Richardson and Mastorakos (2007). The ignition probability approach was further applied in LES simulations of Lacaze et al. (2009a,b) in similar settings.

2.7 Summary

The ignition process can be conceptualized into three distinctive phases, namely, breakdown, arc discharge, and glow discharge. Each phase is characterized by different physical mechanisms and time scales. The energy transfer efficiency of spark ignition is typically between 10% to 30%, depending the local bulk flow velocity. Reignition is also possible provided a sufficiently high bulk flow velocity, but the intensity of each reignition event becomes subsequently weaker. The ignition process induces combustion in the air-fuel mixture. This, and the expanding plasma from the spark ignition, result in a spherical flame front known as the flame kernel. The transformation from the flame kernel to a self-sustaining flame front is termed kernel maturation, and there are a number of criteria describing this transition. However, in order to fully describe stochastic phenomena such as cyclic variations and ignition probability, the

definition must be extended to include the possibility of an kernel extinction, an issue that this research will attempt to address.

Turbulence also plays a significant role in flame kernel survival, since this causes wrinkling in the flame kernel surface. As the flame kernel grows, it becomes increasingly sensitive to the lower frequency components of the local turbulent spectrum. This ultimately hinders flame kernel growth, and the effect is amplified under lean-burn conditions. Mathematical models were developed by others to describe flame kernel evolution and maturation based on local flow conditions and chemical kinetics.

The combustion regime represented by PSC ignition falls into the category of non-premixed spark ignition combustion. Though it is also a more realistic portrayal of spark ignition combustion as a whole, research on this subject is still at its infancy. Existing experimental and detailed numerical studies suggest an increased sensitivity to strain rate under non-premixed conditions. A strong link can also be observed between the probability of a successful ignition event to that of finding an ignitable mixture pocket, necessitating a probability density function that fully characterizes the fuel concentration distribution. However, spark ignition in a stratified fuel environment is still a relatively new study area, partly due to the stochastic treatment of fuel concentration and ignition probability. Additional work must be done to establish a definitive relationship between local inhomogeneity in fuel concentration and the growth of the flame kernel, as well as a method to quantify the sensitivity of the non-premixed spark kernel to flow conditions and chemical kinetics.

Chapter 3

Experimental design and configuration

The object of the visualization experiments is to investigate the enabling mechanisms of the PSC ignition strategy. An idealized PSC system has been adopted to isolate effects of flow geometry. The visualization of injection and ignition events is made possible through high-speed Schlieren motion photography in a optically accessible combustion chamber. One of the greatest challenges, however, is the selection of a proper injector. The present study utilizes a commercial CNG port injector, modified to operate at higher pressures. The characterization of the new PSC injection method will be discussed. It can be shown that this approach provides substantial improvements over its predecessors, in terms of response, reliability, and mass injection. A number of techniques are also employed for post processing of the experimental data. Of particular interest is the filtering of the combustion pressure traces, as well as the feature detection scheme for the Schlieren images. These methods are designed for a systematic automation of data processing, and to eliminate arbitrary manual intervention.

3.1 The idealized PSC ignition system

The PSC spark plug ignition system results in a highly complex injection flow field and flame propagation behavior. Its direct characterization have been the focus of the works of Chan et al. (2007, 2011), and Mezo (2008). Though qualitative data could be inferred from the visualization, the enabling mechanisms of PSC had yet to be identified. An idealized, minimal PSC ignition system was therefore introduced to minimize the effects of spark plug and injector geometry, as shown in Figure 3.1. A pair of sharpened thin-wire electrodes provide the electrical spark

in lieu of the spark plug, to minimize conduction heat loss and flow obstruction. Subsequent tests suggested that the PSC jet still exhibited axisymmetric features, despite the presence of the electrodes.

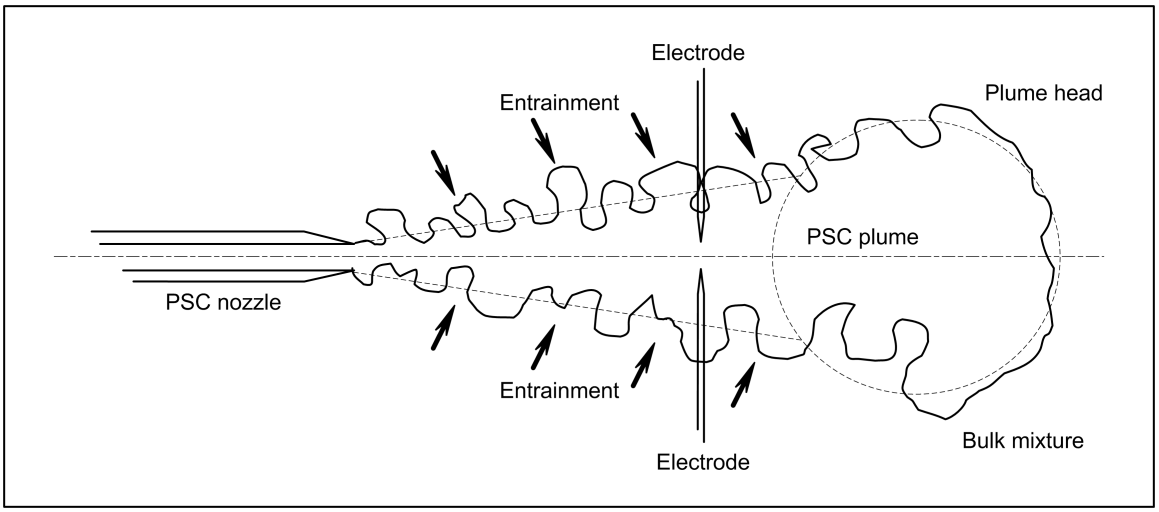

Figure 3.1: Schematic of the idealized PSC ignition system.

The PSC charge can be delivered in the form of a capillary round jet. Sangras et al. (2002) classified such phenomenon into three phases: the transient jet, the interrupted jet, and the puff. The transient jet is the initial phase, where the jet is initiated and sustained by a source. When the source ceases, the jet enters an intermediate regime known as the interrupted jet, and eventually transitions into the puff phase. The PSC injection falls into the transient jet category, which has been well studied in the past (Hill, 1972; Ricou and Spalding, 1961; Turner, 1963). Effects of compressibility have been examined in Birch et al. (1984), Chepakovich (1993) and Ouellette and Hill (2000), and the issue of non-self-similar developing jets was discussed in Cossali et al. (2001). Moreover, it is also a simple, axisymmetric geometry that can be modeled adequately with Reynolds-average type turbulence models. In this case, the round-jet/plane-jet anomaly must be remedied, most commonly by modifying the turbulent model constants, which limits the turbulent dissipation rate and, consequently, corrects the prediction of jet penetration and spreading rates (Pope, 1978; Poroseva and Bézard, 1999).

The ignition zone is kept along the axis of symmetry of the PSC jet. This allows for a detailed, but simplified analytical and numerical treatments, since the PSC ignition system could be effectively regarded as axisymmetric under this implementation. More importantly, an off-axis ignition arrangement increases the chance of igniting the edge of the PSC jet, where the fuel concentration distribution becomes intermittent (Alvani and Fairweather, 2002; Effelsberg and Peters, 1983). This results in a diminished probability of successful ignition beyond its flammability limits (Ahmed and Mastorakos, 2006; Smith et al., 1986). The in-line axisymmetric injection and ignition arrangement allows the ignition event to be initiated and investigated in a deterministic manner.

3.2 Experimental setup

An experimental visualization system was set up to capture the injection, ignition, and combustion events with PSC. Central to the system are the constant volume combustion chamber, and PSC injection system, both developed specifically for this research. The bulk fuel-air mixture was delivered from a separate preparation chamber. The PSC injection and ignition events were captured visually using Schlieren motion photography, and the aggregate behavior during the process was monitored with a number of in situ sensors. The command and data acquisition were managed using a combination of hardware and software synchronization strategies.

3.2.1 Constant volume combustion chamber

Following the initial studies of Chan et al. (2007) and Mezo (2008), based on a combustion chamber designed by Gete (1991), it was recognized that additional, fundamental work needed to be conducted using the aforementioned, idealized PSC system. To this end, a second constant volume combustion chamber (CVCC) was constructed to visualize the evolution of the spark ignited flame kernel under such arrangement. It consists of an optically accessible, cylindrical combustion chamber body, and fully modularized sections for instrumentation as well

as PSC injection / ignition. As a result, the CVCC can be adapted for a variety of visualization experiments. A drawing of the CVCC is presented on Figure 3.2, and the detailed drawings can be found in Appendix A. The bore of the CVCC was set to 80 mm, which mimics the bore size of the Ricardo Hydra single cylinder research engine. Four view ports were created at right angle of each other, around the chamber's axis of symmetry, and were circular to minimize fabrication costs. The port diameter was limited to 50.8 mm, and the interior height of the CVCC was also set accordingly (to 50.8 mm) to maintain total visibility in the axial direction. The displacement of the CVCC was determined to be 369 mL, by measuring the amount of ethylene glycol used to completely occupy the the CVCC volume.

In order to maintain axisymmetry, the PSC jet nozzle, and the ignition zone were located along the jet's axis of symmetry of the CVCC. The PSC charge was injected through a capillary tube (⌀0.571 mm), mounted along the central axis of the CVCC, and the spark ignition was accomplished through a pair of tungsten electrodes (⌀0.406 mm). The electrode gap was set to 1 mm, and was located 10 mm downstream from the capillary nozzle. The choice of spark gap and the axial placement of the electrodes, however, were somewhat arbitrary. Though the amount of spark energy is directly proportional to the spark gap (Paschen, 1889), a nominal value of 1 mm was found to provide sufficient energy to initiate combustion. Further, with the presence of the PSC jet, it was desirable to position the electrode pair closer to the jet nozzle, in order to maximize the view of the combustion downstream. Given that the jet would take between 6 to 20 pipe diameters to reach a self-similar flow profile (Cossali et al., 2001; Ouellette and Hill, 2000), a distance of 10 mm from the nozzle was deemed satisfactory. The electric spark was provided by a MSD Blaster 2 ignition coil. Table 3.1 shows the operating parameters of the CVCC and the PSC ignition system.

The expected combustion pressures were calculated to determine the proper construction parameters for the CVCC. A short C++ program was written with Cantera (Goodwin, 2007), GRI-

Mech 3.0 (Smith et al., 1999), and the NASA thermophysical database (McBride et al., 1993), to calculate the post-combustion equilibrium mixture composition and the corresponding thermodynamic properties. The initial unburnt mixture was a stoichiometric methane-air mixture at 8.5 bar and 300 K. The combustion process was considered adiabatic and isochoric. The equilibrium post-combustion pressure was calculated to be 41.8 bar. A generous factor of safety was given, however, so that the target design pressure would be at least 200 bar.

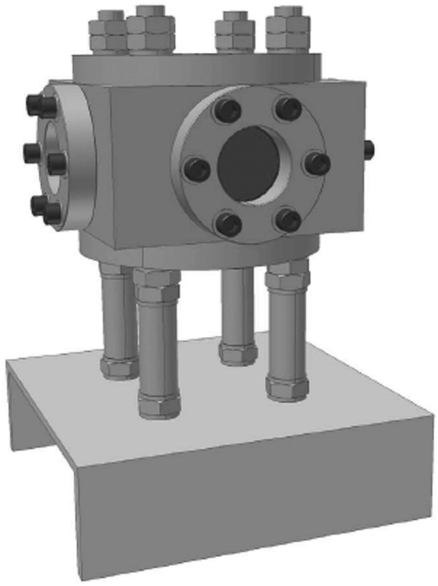

Figure 3.2: The constant volume combustion chamber.

Table 3.1: Operating parameters of the constant volume combustion chamber.

Bore diameter	80 mm
Clearance height	50.8 mm
Number of view ports	4
View port diameter	50.8 mm
Chamber volume	369 mL
Injector nozzle diameter	0.571 mm
Spark electrode material	Tungsten
Spark electrode diameter	0.406 mm
Spark electrode gap	1 mm
Spark location from nozzle	10 mm
Spark location from centerline	0 mm (axisymmetric)

For verification, a finite element analysis was performed using ANSYS on the CVCC components (see Appendix B), using distortion energy (von Mises stress) as the failure criterion. Material properties for quartz were obtained from commercial supplier literature, and those for the silicone rubber padding were taken from o'Hara (1984). These data are also tabulated in Appendix B. Cases were executed for a static chamber pressure of 200 and 300 bar. While the metallic components were able to support both load levels, the quartz windows had a reported critical load of 240 bar, scaled between the two cases. Further, a pressure test was performed on the CVCC. A static load of 124 bar was applied, maintained for over 60 minutes, and the apparatus showed no signs of fracture or leakage.

3.2.2 PSC injection / spark ignition system*

The PSC injection had traditionally been metered by a modified Omega SV-121 solenoid valve (Reynolds and Evans, 2004b; Reynolds et al., 2005). Recent studies, however, have demonstrated difficulties with controlling the valve, which resulted in excessively long injection durations and unacceptably high PSC mass flowrates. Elevated UHC emissions and, in the worst case, misfires were commonplace (Chan et al., 2007; Gorby, 2007; Mezo, 2008). This prompted the search for a more suitable injector at minimal cost and design effort.

Under engine conditions, the PSC injections typically take place at 5 to 8 bar (gauge), thus precluding the use of unmodified commercial port injectors, which were designed to operate only at 3.5 bar (50 psig). A modified Keihin KN3 CNG/LPG peak-hold port injector was thus used for the study. Additional restraints were introduced to allow safe operation at elevated pressure levels. The diameter of the injector nozzle was reduced to 0.571 mm, which substantially reduced the static volume of the injector. The run length of the capillary nozzle was also minimized. A Lee Chek^{TM} miniature axial flow check valve ($\varnothing$0.187 mm) was also introduced to

*The author would like to acknowledge the contributions of Mr. J.-M.S. Logan for the work described in this section. The reader may refer to Logan (2010) for a detailed account of the injector modifications

the injector nozzle to prevent back flow at high chamber pressure. Figure 3.3 shows the Keihin KN 3 injector, and the conversion for PSC operation.

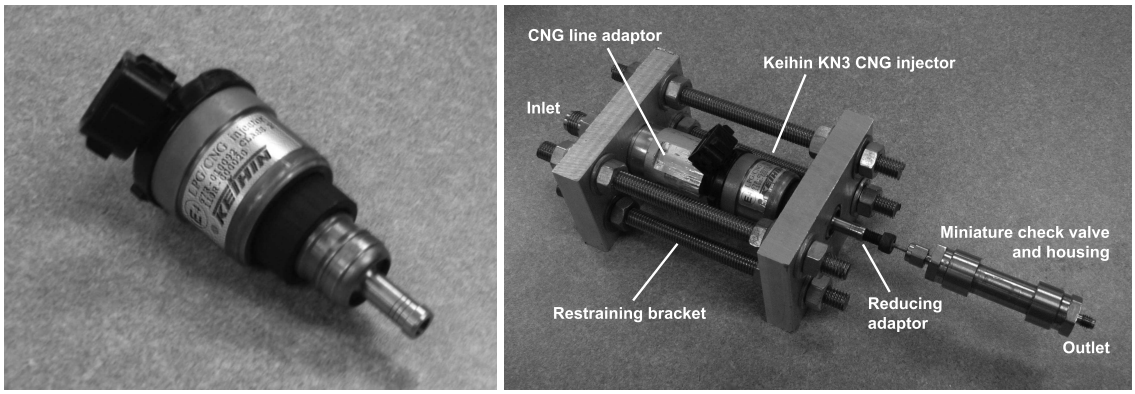

Figure 3.3: (Left) The unaltered Keihin KN3 CNG/LPG injector. (Right) The Keihin KN3 injector modified for PSC operation.

In addition, the injection signal was also altered to further manipulate its response. A customized injector driver, adopted from Brown (2003), was commissioned for the purpose. The injection signal was increased from 12 V to 350 V, such that the injector would open quickly at high pressures. The maximum operating pressure difference was subsequently increased from 3.5 bar to 10.9 bar. On the other hand, the minimum pulse width required to open the valve was summarily reduced from 2.2 ms to 250 μs. This implementation had a major drawback, however. The non-linearity introduced by the check valve, and the time-dependent injection profile resulting from the short injection signal, all but eliminate the possibility of estimating the PSC injection mass flowrate by analytical means. Therefore, it must be obtained experimentally. This will be discussed in Section 3.3.2.

3.2.3 Mixture preparation and fuel delivery

A schematic of the mixture preparation and fuel delivery system for the CVCC is presented in Figure 3.4. The air supply came from bottled compressed air with an initial pressure of 170 bar, and was replaced at regular intervals. An intensified natural gas supply (275 bar) was available

on-site, and was used for the PSC injection and bulk mixture preparation. The mixture was prepared in a mixing chamber, at a maximum total pressure of 70 bar.

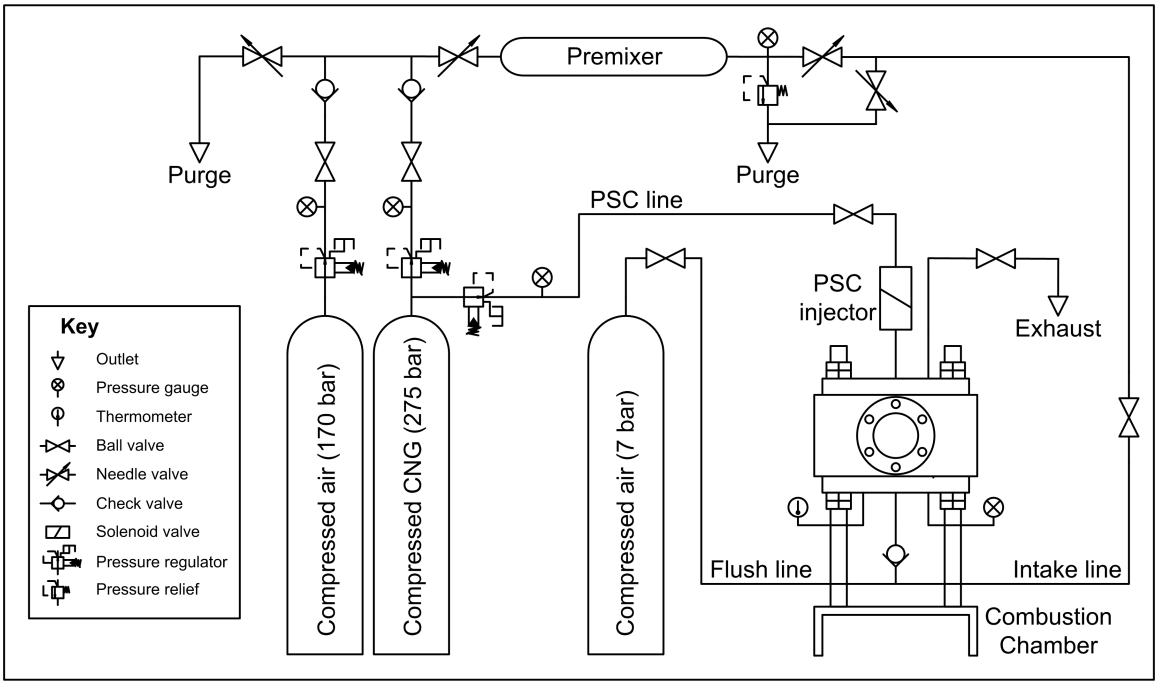

Figure 3.4: The CVCC fuel delivery system.

The partial pressure approach was used to obtain the proper air-to-fuel ratio. The required fuel partial pressure was calculated from that daily composition made available through Westport Innovations, Inc. (Wu, 2009), obtained using a gas chromatography analyzer. Detailed information on natural gas composition, and mixture partial pressures can be found in Appendix C. The pressure of the PSC fuel line is regulated to 10 bar (abs.) throughout. Based on the mass flow measurements outlined in Section 3.3.2, the amount of PSC injection was 0.35 mg, less than 0.6% of the bulk charge at $\lambda = 2.0$. Compensation of the overall bulk charge composition was therefore unnecessary to achieve a target air-to-fuel ratio.

3.2.4 Schlieren motion photography

Light propagates at different velocities under different material densities, ρ, and the degree of deviation is quantified through the refractive index, n. Since changes in ρ typically affects n

only very slightly for most gaseous media, a linear relationship between the two can often be assumed. When traveling in gaseous media of non-uniform densities, the incident light becomes deflected due to the spatial gradient of the refractive indices. These gradient disturbances are summarily termed *Schlieren*, the German word for *streaks*.

When the Schlieren are projected on a two dimensional plane, $\boldsymbol{x}$, such is the case of the CCD array of the high-speed camera, the light deflections can be sensed as planar displacements relative to the direction normal to the plane, $\boldsymbol{z}$, and is integrated over the length of the light path, L:

$$\frac{d\boldsymbol{x}}{d\boldsymbol{z}} = \frac{1}{n_0}\int_0^L \frac{\partial n}{\partial \boldsymbol{x}} d\boldsymbol{z}, \tag{3.1}$$

where n_0 is the ambient (homogeneous) refractive index. As indicated by Equation (3.1), the planar displacement is only a function of the *change* in refraction index, the corresponding length, L, can be taken to be the length where the distortion takes place. The optical distortion is further enhanced by blocking some of the distorted light from the projection plane. The blocked light forms a "shadow" on the image, allowing a clear visualization of the distortion which is otherwise nearly invisible to the naked eye.

Assuming a rectangular light source (from a mercury arc lamp, for instance) with a projected area of $h \times w$, representing the height and width respectively, the level of illumination, I_0, can be expressed as follows:

$$I_0 = \frac{B(hw)}{m^2 f_1 f_2}, \tag{3.2}$$

where B (in candella/m^2) is the luminance of the light source, m is the magnification factor of the image on screen, and the f values (in meters) are the corresponding focal length of the two mirrors (Settles, 2001). A vertical knife edge reduces the projected light source area to ha, where $a \leq w$, so Equation (3.2) becomes:

$$I = \frac{B(ha)}{m^2 f_1 f_2}. \tag{3.3}$$

Due to refraction in the test area, the cutoff causes a slight horizontal shift, proportional to the amount of optical deflection dx/dz, and the focal length of the second parabolic mirror f_2 (Weinberg, 1963). This yields:

$$dI = \frac{Bh}{m^2 f_1}\left(\frac{dx}{dz}\right). \tag{3.4}$$

The *contrast* of the setup is simply the change in luminance dI with respect to I:

$$\frac{dI}{I} = \frac{f_2}{a}\left(\frac{dx}{dz}\right), \tag{3.5}$$

and the corresponding *sensitivity* is defined by f_2/a. Theoretically speaking, the sensitivity of the Schlieren system is directly proportional to the amount of light blockage, but is accompanied by an increase in noise-to-signal ratio. The practical limit of sensitivity is ultimately dictated by the quality of the optical elements, and the accuracy of their alignment.

A Z-type Herschellian Schlieren visualization system was utilized to capture the evolution of the PSC jet and the ignition event, as illustrated in Figure 3.5. A mercury arc lamp was used for illumination, the collimation and condensation of light were accomplished with two identical parabolic mirrors with a diameter of 30 cm (12") and a focal length of 243 cm (8'). The sensitivity of the Schlieren setup was adjusted using a vertically mounted knife edge. A Nikkor 300 mm f/4D autofocus lens is used to focus the image. The images were captured with a Phantom 3815 high-speed CCD camera by Vision Research, at 10000 frames per second. The exposure time of each frame was 30 μs. The motion picture was transferred to a personal computer using Phantom Software CC v. 605.2, and was saved as consecutive bitmap images with 256 (8-bit) greyscale levels.

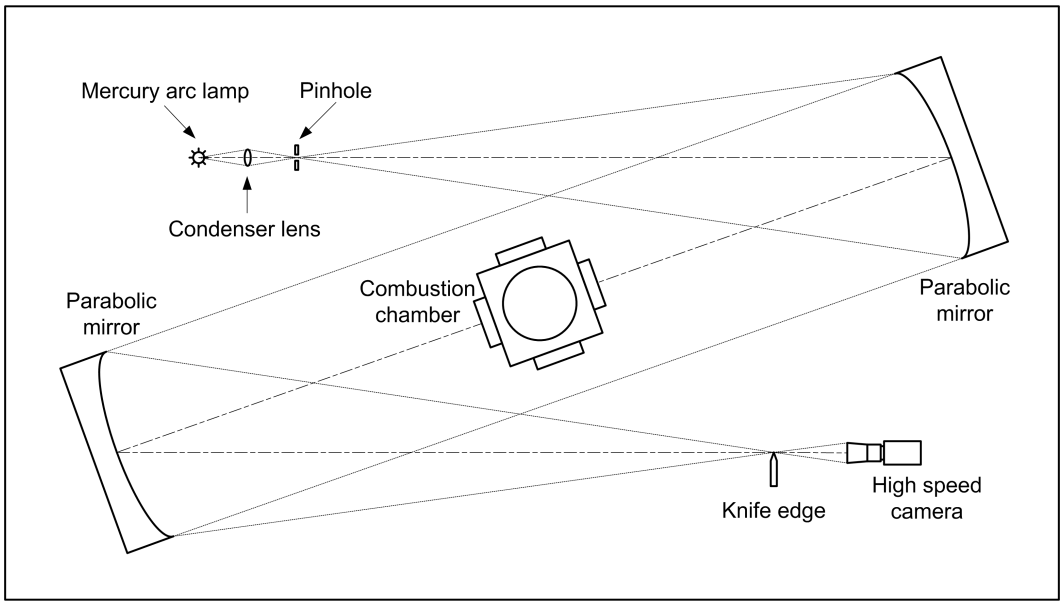

Figure 3.5: Schematic of the Z-type Schlieren system.

3.2.5 Instrumentation, synchronization, and data acquisition

While visualization provides direct access to localized details pertaining to the PSC injection and ignition behaviors, the overall combustion behavior inside the CVCC was also monitored. A thermalcouple recorded the pre-combustion temperature of the CVCC, to ensure the initial conditions were reasonable. Two pressure transducers, one diaphragm (differential) and the other piezoelectric, were used together to record the pressure rise resulting from ignition. The piezoelectric transducer was flush mounted to eliminate "ringing" signals, while a recess was introduced in the differential transducer port to minimize effects of thermal shock. The pressure data were sampled at 50 kHz. It was later found that the differential transducer alone could properly record the combustion pressure rise in the CVCC. A thermal mass flow meter was installed along the PSC gas line to measure the PSC mass flowrate, so that the modified Keihin KN3 injector could be characterized. Table 3.2 shows the instrumentation used in the CVCC, along with their operating range and uncertainties.

Table 3.2: Instrumentation for the CVCC.

Instrument	Make and model	Range	Uncertainty
CVCC pressure (static)	MSI US5100	0-70 bar (gauge)	0.1% F/S (7 kPa)
CVCC pressure (dynamic)	PCB Piezotronics 112A05	345 bar	0.5% F/S (1.73 bar)
CVCC temperature	K-type thermocouple	10 - 1600 K	2.2 K
PSC line pressure	MSI US5100	0-70 bar (gauge)	0.1% F/S (7 kPa)
PSC mass flowrate	MKS 179A-24C-S3BM	0 - 20 slm	0.6% F/S (0.12 slm)

The overall data and signal flow path of the experimental system is presented as a block diagram in Figure 3.6. A personal computer was used to handle various control sequences and data acquisition. An on-board timing card operating at 20 MHz synchronized all signal traffic. Through a LabView visual interface (Figure 3.7), the user could modify the control signals for the PSC injector, spark ignition, and the high-speed camera. Signals for the PSC injector and spark ignition were sent external arbitrary function generator, producing the necessary injector actuation signals for the high voltage driver box. Meanwhile, the high-speed camera came with a proprietary control and acquisition software, where the control signal from the interface was sent as a software trigger. The capture and storage of the camera images were also conducted separately through the proprietary software package.

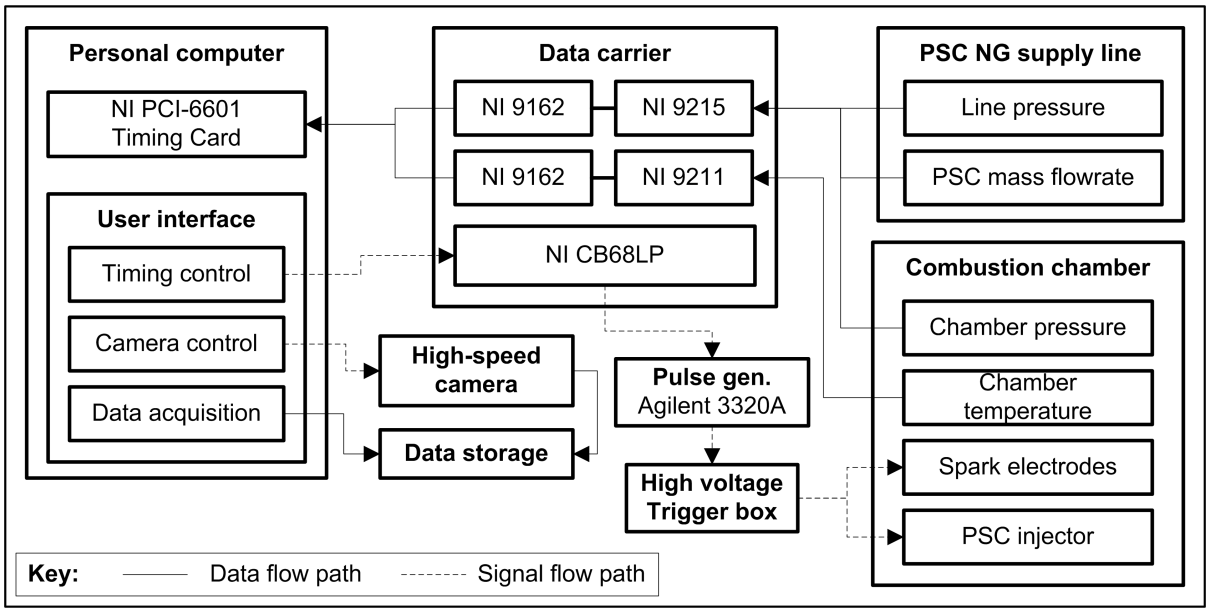

Figure 3.6: Block diagram for the signal and control system.

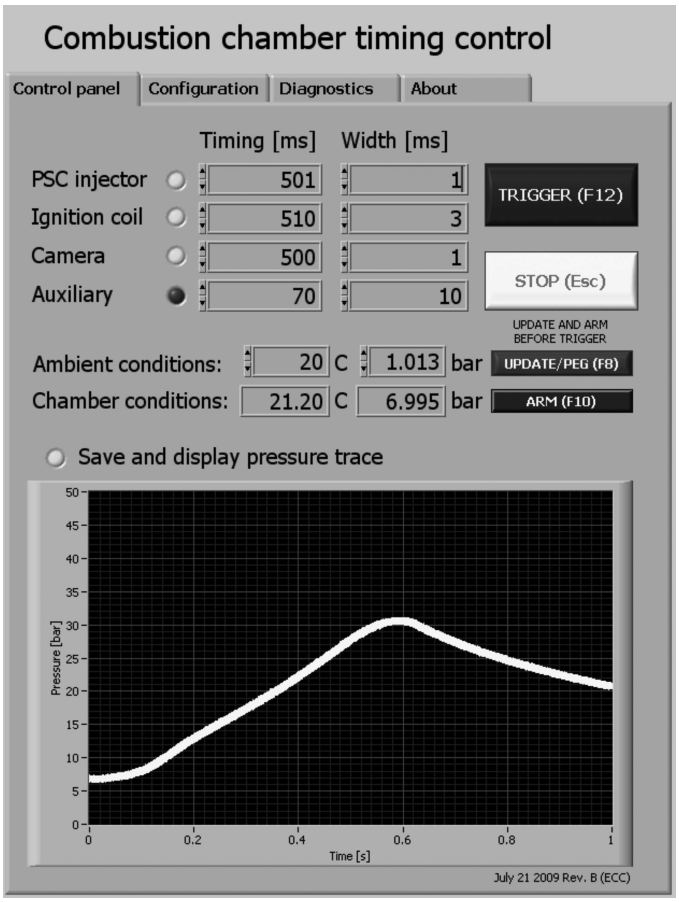

Figure 3.7: The user control panel, as a LabView visual interface.

3.3 Equipment calibration and characterization

A number of issues needed be addressed before the experimental setup became operational. In order to be used for quantitative analysis, the Schlieren system must be properly aligned, and the imaging systems was characterized so that physical measurements could be made on the images. As mentioned in Section 3.2.2, the injection mass flow rate was to be determined experimentally due to non-linear elements introduced in its modification. Finally, the implication from the PSC injection should also be examined, so that the bulk charge mixture composition would be compensated to achieve the desired overall air-to-fuel ratio.

3.3.1 Optical and imaging systems

The Schlieren optical components were aligned using a commercial sheet laser guide, which ensured the center of the CVCC view port coincided with the central axis of the light path. The horizontal rotation of the CVCC was also adjusted ensure a perpendicular alignment between the viewport and the incident light. The offset angles of both parabolic mirrors were also designed to be identical to minimize chromatic aberration. The alignment was verified by inspecting the camera image. The width and height of the raw captured image were 336 and 360 pixels respectively. A bounding box containing exactly the CVCC viewport was 274 by 275 pixels. Provided a 50.8 mm viewport diameter, this gave rise to a pixel metric of 0.18473 mm (width) and 0.18540 mm (height). The corresponding height-to-width aspect ratio was therefore 1.004, and thus the alignment was deemed sufficient.

3.3.2 PSC injector mass flowrate

Due to additional non-linearities introduced by the modifications, namely, the check valve and the non-uniform injection profile, the average mass flowrate of the PSC injector was measured experimentally. This presented a challenge, as the per-injection mass flowrate was expected to be small. The average mass flowrate could only be taken over a number of consecutive injections. On the other hand, the frequency response of the PSC injector was also expected to be non-uniform, so mass flowrate measurements taken at high frequencies (from engine tests, for example) would be inapplicable for single-shot settings, such as the CVCC.

Using a 179A-24C-S3BM thermal mass flow meter from MKS Instruments, the low-frequency injection was measured. A frequency of 1 Hz was selected, as the time elapsed was deemed sufficient for a full dissipation of injector coil energy between two injection signals, which allowed the PSC injector to behave effectively as a single-injection device. The injection pressure was fixed at 10 bar (abs.), while the chamber pressure was maintained at 5, 6, and 7 bar (abs.). Three

injection signal widths were also investigated, at 250μs, 500μs, and 1000μs. For each case, visual samples were taken, and the mass flowrate was taken at the steady-state frequency response. The injection event was also monitored with the high-speed Schlieren motion photography system, described in Section 3.2.4, so that the beginning and end of each injection could clearly be identified. A total of nine cases were considered, as tabulated on table 3.3.

The measured injection mass flowrates are presented in Table 3.4. The time lag between the start of the injection signal and the start of the injection is termed *injection delay*, and was found to be constant for all cases considered. The average injection delay was 1.037±0.0454 ms. The injection duration depended also strongly with the CVCC pressure, but the signal width had little effect. Meanwhile, the mass injected and the injection mass flowrate increased with the signal width but decreased with the chamber pressure.

The exception was case 3, where a notable increase was observed in duration and mass flow. A possible explanation was that the combination of pressure difference and injection signal width allowed the valve to fully open, while the valve was only partially open (to some degree) for the remaining cases. In other words, in this operating range, the PSC mass flow could not be viewed as a sole function of injection signal width, confirming the earlier assumption of non-linear injection behavior. Despite the slight implication, which would complicate subsequent efforts in analysis and modeling, the current PSC injector represented a significant improvement over the previous injector configuration (Mezo, 2008) under single-shot settings, as presented in Table 3.5.

Table 3.3: Cases considered for the PSC mass flowrate measurement.

Case	CVCC pressure [bar abs.]	Signal width [μs]	CVCC pressure (measured) [bar abs.]	PSC pressure (measured) [bar abs.]
1	5	250	$4.94\pm2.41\times10^{-4}$	$9.83\pm5.78\times10^{-4}$
2	5	500	$4.95\pm2.41\times10^{-4}$	$9.76\pm5.81\times10^{-4}$
3	5	1000	$4.96\pm2.40\times10^{-4}$	$9.77\pm6.34\times10^{-4}$
4	6	250	$6.03\pm2.20\times10^{-4}$	$9.76\pm4.88\times10^{-4}$
5	6	500	$5.99\pm2.20\times10^{-4}$	$9.76\pm4.99\times10^{-4}$
6	6	1000	$5.94\pm2.20\times10^{-4}$	$9.81\pm5.61\times10^{-4}$
7	7	250	$7.01\pm2.17\times10^{-4}$	$9.80\pm4.01\times10^{-4}$
8	7	500	$6.93\pm2.21\times10^{-4}$	$9.82\pm4.34\times10^{-4}$
9	7	1000	$6.94\pm2.21\times10^{-4}$	$8.77\pm4.80\times10^{-4}$

Table 3.4: PSC Mass flowrate measurements, with a 95% confidence interval.

Case	Injection delay [ms]	Inj. duration [ms]	Mass injected [mg / injection]	Mass flowrate [mg / s]
1	1.11±0.168	11.9±0.567	$0.422\pm5.78\times10^{-4}$	35.6±1.66
2	1.02±0.034	11.4±0.286	$0.423\pm5.81\times10^{-4}$	37.2±0.901
3	0.914±0.0569	12.2±0.117	$0.663\pm6.34\times10^{-4}$	54.3±0.353
4	1.00±0.0825	10.2±0.336	$0.356\pm4.88\times10^{-4}$	34.8±1.14
5	0.983±0.0680	10.2±0.462	$0.364\pm4.99\times10^{-4}$	35.6±1.83
6	0.967±0.0738	10.2±0.462	$0.409\pm5.61\times10^{-4}$	39.4±1.41
7	1.06±0.125	9.66±0.281	$0.292\pm4.01\times10^{-4}$	30.3±0.901
8	1.27±0.300	9.34±0.293	$0.317\pm4.34\times10^{-4}$	33.9±1.08
9	0.985±0.0317	9.90±0.415	$0.350\pm4.80\times10^{-4}$	35.4±1.49

Table 3.5: Comparison in PSC performance in a constant volume combustion chamber.

Study	Injector	Inj. signal	Inj. delay	Inj. duration	Mass injected
Mezo (2008)	Omega SV 121	8 ms	13.1 - 20.5 ms	52.4 - 102 ms	7.53 - 21.3 mg
Current study	Keihin KN3	1 ms	1.04 ms	9.90 - 11.9 ms	0.303 - 0.543 mg

3.3.3 PSC injection and overall air-to-fuel ratio

In order the maintain the desired overall air-to-fuel ratio, the additional mass introduced by the PSC injection must be taken into account when preparing the bulk mixture. Fortunately, the amount of PSC mass injection, discussed already in the previous section, proved to be small, so it was expected to have a negligible effect on the overall mixture strength. However, the validation of this assumption should be no less rigorous than other aspects of the present

research. The fuel properties for natural gas were taken from Wu (2009), represented by its mean molecular mass and molar stoichiometric air-to-fuel ratio. Meanwhile, the initial fuel mass in the CVCC could be estimated with the perfect gas law, evaluated at different pressures and air-to-fuel ratios. These values were summarized in Table 3.6. The by-mass percentage of the PSC injection of the overall fuel mass is presented in Table 3.7. It was obvious that the PSC charge, occupied less than 0.6% of the total charge by mass. As far as the range of pressures and air-to-fuel ratios were concerned, the compensation of the PSC mass in the overall charge calculation needed not be performed explicitly.

Table 3.6: Parameters used in the fuel charge mass calculation.

NG Mean molecular mass	16.2 g/mol
NG Stoichiometric molar AFR	9.44
Volume of CVCC	369 mL
Charge temperature	300 K
Charge pressure	5, 6, and 7 bar (abs.)

Table 3.7: Percentage of PSC injection of overall charge mass at 300K.

	Total NG charge [mg]			**PSC charge [% wt.]**		
AFR (λ)	**5 bar**	**6 bar**	**7 bar**	**5 bar**	**6 bar**	**7 bar**
1.0	115	138	161	0.305	0.254	0.218
1.2	97.2	117	136	0.360	0.300	0.257
1.4	84.3	101	118	0.415	0.346	0.297
1.6	74.4	89.3	104	0.470	0.392	0.336
1.8	66.6	79.9	93.2	0.525	0.438	0.375
2.0	60.3	72.3	84.4	0.581	0.484	0.415

3.4 Data processing

The amount of data collected in the experiment rendered manual intervention highly undesirable. Therefore the objective for data processing is to facilitate the automation of summary data extraction. The raw data, namely, the pressure trace and the Schlieren images, will require some form of processing for the information to become meaningful. From the rate of change in pressure, one could estimate the total energy release and the amount of fuel consumed in

the process. This, in turn, requires the removal of all signal noise, linear and non-linear, since they affect the quality of the numerical derivative. Similarly, the Schlieren images also require some level of manipulation. This is generally accomplished through edge detection, which extracts the evolution of the PSC jet and the subsequent ignited flame front. As all experimental observables are tainted with uncertainties from instrumentation to measurement, an overview of general statistical treatment is also included.

3.4.1 Energy release estimation

The quality of the combustion event can be gauged using the combustion energy release, and the corresponding combustion duration. The energy release represents the total additional energy resulting from the combustion reaction, and the combustion duration is the time between ignition to the point of maximum energy release. Though it is more common, particularly in engine experiments, to define the combustion duration as the time between 10% and 90% of the total heat release (Heywood, 1988), such alternate definitions existed for reasons of convenience, to provide definite reference points while obtaining the heat release. In the case of the CVCC, the pressure wave generated from the electrical spark was recorded as part of the combustion pressure trace, so the start of ignition could be clearly identified. Consequently, this allowed the combustion duration to be obtained in its entirety.

The rate of chemical energy released from the combustion in the CVCC can be expressed as a sum between the rates of change in internal energy of the system, flow work, and and heat loss to its surroundings:

$$\frac{dQ}{dt} = \frac{dU}{dt} + p\frac{dV}{dt} + \frac{dQ_{\text{ht}}}{dt}. \tag{3.6}$$

The ideal gas law can be assumed when considering the change in internal energy, assuming constant specific heat (c_v) and specific gas constant (R):

$$\begin{aligned}\frac{dU}{dt} &= c_v \frac{d}{dt}(mT) = \frac{c_v}{R}\frac{d}{dt}(pV) \\ &= \left(\frac{1}{\gamma - 1}\right)\frac{d}{dt}(pV) \\ &= \left(\frac{1}{\gamma - 1}\right)\left(p\frac{dV}{dt} + V\frac{dp}{dt}\right)\end{aligned}$$

Substituting the result above into Equation (3.6) yields:

$$\begin{aligned}\frac{dQ}{dt} &= \left(\frac{1}{\gamma - 1}\right)\left(p\frac{dV}{dt} + V\frac{dp}{dt}\right) + p\frac{dV}{dt} + \frac{dQ_{\text{ht}}}{dt} \\ &= \left(\frac{1}{\gamma - 1}\right)V\frac{dp}{dt} + \left(\frac{\gamma}{\gamma - 1}\right)p\frac{dV}{dt} + \frac{dQ_{\text{ht}}}{dt}\end{aligned}$$

As with all constant volume processes, the dV term vanishes, so the final expression for the heat release rate becomes:

$$\frac{dQ}{dt} = \left(\frac{1}{\gamma - 1}\right)V\frac{dp}{dt} + \frac{dQ_{\text{ht}}}{dt}. \tag{3.7}$$

Meanwhile, the heat loss can be estimated using the coefficient of heat transfer approach:

$$\frac{dQ_{\text{ht}}}{dt} = hA(\overline{T} - T_{\text{wall}}), \tag{3.8}$$

where h is the heat transfer coefficient, A is the burn gas surface area that is in contact with interior surface area of the combustion chamber, $\overline{T}$ is the mean burnt gas temperature, and T_{wall} is the initial wall temperature. Estimates for these parameters are difficult to obtain, so this term is summarily included in the energy release rate calculation, such that dQ/dt is implicit of losses from heat transfer. However, an implicit consideration of heat loss will render the experimental results more conservative, since the peak pressure and the corresponding

energy release are expected to be lower than the adiabatic case.

The energy release can be estimated by integrating Equation (3.7) from the ignition timing:

$$\Delta Q = \left(\frac{V}{\gamma - 1}\right) \int_{t_0}^{t_1} \frac{dp}{dt} dt, \tag{3.9}$$

where t_0 is the time of spark onset, and t_1 is the time when the peak pressure has been reached. At this point, all that is required is the rate of change in the chamber pressure, which can be obtained using the numerical derivative of the instantaneous pressure trace. Before proceeding, however, it is necessary to remove all forms of signal noise from the pressure trace, so that a smooth pressure trace can be produced to evaluate the numerical derivative.

3.4.2 Pressure signal processing

The raw pressure signal for the CVCC contains noises that, while acceptable for human inspection, heavily impede the automation of data processing. In the time domain, the raw signal (ϕ) is can be expressed as a superposition of the signal (φ), as well as linear (η), and non-linear (ξ) noise components:

$$\phi(t) = \varphi(t) + \eta(t) + \xi(t), \tag{3.10}$$

Linear noises. Linear noises refer to those that are uniformly applied to the signal at specific frequencies. Such noises that appear in the combustion pressure signal are of the high-frequency, low amplitude variety, and can be removed with a low-pass filter, $g(t)$. The filtering operation was performed in the frequency domain (ω), so that the convolution property of the Fourier transform could be used to reduce computational effort:

$$\phi(t) * g(t) = \mathscr{F}^{-1}\left[\Phi(\omega) \cdot G(\omega)\right]. \tag{3.11}$$

A Gaussian low-pass filter was constructed in the frequency domain to remove the high frequency noises. The filter is defined as follows:

$$G(\omega) = \exp\left[-\log(2)\left(\frac{\omega}{\omega_c}\right)^2\right], \tag{3.12}$$

where ω_c is the cutoff frequency, such that $G(\omega_c) = 1/2$. Since the Fourier transform of a Gaussian function is also a Gaussian function, the filtering operation will not introduce additional ripples, that commonly occur in window-function filters. It was found that a cutoff frequency of $\omega_c \approx 1200$ rad/s was optimal in separating noise from signal.

Non-linear noises. Unlike linear noises, non-linear noises are artifacts in the signal that occur at no specific frequency or shape. In the CVCC, the single source of non-linear noise comes from the ignition coil, where a high-amplitude pressure wave was captured by the pressure transducer at the spark timing. While the presence of the spark signal helped identify the start of ignition, its removal was also necessary so that the heat release rate could be properly integrated in this range.

A window median filter was used to distinguish the non-linear noise sources from the signal. A subsample (window) of the signal of fixed width was constructed around a point in time t_0. A comparison was then made between the magnitude of the signal at t_0 and the median of the corresponding subsample. An arbitrary but robust threshold could be set, so that the signal at t_0 could be rejected as noise if its magnitude was substantially higher than the window median. In the case of the pressure signals, the window size was to be large enough to cover at least two spark ignition periods, and the rejection threshold was set to two per cent of the median value.

Figures 3.8 and 3.9 show the various stages of signal filtering. The original, unfiltered combustion pressure signal is presented in Figure 3.8(A). While the high frequency (linear)

noises might be difficult to see from the figure, the non-linear noise from the spark signal could be clearly identified. The window median filter was able to take out the non-linear noise, as seen in Figure 3.9(A), while leaving the signal mostly intact. The high-frequency noises, shown in Figure 3.9(B), were isolated using the Gaussian low-pass filter. The application of the two filters resulted in the filtered pressure shown in 3.8(B), which could be used for automated data processing. More importantly, the peak pressure was also preserved, and as such the combustion heat release could be properly evaluated.

3.4.3 Digital image processing

With the proliferation of affordable digital imaging and processing equipment, aesthetic improvement of images for human inspection is but a trivial issue. Rudimentary image binarization techniques such as thresholding and, by extension, background removal will be more than adequate with manual intervention (Gonzalez and Woods, 2002; Shapiro and Stockman, 2002). Since the computer cannot instinctively identify features on an image, and with a large number of images, the ability to automate image processing becomes quite critical. The key, therefore, is the systematic reduction of the image to its essential features so that further processing would produce meaningful results. Any quantification of image features, such as flame front locations and PSC jet trajectories, can then be inferred by inspecting the respective defined *boundaries*. Therefore, edge detection serves as a reasonable starting point.

An edge detector, based on Canny (1986), is used to extract features from the image. The Canny algorithm first finds the edges through the image gradient. The edges are then refined and categorized into *textures*, which are discarded, and *features*, which are kept. Unlike simple thresholding and background removal methods, which identifies features based on intensity alone, the Canny detector considers the context of the edges through connectivity, thus providing some flexibility in the selection of features. Additional steps were also introduced to further

remove static structures not needed for analysis. The algorithm will be described succinctly below, and the results of each intermediate step is presented in Figure 3.10.

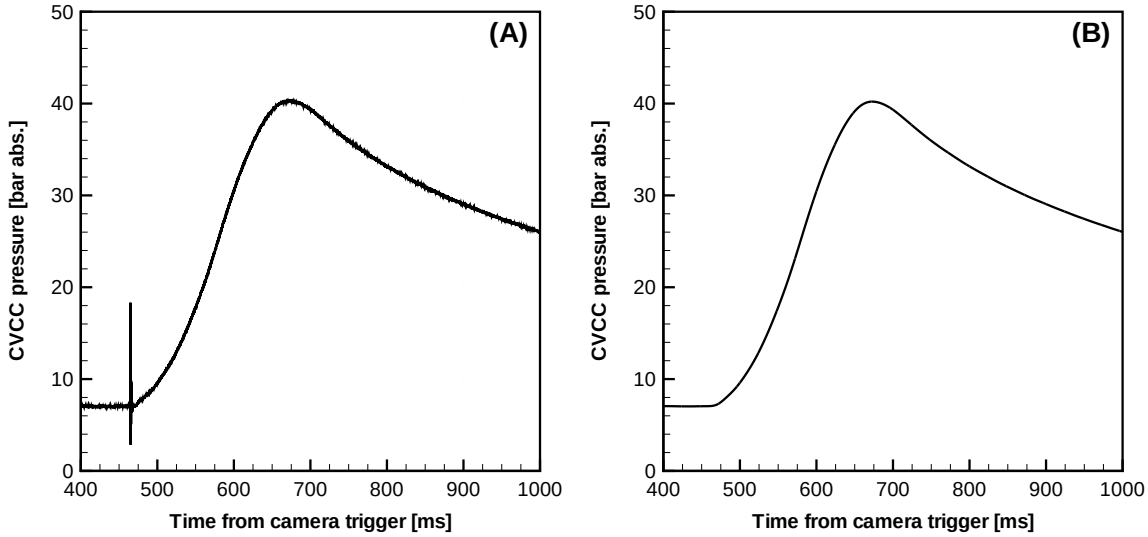

Figure 3.8: Pressure signal (A) before, and (B) after filtering.

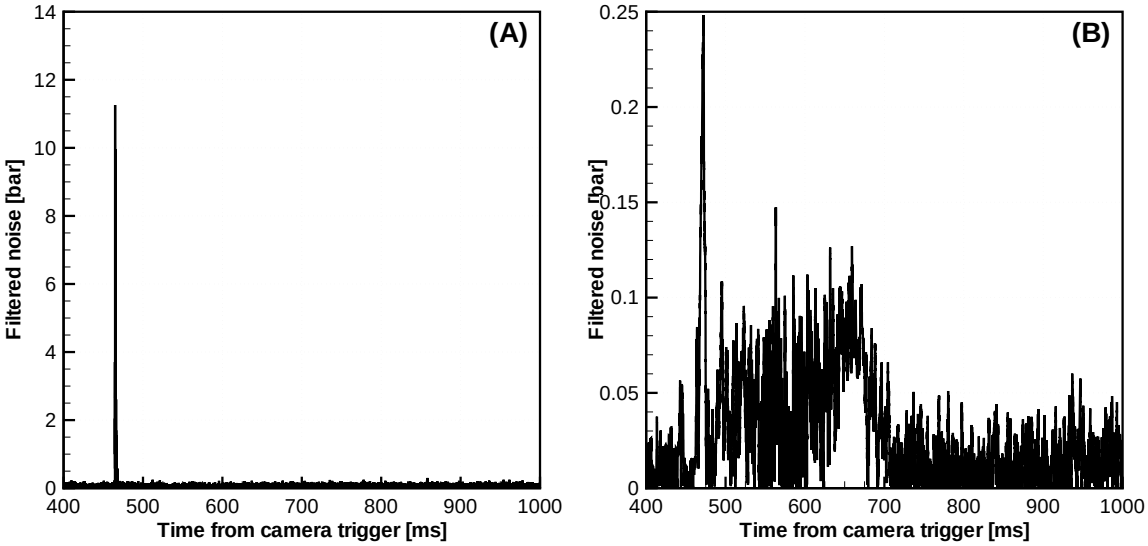

Figure 3.9: Noise components of the pressure signal extracted from (A) the window median filter, and (B) the Gaussian low-pass filter.

Gradients-of-Gaussian. Consider a normalized greyscale image, $I(x,y) \in (0,1)$, as presented in Figure 3.10(A). A gradients-of-Gaussian operation is applied to I to obtain the magnitude of

gradients, M, and the corresponding gradient normal, Θ:

$$M = |\nabla I| = \sqrt{(I * \nabla_x G)^2 + (I * \nabla_y G)^2} \tag{3.13}$$

and

$$\Theta = \tan^{-1}\left(\frac{I * \nabla_y G}{I * \nabla_x G}\right), \tag{3.14}$$

where

$$G = \frac{1}{2\pi\sigma^2}\exp\left(-\frac{x^2+y^2}{2\sigma^2}\right), \tag{3.15}$$

has a standard deviation σ, which depends on the image scale. Note that $I * \nabla G = \nabla I * G$, so the gradients-of-Gaussian operation is effectively a Gaussian low-pass filter applied to the gradient (or edges) of the image. This maximizes the signal-to-noise ratio, while maintaining good localization of the response (Tagare and Figueiredo, 1990). Since an analytical expression is available for ∇G, discretization errors resulting from calculating ∇I can also be eliminated. Figure 3.10(A) shows the original image, and Figure 3.10(B) illustrates the results after the gradient-of-Gaussian operation.

Non-maxima suppression. An edge defined over multiple pixels will, as a result, generate multiple edge responses with a gradient type edge detection. *Non-maxima suppression* serves to remove all duplicate edge responses along the direction of the gradient (Θ) that are not local peak values in gradient magnitude (M). In practice, one can take advantage of the pixelated nature of the image, and discretize the gradient normal into four sections:

$$\begin{pmatrix} 3 & 2 & 1 \\ 0 & x & 0 \\ 1 & 2 & 3 \end{pmatrix}. \tag{3.16}$$

The location of the pixel is represented by x. Also note that the *sense* of the gradient normal is irrelevant, since neighbors will be extracted from *both* sides of the normal. As a result, only

four sectors will be needed, and the discretized gradient normal will be denoted as $\hat{\Theta}$. For each pixel location (x, y), a 3×3 window passes over M, which will be compared with the two neighbors defined by $\hat{\Theta}$. The magnitude at (x, y) will be set to zero if it is not the local maximum. The intermediate result after non-maxima suppression is shown on Figure 3.10(C).

Hysteresis thresholding. At this point of the algorithm, the image is reduced to a map of unique edge responses of magnitude M. It still contains many spurious edge segments due to noise and other irrelevant details. These are known as *textures* and they are typically plentiful but with low gradient magnitudes. Edges that define *features* are rare compared to the textures, but they occur usually at higher gradient magnitudes. A histogram of gradient magnitude distribution, taken from a composite of processed edge images, is presented in Figure 3.11, illustrating the observations on feature and texture edges.

It is also found that naturally exposed images (as opposed to artificially generated images) follow a similar gradient magnitude distribution as Figure 3.11 (Crigorescu et al., 2004). Based on this, thresholds levels based on M can be set manually to identify magnitudes for textures and features, denoted as T_t and T_f respectively. Edges with $M < T_t$ will be rejected as textures, while those with $M > T_f$ will be included as features. For the remaining edges, where $T_t \leq M \leq T_f$, only those connected to a previously identified feature will be kept. The use of two thresholds provides additional flexibility, which reduces the inclusion of unwanted edges, as well as the rejection of otherwise wanted edges. Typically the texture threshold is set to 10% of the maximum gradient magnitude, and 20 - 25% for the feature threshold (Crigorescu et al., 2004). Figure 3.10(D) shows the result after hysteresis thresholding, which also concludes the Canny edge detection algorithm.

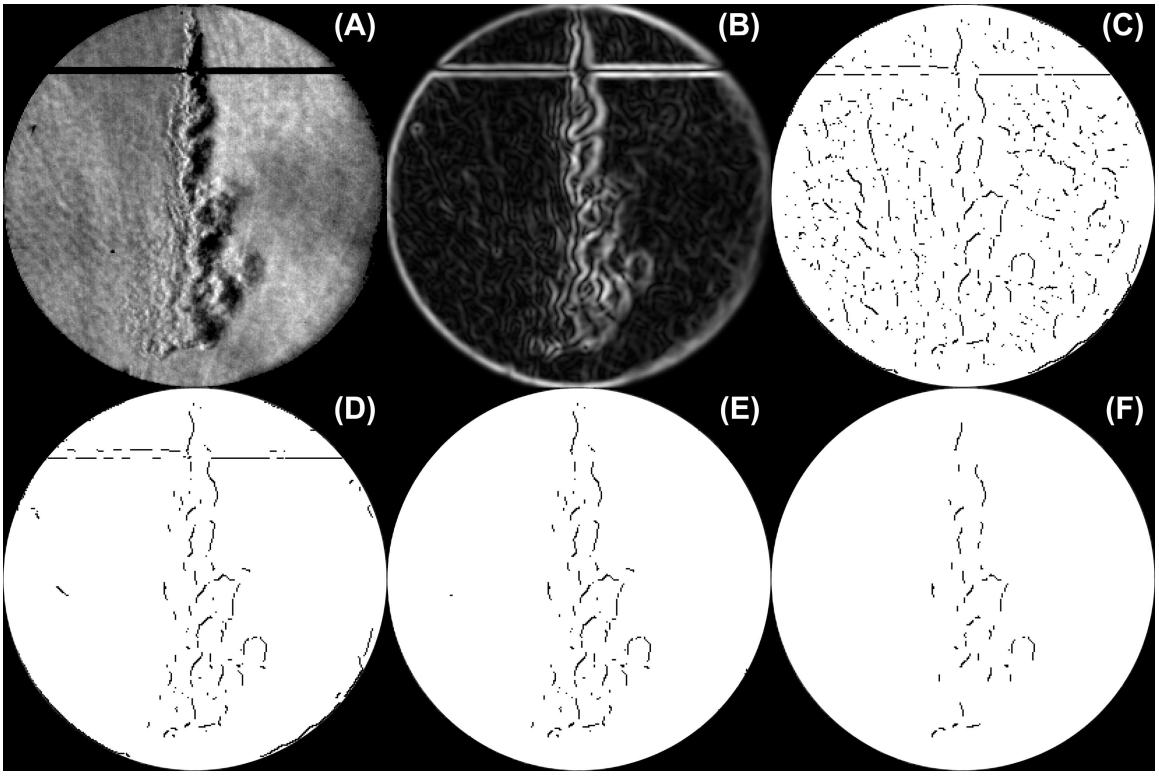

Figure 3.10: Results of the edge feature extraction: (A) original image, (B) after gradient-of-Gaussian operation, (C) after non-maxima suppression, (D) after hysteresis thresholding. (E) Removal from background structures from (D), and (F) after cluster isolation.

Static feature removal. Though the Canny algorithm successfully removes much of the unnecessary information from the image, some features that are not needed for analysis still remain. These include boundaries from the electrodes and the viewport, stains from earlier test runs (but were too inconvenient to clean up right away), as well as various optical artifacts. Many of these features represent static structures that remained throughout each experiment, and background removal techniques can be applied. Let E^0 be a sample of background edge images, which is taken as the union of the edge image of the initial n frames of each test, $E_0^0, E_1^0, ...E_n^0$, before injection or ignition takes place:

$$E^0 = \bigcup_{i=0}^{n} E_i^0. \tag{3.17}$$

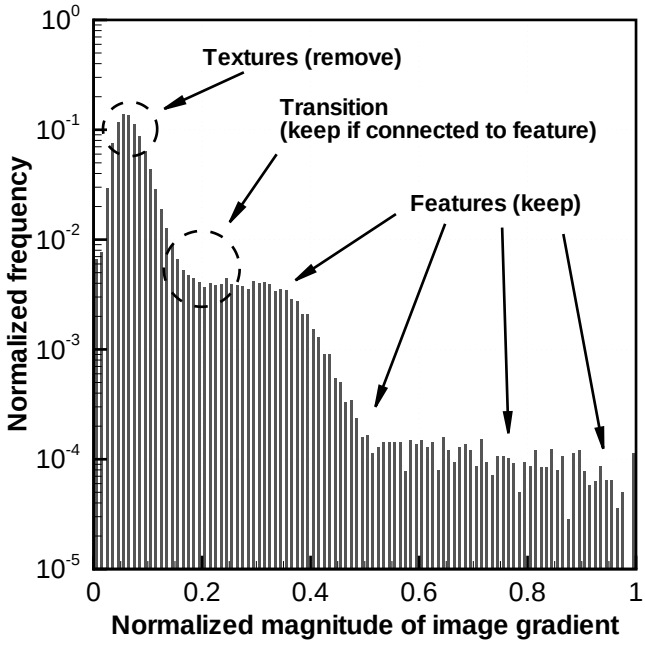

Figure 3.11: A histogram of gradient magnitude of an edge image after non-maxima suppression. Features, textures, and transitional regions are identified.

The background feature components of each image, E_j, can be removed with additional boolean operations. Since the background E^0 contains multiple responses for background edges through the aforementioned union operation, the response specific for the image E_j is its intersection between E^0. The features of interest can then be obtained with a second boolean operation between E_j and the result from the background extraction step. The overall process can be represented with the operation below:

$$E_j^* = E_j \cap \overline{(E_j \cap E^0)},$$

where E_j^* is the background-free edge image. Application of de Morgan's theorem yields:

$$E_j^* = E_j \cap (\overline{E_j} \cup \overline{E^0}) = E_j \cap \overline{E^0}. \tag{3.18}$$

After this, a rudimentary clustering method is used to isolate and remove any outlying, unwanted features. The edge image is first divided into clusters (of 3×3 pixels, for instance). Clusters showing no connectivity to other clusters will be culled from the edge image. The results of the background edge removal and clustering are shown on Figure 3.10(E) and 3.10(F), respectively. The edge detection method was used to extract the penetration and spread of the PSC jet. The penetration could be obtained by identifying the edge furthest away from the nozzle along the central axis of the injection. Correspondingly, the spread is the radial edge furthest away from the same central axis.

3.4.4 Stochastic treatment of experimental data

In frequentist analysis, experimental observables are expressed in terms of confidence intervals. For a sample of size N, with a mean point estimate $\overline{X}$, and a standard error $S/\sqrt{N}$, the mean of the population, μ, expressed in terms of a fixed interval about $\overline{X}$:

$$\mu = \overline{X} \pm t_{\nu}^{(1-\alpha)} \frac{S}{\sqrt{N}}, \tag{3.19}$$

where t is the standard variable for the t-distribution, with a degree of freedom of $\nu = N - 1$. An arbitrary *level of significance*, α, determines the rejection criterion of the sample mean. A popular choice is $\alpha = 0.05$, symmetric about μ, which gives rise to the *95% confidence interval*.

Since the t-distribution is used, it is noteworthy to devote a very brief discussion on this subject. The probability density function for this distribution is:

$$f(t|\nu) = \frac{1}{\sqrt{\pi\nu}} \frac{\Gamma\left[\frac{1}{2}(\nu+1)\right]}{\Gamma\left(\frac{\nu}{2}\right)} \left(1 + \frac{t^2}{\nu}\right)^{-\frac{1}{2}(\nu+1)}. \tag{3.20}$$

Using Stirling's approximation to evaluate $\Gamma(x)$ for large values of x:

$$\Gamma(x) \approx \sqrt{\frac{2\pi}{x}} x^x \exp(-x), \tag{3.21}$$

it can be shown that, as ν goes large:

$$\begin{aligned}
\lim_{\nu\to\infty} f(t|\nu) &= \frac{1}{\sqrt{\pi\nu}} \frac{\sqrt{\frac{4\pi}{\nu+1}} \exp\left[\frac{1}{2}(\nu+1)\right] \left[\frac{1}{2}(\nu+1)\right]^{\frac{1}{2}(\nu+1)}}{\sqrt{\frac{4\pi}{\nu}} \exp\left(\frac{\nu}{2}\right) \left(\frac{\nu}{2}\right)^{\frac{\nu}{2}}} \left(1+\frac{t^2}{\nu}\right)^{-\frac{1}{2}(\nu+1)} \\
&= \frac{1}{\sqrt{2e\pi}} \underbrace{\left(\frac{\nu}{\nu+1}\right)^{\frac{1}{2}} \left(\frac{\nu+1}{\nu}\right)^{\frac{1}{2}(\nu+1)}}_{=\sqrt{e}} \underbrace{\left(1+\frac{t^2}{\nu}\right)^{-\frac{1}{2}(\nu+1)}}_{=\exp\left(-\frac{t^2}{2}\right)} \\
&= \frac{1}{\sqrt{2\pi}} \exp\left(-\frac{t^2}{2}\right).
\end{aligned}$$

So the normal distribution is, indeed, a limiting case of the t-distribution at an infinite degrees of freedom. In practical terms, however, the difference between the two distributions diminishes rapidly when $\nu \sim 30$ and beyond. The number of samples taken for each test points has also been set accordingly to exploit this fact.

Additional measurement uncertainties can be introduced from instrumentation. Consider an experimental observable, $\varphi(\boldsymbol{x})$, a function of a number of independently measured parameters, $\boldsymbol{x}$. Let $\boldsymbol{x}_0$ be the values of $\boldsymbol{x}$ such that $\varphi(\boldsymbol{x}_0) = \varphi_0$, the difference $\varphi - \varphi_0$ can be expressed as a multivariate Taylor series expansion of φ about $\boldsymbol{x}_0$:

$$\varphi - \varphi_0 = \sum_{n=1}^{\infty} \frac{\nabla^n \varphi(\boldsymbol{x}_0) \cdot (\boldsymbol{x} - \boldsymbol{x}_0)^n}{n!}. \tag{3.22}$$

Provided that $\boldsymbol{x} - \boldsymbol{x}_0$ is sufficiently small, that is, $\boldsymbol{x} - \boldsymbol{x}_0 \ll \boldsymbol{x}$, the right hand terms beyond the first derivative can be neglected:

$$\varphi - \varphi_0 \approx \nabla\varphi(\boldsymbol{x}_0)\cdot(\boldsymbol{x} - \boldsymbol{x}_0) \tag{3.23}$$

The difference $\boldsymbol{x} - \boldsymbol{x}_0$, often referred to as $\boldsymbol{\omega}$, can be effectively regarded as the uncertainty in the measurement in $\boldsymbol{x}$. This produces a corresponding uncertainty in the observable, defined as $\delta\varphi = \varphi - \varphi_0$. A conservative magnitude of $\delta\varphi$ can be estimated using the Schwarz inequality:

$$\langle\delta\varphi, \delta\varphi\rangle \leq \langle\nabla\varphi\cdot\boldsymbol{\omega}, \nabla\varphi\cdot\boldsymbol{\omega}\rangle \tag{3.24}$$

or, in a more familiar form:

$$\left\|\delta\varphi\right\|_2 \leq \left\|\nabla\varphi\cdot\boldsymbol{\omega}\right\|_2, \tag{3.25}$$

which is the L_2 norm over all the uncertainties in measurement.

3.5 Summary

An idealized geometry was adopted to allow a detailed study on the enabling mechanisms of PSC injection and ignition in an axisymmetric geometry. The constant volume combustion chamber was subsequently commissioned to accommodate visualization experiments under this arrangement. The evolution of the PSC injection, ignition, and combustion was captured using high-speed Schlieren motion photography.

The PSC injection was metered by a CNG port injector, modified to reduce mass flowrate and improve injection time response. A customized high-voltage injector driver provided sufficient energy for the injector to operate at elevated injection pressures. Preignition injection testing indicated substantial improvement from previous PSC injector implementations in

terms of injection timing and mass flow control. Consequently, the amount of PSC charge reduced to less than 0.6 % of the total fuel mass at an ultra-lean level.

Data acquisition and signal synchronization were managed by a personal computer with peripheral modules to handle data carriage and timing control. The experiment data were digitally stored and processed to render them suitable for automated analyses. Noise signals from the combustion pressure traces were removed using a combination of linear and non-linear filters, while the salient features from the Schlieren images were extracted through image edge detection.

Chapter 4

Experimental results

Following the discussion of the experimental framework, the experimental program was formulated to investigate the various aspects of the PSC ignition strategy. In particular, the injection method, spark ignition timing, and the bulk mixture fuel concentration were points of interest. The overall quality of the combustion process could be inferred from the pressure history, and the salient features of flame evolution could be observed from the Schlieren images. The data quantify the enhancement introduced by PSC and identify its principal enabling mechanisms.

4.1 Experimental parameters

The experimental parameters are separated into two categories, *fixed* and *adjustable* parameters. Fixed parameters are those that are held constant throughout. They arose mainly from the limitations in the experimental equipment. The other category, the adjustable parameters, refers to those from which changes in combustion behavior could be observed or examined.

4.1.1 Fixed parameters

A number of parameters have been held constant throughout the experiment. The first set of fixed parameters came from geometrical constraints of the constant volume combustion chamber. As mentioned in Section 3.2.1, the spark electrodes could not be changed easily as a result of the design of the chamber. The spark gap, fixed at 1 mm, was positioned along the axis of symmetry of the combustion chamber to preserve a axisymmetric ignition behavior. The axial location of the spark was also fixed at 10 mm downstream of the PSC nozzle. This ensured

the turbulent core of the PSC jet could cover the spark gap entirely. The spark duration has also been fixed at 3 ms, as it was deemed a sufficiently long under most automotive conditions (Maly, 1984).

The other set of fixed parameters are results of limitations in the PSC injector. Empirical tests suggested a maximum operating pressure difference of about 10.9 bar across the injector. In practice, the pressure difference was kept low enough such that the injection duration could be minimized. This is evidenced by a sudden increase in mass flow rate, noted in Table 3.4, when the CVCC pressure was dropped to 5 bar (abs.). As a result, the PSC injection pressure was kept at 10 bar (abs.), and the initial chamber pressure was kept at 7 bar (abs.). The injection signal was set to 1 ms, such that the resulting injection duration would be 9.9 ms. The fixed parameters and their respective values are summarized in Table 4.1.

Table 4.1: Parameters held constant throughout the experiment.

Spark gap	1 mm
Spark location from PSC nozzle	10 mm
Spark duration	3 ms
PSC injection pressure	10 bar (abs.)
Initial CVCC chamber pressure	7 bar (abs.)
PSC injection duration	9.9 ms

4.1.2 Variable parameters

The remaining parameters were adjustable, and served to examine the the role of chemistry and turbulence in modifying combustion behavior. First and foremost was the fuel concentration of the bulk mixture. A mixing chamber, described in Section 3.2.3, allowed the mixture to be prepared at different relative air-to-fuel ratios (λ), using the partial pressure approach. For the experiments, the relative air-to-fuel ratios ranged from $\lambda = 1.2$ to $\lambda = 2.0$.

Though the injection amount and duration had been kept constant, as discussed in the previous section, the effects of hydrodynamics on ignition could still be examined by varying the spark timing relative to the PSC injection. Preliminary experimentation indicated that ignition would lead to combustion only at the beginning and the end of the PSC injection. This is likely to be a consequence blow-off due to high bulk velocity in the PSC jet during the injection period. They were referred to as the SOI and EOI spark timings respectively. The SOI spark timing was defined at the moment when the PSC jet enters the combustion chamber, which typically took place about 1 ms after the injection signal (see Table 3.7). On the other hand, the EOI spark timing was set shortly before the cessation of the PSC injection, at 9 ms after SOI.

Single and double PSC injection

During the early stages of experimentation, under the EOI spark timing, the spark signal would occasionally trigger a second PSC injection after the spark. Though initially perceived as an externality, the benefits of the second injection could be observed from the Schlieren images and the pressure history. In time, the problem was solved by improving shielding around the spark cables. An arbitrary function generator replaced the role of spark signal noise, allowing the combustion behavior to be investigated under one or two PSC injections. Under this implementation, the two injections were identical.

Since the injection duration of each PSC injection was 9.9 ms, the double injection method would only be feasible if the two injection signals were at least 9.9 ms apart. For the experiments, the two injections are commanded at 10 ms from each other, at the same pulse width of 1 ms. The spark took place at the designated EOI spark timing, 9 ms after the start of the first injection. The double injection case will be referred to as EOI×2 throughout the study, to distinguish this case from the single injection EOI case.

4.1.3 Test matrix

Table 4.2 shows all the cases considered in the experiment. Each test point was repeated 30 times, such that the each observable could be regarded as normally distributed*. The three PSC cases introduced in Section 4.1.2 (SOI, EOI, and EOI×2), were executed at relative air-to-fuel ratios from $\lambda = 1.2$ to $\lambda = 2.0$. Energy release analysis up to this point suggested no significant statistical evidence that the SOI and the single injection EOI results were different at $\lambda = 1.2$ and $\lambda = 1.4$. Therefore, no double injection EOI cases was performed at these relative air-to-fuel ratios.

In addition, for the purpose of comparison, a baseline case was introduced, where the homogeneous mixture was ignited without the use of the PSC jet. The baseline experiments serve two functions. Firstly, they provided a rough idea of how the combustion would proceed. This was particularly important when the mixture was near stoichiometric, where the combustion took place quickly without the aid of PSC. Second, they also gave a good estimate on the lower (lean) flammability limit of the homogeneous mixture. Consistent failure to reach combustion was observed experimentally at $\lambda = 1.8$ and beyond. No baseline tests were performed at these levels as a result.

Table 4.2: Final experimental schedule.

λ	**No PSC**	**PSC SOI**	**PSC EOI**	**PSC EOI×2**
1.2	✓	✓	✓	
1.4	✓	✓	✓	
1.6	✓	✓	✓	✓
1.8		✓	✓	✓
2.0		✓	✓	✓

*The t-distribution would still be used for the calculation of standard error, however.

4.2 Overall combustion characteristics

The overall combustion quality could be inferred by inspecting the instantaneous pressure history and the estimated energy release. The detection of the spark signal marked the start of combustion, which was considered complete when the chamber pressure reached a maximum value. The time elapsed between the two events was defined as the combustion duration. The energy release during combustion could be estimated using the first law of thermodynamics. The methods of post-processing have been discussed in Sections 3.4.1 and 3.4.2.

4.2.1 Normalized groups

The summary results were normalized to provide a consistent and uniform basis for comparison. These dimensionless groups include pressure, energy, and combustion duration. The initial chamber pressure (p_i) is used to normalize the pressure history as prescribed in the equation below:

$$\tilde{p} = \frac{p - p_i}{p_i}, \tag{4.1}$$

where $\tilde{p}$ is the normalized pressure, and p_i is the initial pressure of the mixture in the combustion chamber. Using $\tilde{p}$ instead of p has the advantage of eliminating any variability the initial pressures in all the test cases. Since p_i is (more or less) constant throughout the study, $\tilde{p}$ shall exhibit identical trends as energy release in for the constant volume combustion chamber.

The energy release could be normalized using the energy content of the mixture:

$$\tilde{Q} = \frac{\Delta Q}{E}. \tag{4.2}$$

Since the mixture was lean for all experimental cases considered, the fuel energy content E could be estimated directly as the product between the mass of the fuel, and its lower heating value (LHV). Using the natural gas composition data provided by Westport Innovations, Inc.

(Wu, 2009), the lower heating value for natural gas was 49.10 MJ/kg. The fuel mass in the combustion chamber could be estimated using the ideal gas relation. An initial absolute pressure of 7 bar and a temperature of 280 K were representative of the initial conditions throughout the experiment. The energy content of the bulk mixture was between 7.16 kJ at $\lambda = 1.2$ and 4.44 kJ at $\lambda = 2.0$. The energy contained in each 0.35 mg PSC injection is approximately 17.19 J.

A time scale is also defined to normalize the combustion duration. A reasonable scale could be the time for a laminar flame to travel across the combustion chamber. As the flame kernel expansion is an isobaric process (Maly, 1984) at the higher temperature than the unburnt mixture, the density disparity between the flame kernel and the bulk mixture should also be taken into account. So the characteristic time scale becomes:

$$\tau = \left(\frac{\rho_b}{\rho_u}\right)\left(\frac{V^{1/3}}{S_L}\right). \tag{4.3}$$

The characteristic length scale can be taken at the cube root of the combustion chamber volume. The laminar flame speed, S_L, can be evaluated as a one-dimensional stationary flame problem, using detailed chemical kinetics for natural gas (Smith et al., 1999). The densities for the corresponding burnt (ρ_b) and unburnt (ρ_u) regions can be calculated with the NASA thermophysical database (McBride et al., 1993). A C++ code was written using Cantera (Goodwin, 2007) for this purpose. The results are summarized in Table 4.3.

It is noteworthy to comment on the role of S_L in the calculation of τ. The initiation of the flame kernel is, in effect, a competition between combustion energy release and heat loss to its surrounding, radiation heat transfer in particular (Chen and Ju, 2007). This is the ultimate criteria in determining of the flammability limit of a air-fuel mixture (Law, 2006). As heat transfer has been excluded in the numerical calculation, under this approach, the flammability limit is instead dictated by the adiabatic flame temperature. A flame is self-sustaining and propagates

when the adiabatic flame temperature is greater than the auto-ignition temperature. At the current initial temperature and pressure (280K and 7 bar), the limit, extrapolated from the computed data, is located at $1/\lambda \approx 0.22$, or $\lambda \approx 4.5$, as illustrated in Figure 4.1.

Table 4.3: CVCC bulk charge properties and characteristic scales.

λ	S_L [cm/s]	T_{ad} [K]	ρ_b/ρ_u [ ]	m_{fuel} [mg]	E [kJ]	τ [ms]
1.2	11.62	2052	0.1372	145.8	7.159	84.64
1.4	7.026	1862	0.1353	126.5	6.209	138.1
1.6	4.543	1711	0.1360	111.6	5.481	214.7
1.8	3.092	1589	0.1784	99.91	4.906	413.9
2.0	2.192	1487	0.1913	90.42	4.440	625.8

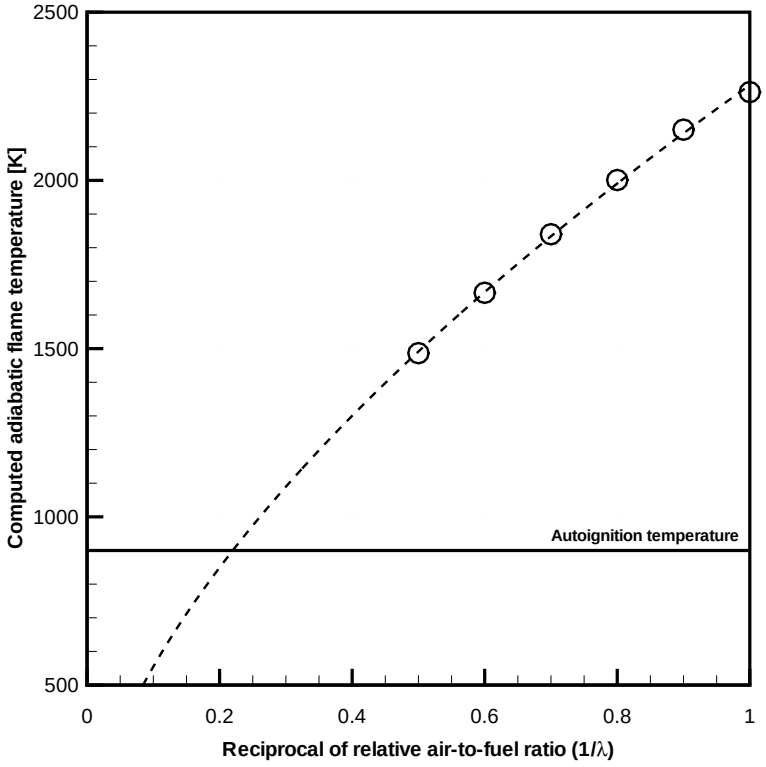

Figure 4.1: Adiabatic flame temperature for natural gas at an initial pressure 7 bar and temperature of 280 K. Key: ∘ Numerical results from GRI-Mech 3.0 (Smith et al., 1999); - - Best-fit curve.

4.2.2 Combustion duration and energy release

The discussion of the experimental results begins with the instantaneous pressure data. The combustion energy release can be estimated by integrating Equation (3.7). The combustion duration results are tabulated in Tables 4.4 and 4.5. The pressure and estimated energy release data are presented in Tables 4.6 to 4.9. They are graphically presented on Figures 4.2 to 4.5. All results include a 95% confidence interval about the mean.

Combustion duration. From Figure 4.2, it can be seen that, when the relative air-to-fuel ratio is close to unity (λ =1.2 and 1.4), the combustion duration was about the same for all cases. This is indicative of a sufficiently high flame speed in the bulk mixture, that the additional fuel introduced from the PSC jet did little to modify it. In the baseline conditions, the combustion duration increased rapidly with λ, which also reflects a drastic decrease in the laminar flame speed, and that, in the absence of turbulence, molecular transport became the only means of flame front propagation. Thus the immediate benefit of the PSC ignition method was the reduction of the combustion duration.

Additional details can be obtained by examining the dimensionless timing in Figure 4.3. The characteristic time τ represents the time for a laminar premixed flame to consume the contents in the combustion chamber. So the ideal normalized combustion duration would approach unity. A value greater than one indicates an inefficiency in combustion. It was apparent, from Figure 4.3, that for the PSC cases, the normalized combustion duration followed a parabolic trajectory with air-to-fuel ratio, peaking at $\lambda \approx 1.6$ before approaching below unity at $\lambda = 2.0$. At first glance, a less-than-unity burn duration might represent an improvement. since the bulk mixture was quiescent, such cases were likely to indicate prematurely terminated combustion.

Pressure rise and energy release. The discussion on pressure rise could be effectively regarded as the same as that for energy release, as they exhibited identical behaviors in a constant

volume setting. Figures 4.4 and 4.5 show the energy release estimated by integrating Equation (3.7). A decrease in released energy was expected to decrease with λ. There were two reasons for such observation. First is the reduction in fuel mass, which resulted in a corresponding reduction in energy output. Such is critical from a load control standpoint. The second factor was heat loss, which was dependent on geometry and the rate of combustion.

When normalized with the energy content of the fuel charge, the energy release reflected the net amount of work output. From Figure 4.5, even at $\lambda = 1.2$, where complete combustion was likely to occur, the heat transfer losses, according to the normalized energy release, account for approximately 37% of the total energy content. The figure dropped with increasing λ, first as a result of prolonged interaction with the combustion chamber surface, which increased heat loss to the chamber walls during combustion of the mixture. Second was the possibility of incomplete combustion. For the cases considered, as presented in Figures 4.4 and 4.5, the combustion duration would increase with λ until it reached a peak, and began to decrease from that point forward. Since the speed of flame propagation decreases with air-to-fuel ratio, a decrease in combustion duration was indicative of premature termination of combustion reaction.

Quantifying heat transfer and the completeness of combustion, however, were confounded by the use of pressure history as the sole means of evaluating energy release, and therefore could not be easily separated. As heat loss decreased the flame temperature, it also increased the reaction time, which further resulted in additional heat loss. Therefore, it was expected that the effect heat transfer would significantly impede the consumption of the bulk mixture as it was further leaned out. This eventually led to a premature termination of the combustion reaction (i.e., partial combustion).

Table 4.4: Combustion duration for all cases, in milliseconds.

λ	**No PSC**	**PSC SOI**	**PSC EOI ×1**	**PSC EOI ×2**
1.2	85.01±1.125	87.34±6.044	93.62±5.589	
1.4	204.7±6.969	196.7±27.34	189.1±24.02	
1.6	566.2±27.68	312.2±36.03	312.2±24.58	288.9±19.25
1.8		506.4±13.92	440.3±20.11	409.4±24.41
2.0		338.4±22.98	426.7±12.69	435.8±11.96

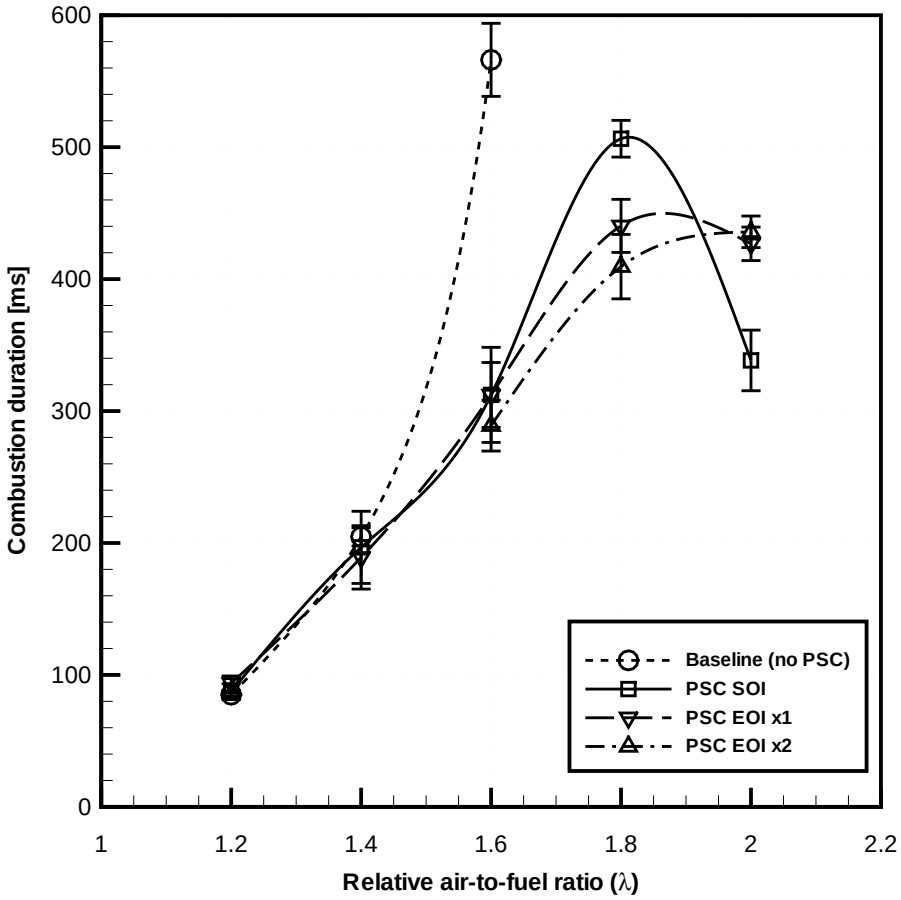

Figure 4.2: Combustion duration for all cases.

Table 4.5: Normalized combustion duration for all cases.

λ	**No PSC**	**PSC SOI**	**PSC EOI ×1**	**PSC EOI ×2**
1.2	1.004±0.01329	1.032±0.07140	1.106±0.06603	
1.4	1.481±0.05045	1.424±0.1979	1.369±0.1739	
1.6	2.637±0.1289	1.454±0.1678	1.454±0.1145	1.346±0.08964
1.8		1.224±0.03364	1.064±0.04860	0.9893±0.05899
2.0		0.5407±0.03671	0.6819±0.02028	0.6964±0.01912

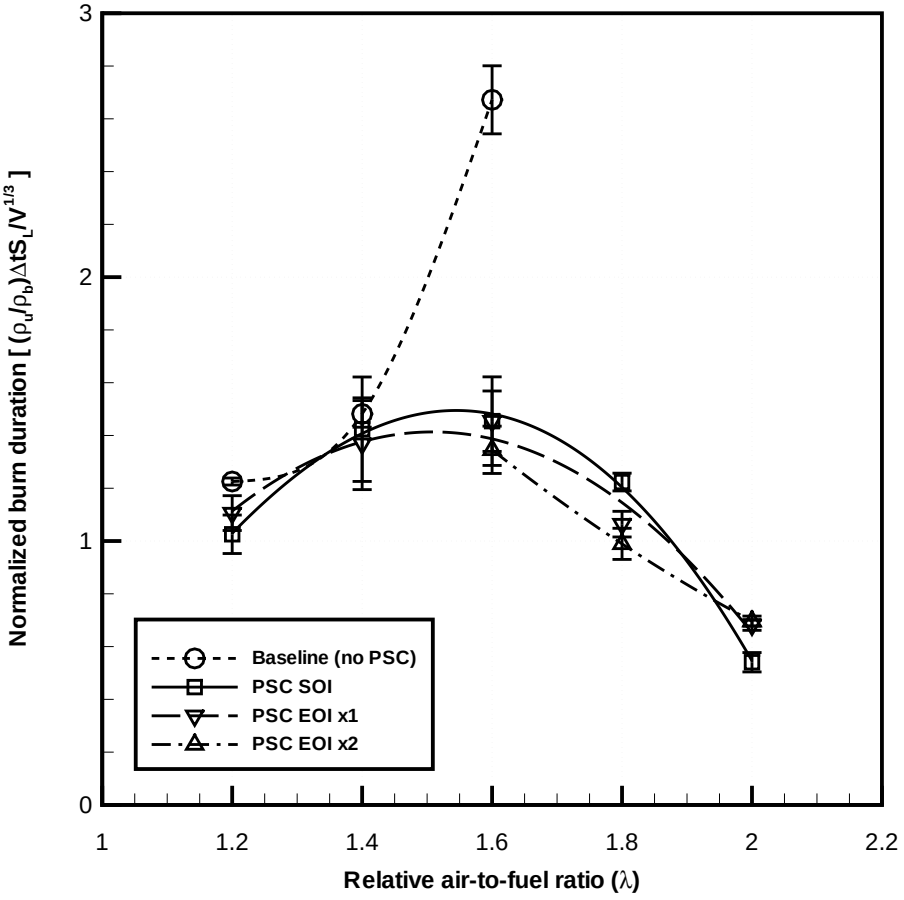

Figure 4.3: Normalized combustion duration for all cases.

Table 4.6: Combustion pressure rise for all cases, in bars.

λ	No PSC	PSC SOI	PSC EOI ×1	PSC EOI ×2
1.2	40.07±0.7697	40.83±0.6882	40.33±0.6752	
1.4	30.45±0.6570	32.53±1.434	32.33±1.571	
1.6	25.53±0.5642	29.11±1.194	26.87±1.131	28.42±0.9035
1.8		12.45±1.631	19.01±1.309	21.85±1.429
2.0		3.454±0.6565	11.89±1.759	14.17±1.464

Table 4.7: Estimated energy release for all cases, in kilojoules.

λ	No PSC	PSC SOI	PSC EOI ×1	PSC EOI ×2
1.2	4.481±0.07472	4.566±0.07748	4.510±0.07608	
1.4	3.405±0.06349	3.638±0.1600	3.615±0.1754	
1.6	2.631±0.06127	3.255±0.1332	3.004±0.1264	3.178±0.1012
1.8		1.392±0.1825	2.125±0.1463	2.443±0.1603
2.0		0.3862±0.0733	1.329±0.1960	1.584±0.1635

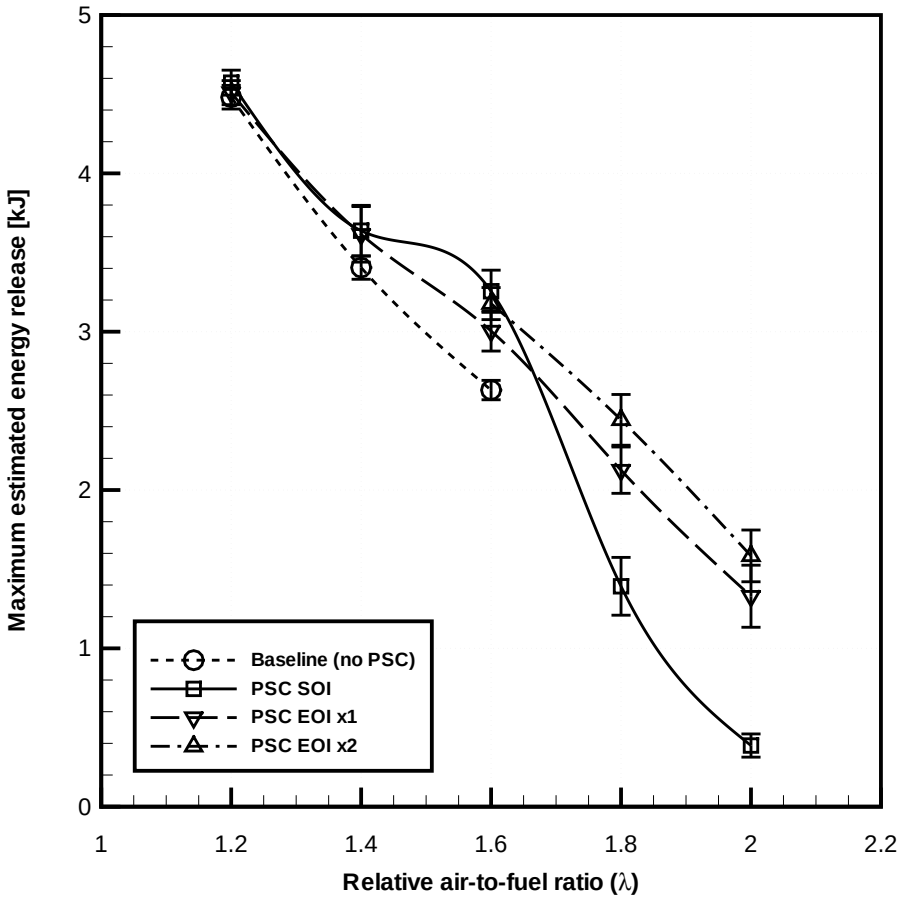

Figure 4.4: Estimated heat release for all cases.

Table 4.8: Normalized combustion pressure rise for all cases.

λ	**No PSC**	**PSC SOI**	**PSC EOI ×1**	**PSC EOI ×2**
1.2	6.007±0.03146	5.785±0.1033	5.800±0.1030	
1.4	4.635±0.03938	4.644±0.2021	4.665±0.2245	
1.6	3.536±0.07777	4.155±0.1687	3.833±0.1608	4.076±0.1313
1.8		1.773±0.2326	2.700±0.1856	3.134±0.2075
2.0		0.4934±0.09351	1.707±0.2507	2.029±0.2086

Table 4.9: Normalized estimated energy release for all cases.

λ	**No PSC**	**PSC SOI**	**PSC EOI ×1**	**PSC EOI ×2**
1.2	0.6259±0.01044	0.6377±0.01082	0.6299±0.01063	
1.4	0.5484±0.01023	0.5859±0.02576	0.5822±0.02825	
1.6	0.4801±0.01118	0.5940±0.02429	0.5481±0.02306	0.5797±0.01846
1.8		0.2837±0.03721	0.4333±0.02983	0.4980±0.03267
2.0		0.08698±0.01650	0.2994±0.04415	0.3568±0.03681

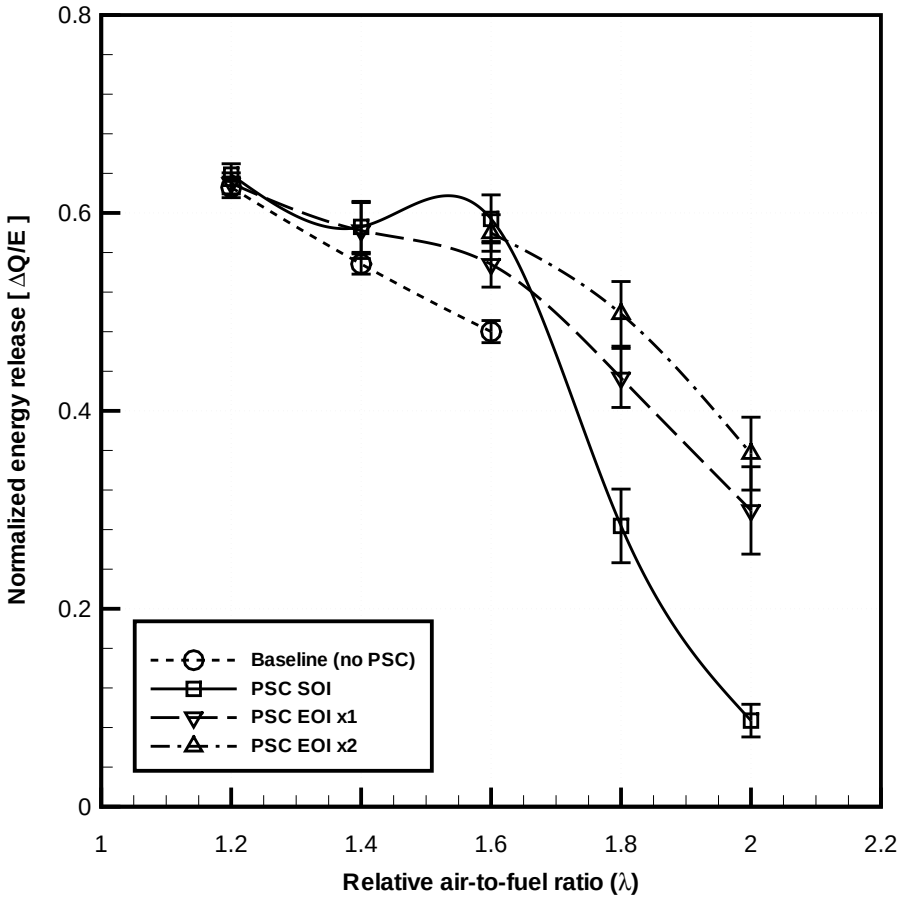

Figure 4.5: Normalized estimated heat release for all cases.

4.2.3 Pressure history and energy release rate

The discussion of the individual behavior in pressure history and energy release rate is divided between moderately lean (λ = 1.2 and 1.4), and ultra-lean (λ = 1.6 to 2.0) cases. Each section provides additional insight in the role of the PSC injection in stabilizing combustion, even in cases where no self-sustaining flame front could be obtained with the homogeneous mixture alone.

a. **Moderately lean operation (λ = 1.2 and 1.4)**

Figures 4.6 to 4.10 show the average pressure histories for the PSC ignition scenarios at each air-to-fuel ratio. The corresponding energy release rates are presented in Figures 4.11 to 4.20. At λ = 1.2, the pressure traces (Figure 4.6) showed no appreciable difference. A similar trend could be observed for the pressure history for the case of λ = 1.4, as presented in Figure 4.7, which also showed no appreciable difference in peak pressure values. Based on the energy release rates, as evidenced in Figures 4.11 (for λ = 1.2), the PSC injection increased the energy release rate early from the spark onset, as the injection provided a richer mixture, and flame kernel could be developed at a higher temperature. The higher global energy release rate observed in the homogeneous case was likely a result of a slower initial consumption of the fuel.

Further, the combustion was initiated much faster for the SOI cases than the EOI cases. For the SOI cases, the flame kernel was formed before its interaction with the PSC jet. Since the bulk mixture was still reasonably rich, the flame kernel grew quickly, and the rich PSC jet was able to be ignited upon contact with the flame surface, and the jet momentum carried the flame front further. On the other hand, the EOI spark ignition took place when the PSC injection was about to complete. The end-injection had a lower momentum, and therefore did not promote fuel consumption rate substantially. Nevertheless, the early increase in energy release for the SOI case quickly decreased about 1 ms after the spark onset, as shown in Figure 4.12. Since the

energy release (Tables 4.7 and 4.9) were about the same for all three cases at $\lambda = 1.2$, the PSC injection did not have a significant influence on the combustion energy output.

A similar but more pronounced trend could also be observed for $\lambda = 1.4$. Since the peak estimated energy release (again, see Tables 4.7 and 4.9) did not show substantial difference from one case to another, the use of PSC resulted in no significant improvement in the energy output. This observation was verified by the pressure trace in Figure 4.7. However, as evidenced in Figure 4.13, the energy release rate for the homogeneous case lagged behind both PSC cases, and did not reach their peak values until about 140 ms after the spark signal. While the heat release rate for the PSC cases peaked at about 70 ms.

A closeup of the initial stages of energy release (Figure 4.14) showed that a boost in energy release rate could be achieved with the SOI spark timing at the beginning. However, the quiescent flame kernel growth was much slower at $\lambda = 1.4$ than $\lambda = 1.2$, so the improvement introduced by the flame kernel's interaction with the PSC jet was also diminished. The EOI ignition at $\lambda = 1.4$ was able to attain a reasonably fast combustion, and the energy release rate surpassed the SOI case at about 21 ms.

***b.* Ultra-lean operation (λ = 1.6 to 2.0)**

Significant deviations in pressure history between homogeneous and PSC ignition could be observed in Figure 4.8 for $\lambda = 1.6$. The laminar flame speed in the bulk mixture was much reduced in this case, which yielded a much slower pressure rise and lower peak pressure. The corresponding heat release rate, presented in Figure 4.15 also showed a low level plateau beyond the peak energy release rate, which indicated a substantial loss in combustion energy due to heat transfer to the combustion chamber surface. Further, the initial cases for homogeneous mixtures for $\lambda = 1.8$ and $\lambda = 2.0$ indicated no evidence of flame kernel formation from spark

ignition. For this reason, these cases were not pursued.

Returning to $\lambda = 1.6$, the PSC cases showed an appreciable improvement in combustion duration, from 566 ms (for the homogeneous case) to approximately 300 ms (see Table 4.4). The presence of the PSC jet allowed the initial kernel to grow at a faster rate due to an increase in flame speed resulting from the richer mixture and localized turbulence. As mentioned in Section 4.1.3, an additional PSC injection method was introduced from $\lambda = 1.6$ onwards. A second PSC injection was introduced with the EOI spark timing.

The effect of the second PSC injection became apparent by inspecting the corresponding energy release rates in Figures 4.15 and 4.16. For the homogeneous case, the rate of fuel consumption depended on the flame kernel surface area. For the purpose of illustration, the asymptotic flame kernel growth behavior can be considered, where the rate of energy release is related to the laminar flame speed of the mixture:

$$\begin{aligned} \frac{dE_k}{dt} &= \frac{d}{dt}\left(\rho_b V_k\right) = \rho_u A_k S_L \\ \frac{dr_k}{dt} &= \left(\frac{\rho_u}{\rho_b}\right) S_L. \end{aligned} \tag{4.4}$$

Upon integration, it can be shown that, $m_k \sim V_k \sim t^3$ for early combustion. A similar observation could be made for the EOI spark timing. When at the conclusion of the PSC injection, the spark region was populated with a rich mixture at low momentum. A spark-ignited flame kernel at this point would therefore behave as the homogeneous case, except for an increased expansion rate due to a higher flame speed resulting from the rich PSC mixture in the vicinity of the spark ignition site. With the SOI spark timing, the PSC jet allowed additional fuel to be ignited. This resulted in a rapid increase in initial energy release rate, but the rate decreased as the PSC injection subsided.

The dual injection technique combined the boost in energy release observed with the SOI spark timing, and the ignition stability offered with the EOI (single injection) spark timing. With the first injection, the flame kernel could be developed in a richer mixture, as opposed to a homogeneous mixture, which accelerated the maturation of the flame kernel. The second injection, like the SOI spark timing, helped propel the flame kernel into the bulk fluid. This was evidenced by a corresponding near step-wise increase in initial energy release rate (Figure 4.16). A sudden deceleration in the burning rate in all three PSC cases, however, indicated a transition from consumption of fuel from the PSC jet to the bulk mixture, which proceeded at a substantially slower rate in leaner mixtures.

The influence of the PSC injection could be readily observed for cases where the homogeneous bulk mixture alone could not support a self-sustaining flame front, that is, $\lambda = 1.8$ and 2.0. The pressure traces in Figures 4.9 and 4.10 showed that the SOI ignition strategy, that yielded satisfactory results in the richer cases, resulted in a substantially diminished pressure rise. At this point, the mixture was beyond its flammability limit, and a spark event was not expected to produce a self-sustaining flame kernel in the homogeneous mixture, evidenced by the time required for the pressure to reak its peak value, compared to the two EOI ignition cases. The EOI dual injection spark timing gave rise to a higher peak pressure than the single injection case for both bulk air-to-fuel ratios.

By inspecting the corresponding energy release rates (Figures 4.17 and 4.18 for $\lambda = 1.8$, and Figures 4.19 and 4.20 for $\lambda = 2.0$), each PSC injection after the spark timing resulted in a rapid increase in energy release rate. This was followed by a rapid decrease, followed by a recovery. The increase introduced by the PSC injection was indicative of a preferential combustion along the PSC jet. Further, the momentum of the PSC injection also carried the flame front further into the bulk mixture, increasing the contact area between the flame and the bulk (unburnt) mixture. When the fuel of the PSC jet was consumed, turbulent mixing remained the only

interaction mechanism between the flame and the ultra-lean bulk mixture. This resulted in a sudden decrease and eventual recovery in energy release rate.

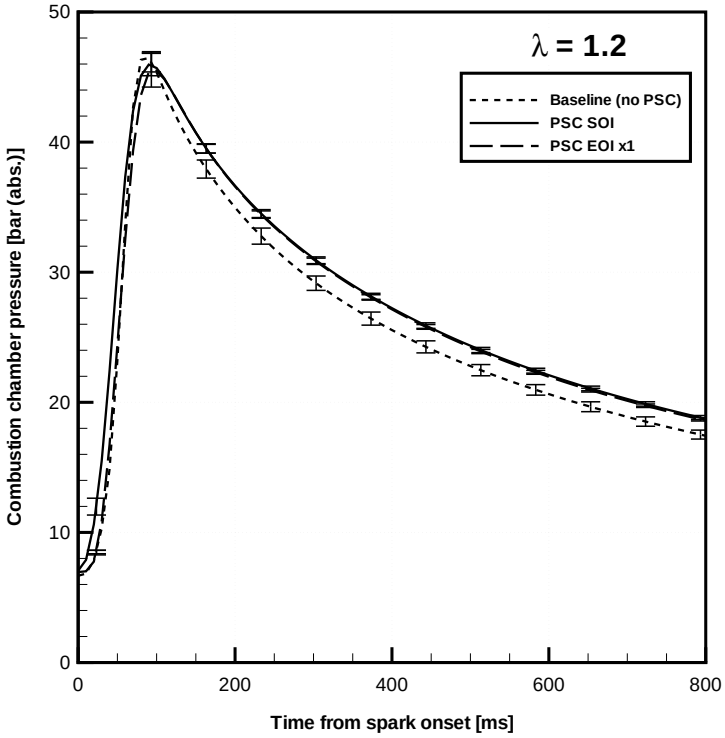

Figure 4.6: Combustion pressure history for all cases at $\lambda = 1.2$.

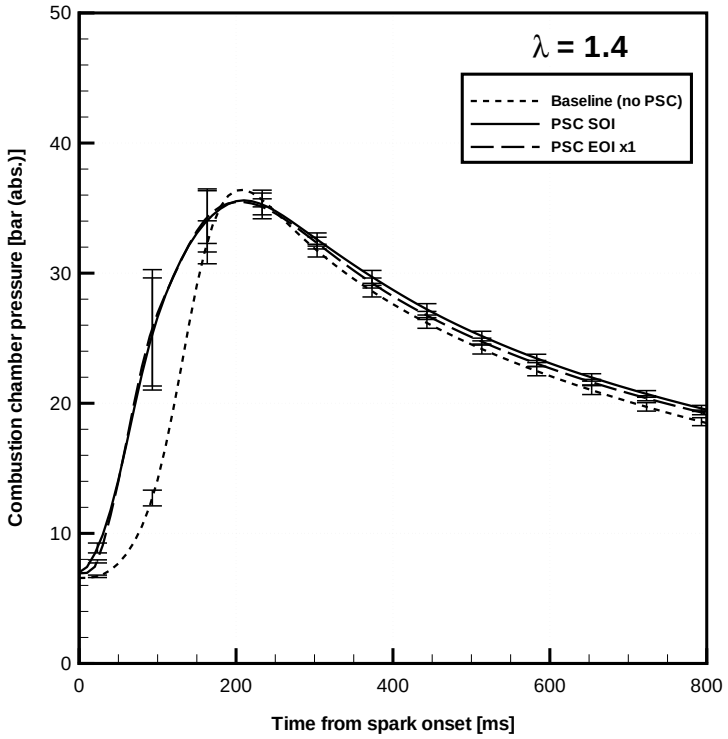

Figure 4.7: Combustion pressure history for all cases at $\lambda = 1.4$.

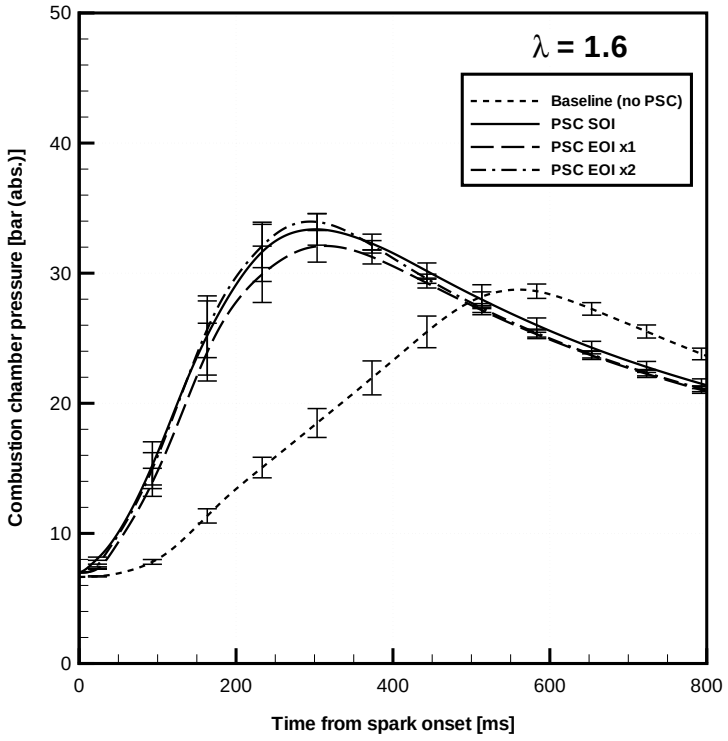

Figure 4.8: Combustion pressure history for all cases at $\lambda = 1.6$.

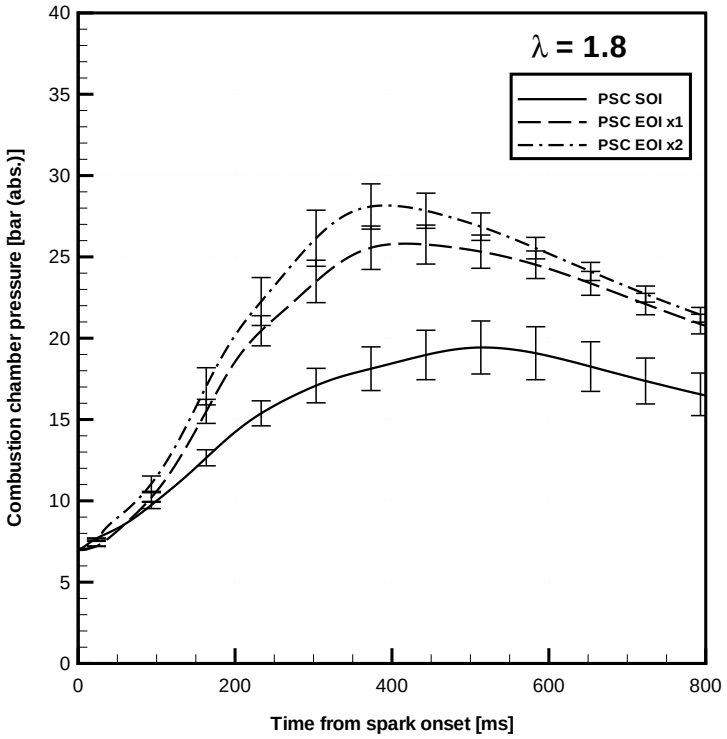

Figure 4.9: Combustion pressure history for all cases at $\lambda = 1.8$.

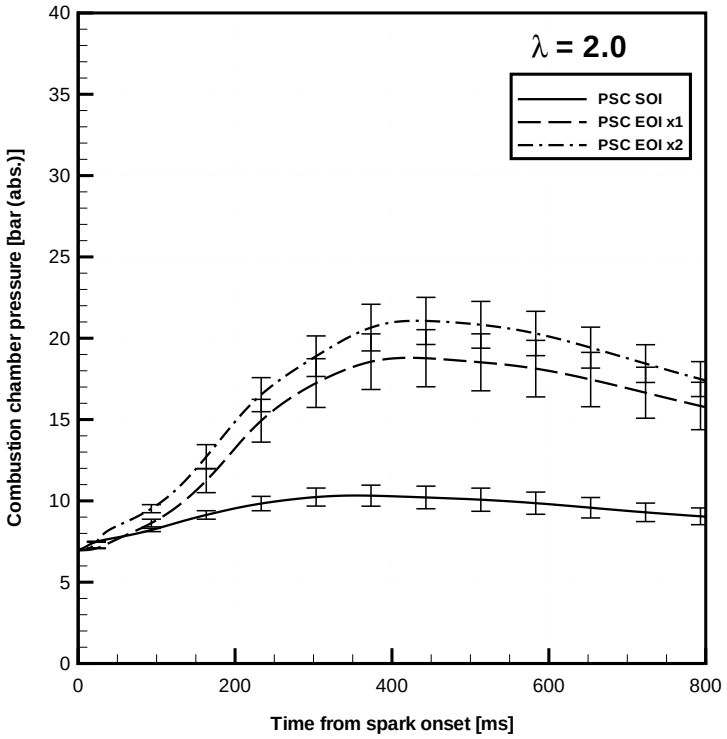

Figure 4.10: Combustion pressure history for all cases at $\lambda = 2.0$.

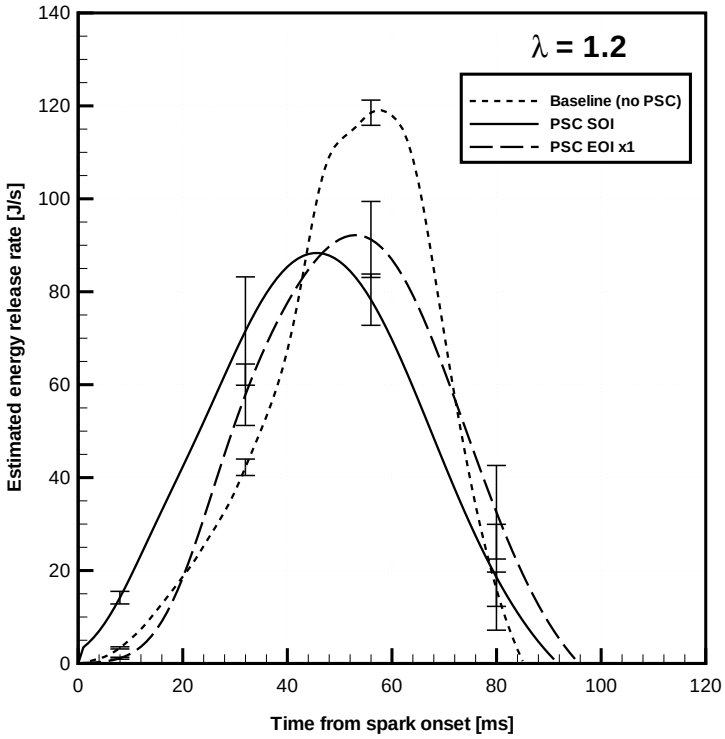

Figure 4.11: Estimated energy release rate for all cases at $\lambda = 1.2$.

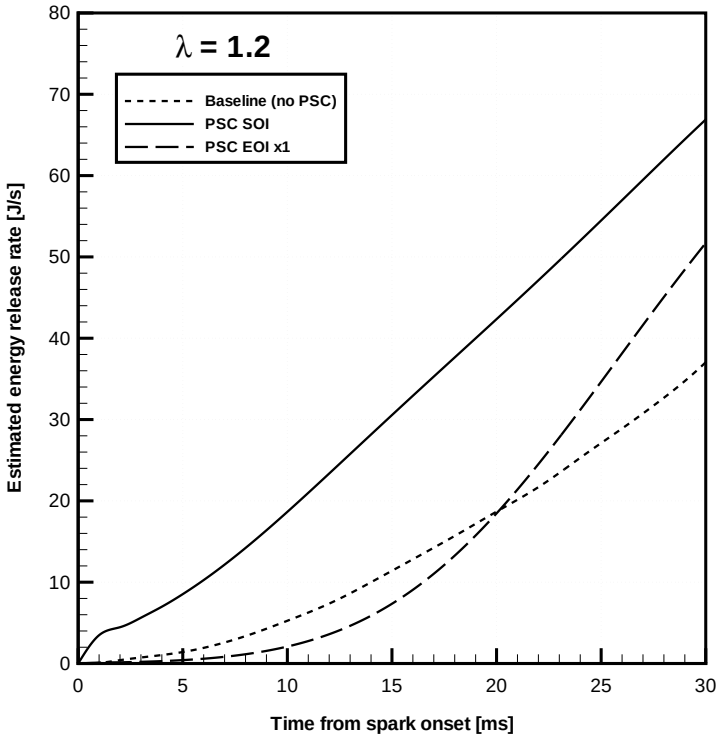

Figure 4.12: Initial estimated energy release rate for all cases at $\lambda = 1.2$.

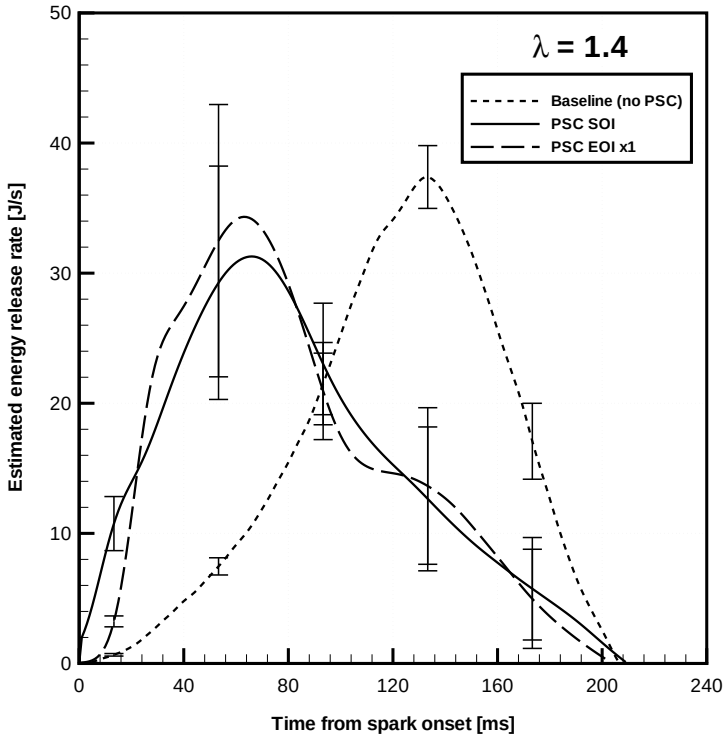

Figure 4.13: Estimated energy release rate for all cases at $\lambda = 1.4$.

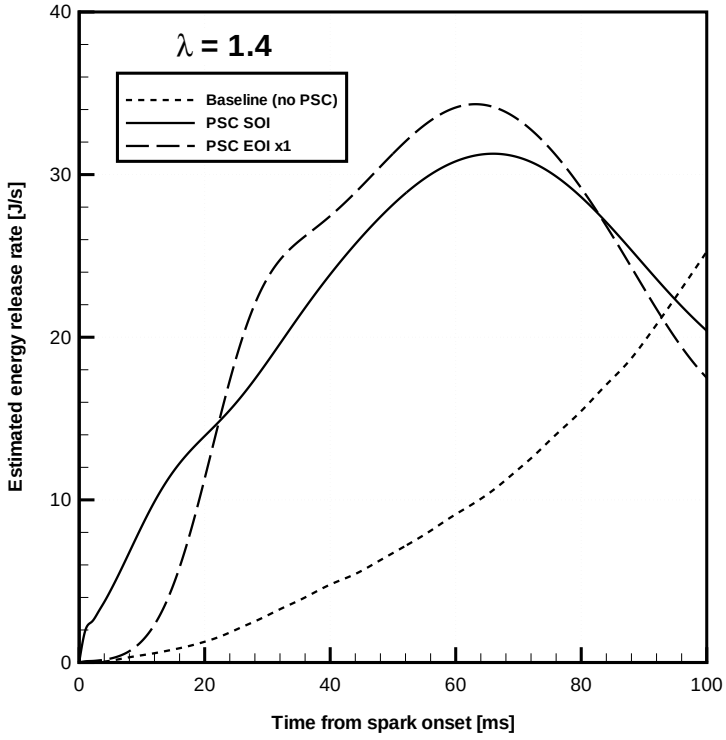

Figure 4.14: Initial estimated energy release rate for all cases at $\lambda = 1.4$.

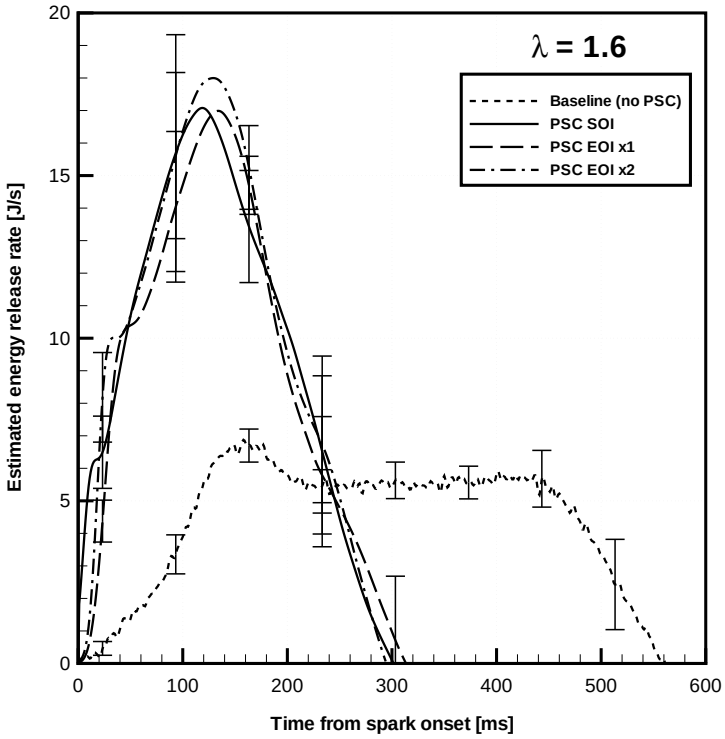

Figure 4.15: Estimated energy release rate for all cases at $\lambda = 1.6$.

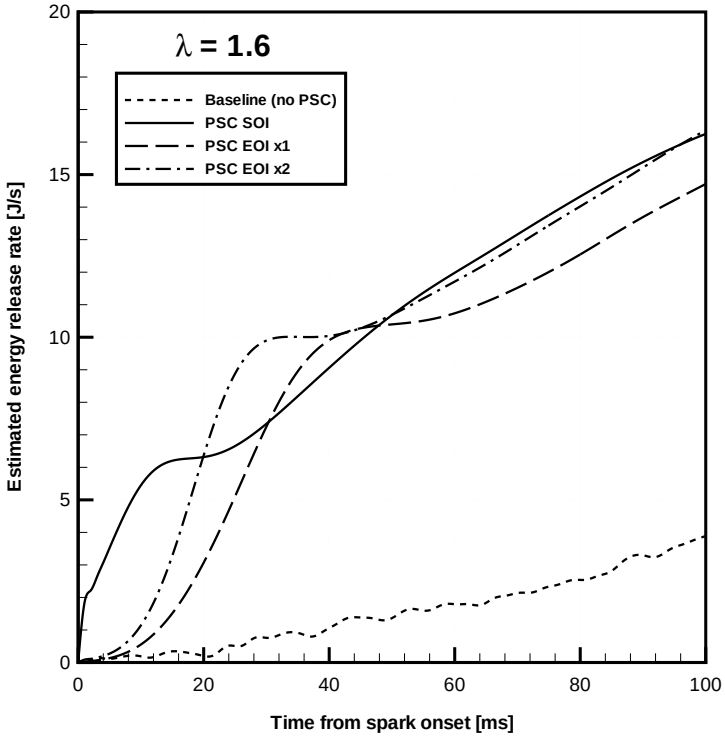

Figure 4.16: Initial estimated energy release rate for all cases at $\lambda = 1.6$.

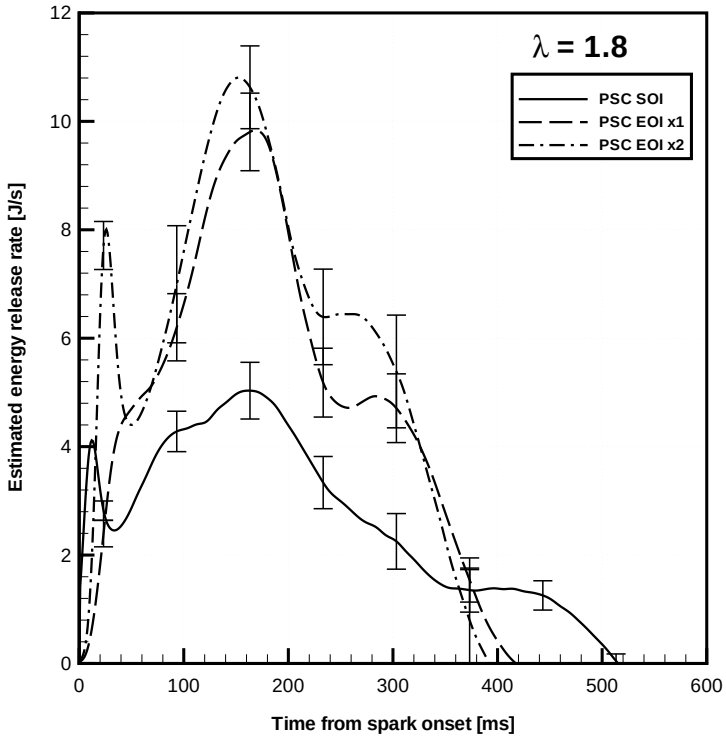

Figure 4.17: Estimated energy release rate for all cases at $\lambda = 1.8$.

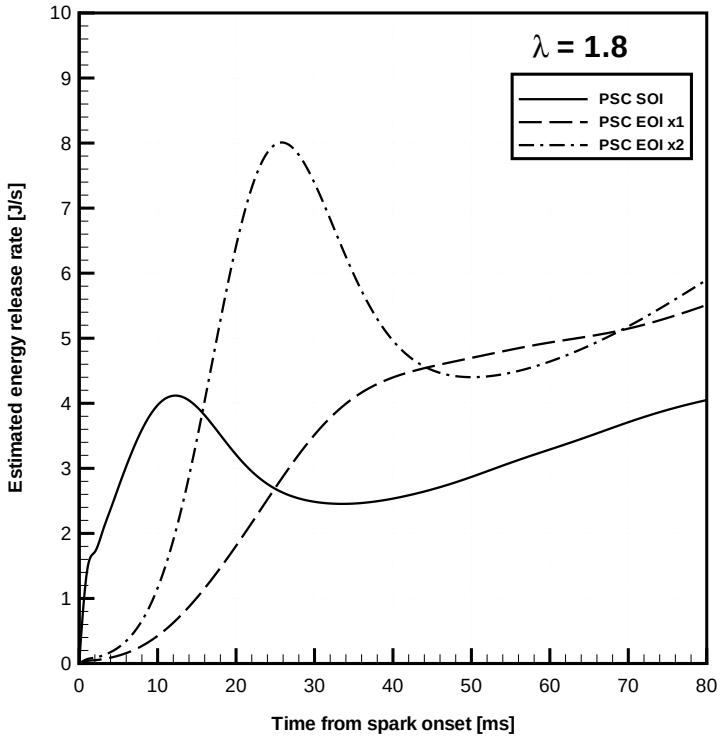

Figure 4.18: Initial estimated energy release rate for all cases at $\lambda = 1.8$.

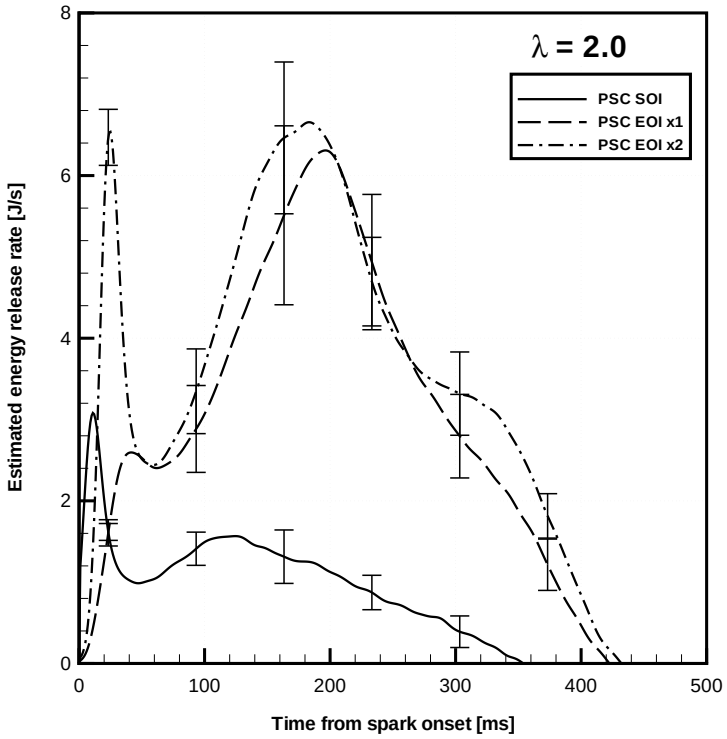

Figure 4.19: Estimated energy release rate for all cases at $\lambda = 2.0$.

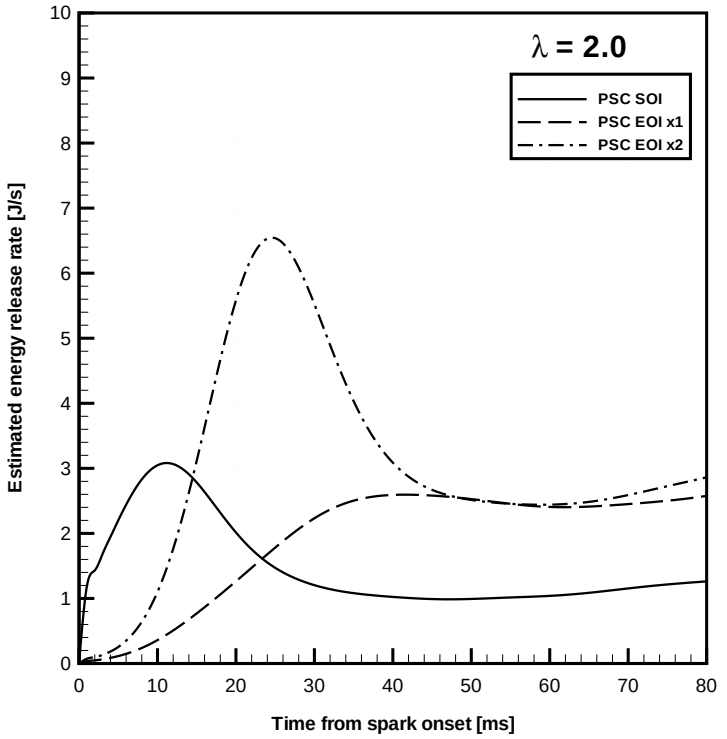

Figure 4.20: Initial estimated energy release rate for all cases at $\lambda = 2.0$.

4.3 Flame development and propagation

While the overall combustion behavior in the combustion chamber could be easily assessed with pressure history and energy release behaviors, additional information such as flame propagation and kernel development required direct visualization. Such data were collected using high-speed Schlieren motion photography. The discussion will begin by inspecting the baseline, homogeneous charge cases, which featured the classical laminar spherical flames. This is followed by a examining the PSC cases at each air-to-fuel ratio. The images provide some insight to explain the overall combustion behaviors encountered under different PSC injection and ignition strategies.

4.3.1 Baseline cases

Figure 4.21 shows the flame evolution for the baseline cases at all air-to-fuel ratios considered. As the mixture was quiescent, the flame front was expected to expand in a roughly spherical manner. While the flame kernel was anchored to the spark electrodes early in the spark onset as a result of the flame holder effect, buoyancy-driven displacement of the flame kernel became apparent later on in the flame development. Heat loss to the chamber wall and electrodes also resulted in deformation of the kernel from its spherical shape. Meanwhile, the transition to a cellular flame can be observed for $\lambda = 1.2$ at 40 ms. Cellularity originates from hydrodynamic and diffusional-thermal instabilities, as pointed out by Jomaas et al. (2007).

The speed of flame kernel expansion could be modeled, and several interesting points could be identified and subsequently expanded to include effects of turbulence. Recall Equation (4.4):

$$\frac{dr_k}{dt} = \left(\frac{\rho_u}{\rho_b}\right) S_L.$$

Note that dr_k/dt is also the speed of flame propagation, and it denoted as S_b for simplicity. The stretched laminar flame speed (S_L) can be expressed using the stretch factor, I_0, such that Equation (4.4) can be normalized:

$$\frac{dr_k}{dt} = \left(\frac{\rho_u}{\rho_b}\right) I_0 S_L^0$$
$$\frac{S_b}{S_L^0} = \left(\frac{\rho_u}{\rho_b}\right) I_0,$$

while the flame stretch factor can derived from the Markstein length (L_b), a measure of flame stretch:

$$I_0 = \frac{S_L}{S_L^0} = 1 - \frac{\kappa L_b}{S_L^0},$$

where κ is the normalized stretch rate for the flame surface. Introducing δ_L, the laminar flame thickness, yields:

$$I_0 = 1 - \underbrace{\left(\frac{\kappa \delta_L}{S_L^0}\right)}_{\text{Ka}} \underbrace{\left(\frac{L_b}{\delta_L}\right)}_{\text{Ma}}. \tag{4.5}$$

So the flame stretch can be expressed in terms of the normalized stretch rate (Karlovitz number, Ka) and the normalized thermally-induced stretch length (Markstein number, Ma). The Markstein number can be defined as follows (Chung and Law, 1988; Law et al., 1986):

$$\text{Ma} = \frac{1}{\text{Le}} + \left(\frac{\text{Le}-1}{\text{Le}}\right)\left(\frac{T_A}{2T_{\text{ad}}}\right), \tag{4.6}$$

where Le is the Lewis number, the ratio between heat and mass diffusivities, and T_A is the activation temperature. So Equation (4.4) becomes:

$$\frac{S_b}{S_L^0} = \left(\frac{\rho_u}{\rho_b}\right)\left\{1 - \text{Ka}\left[\frac{1}{\text{Le}} + \left(\frac{\text{Le}-1}{\text{Le}}\right)\left(\frac{T_A}{2T_{\text{ad}}}\right)\right]\right\}. \tag{4.7}$$

The hydrodynamic instability is a result of disparity in burnt and unburnt mixture densities (Landau, 1944), and the diffusional-thermal instability originates from a disparity in mass and

heat diffusion rates, represented by the Lewis number (Law, 2006). Since, from Equation (4.6), Le < 1 implies Ma < 0. This leads to an *increase* in burning speed with stretch. For lean natural gas flames, however, the Lewis number is effectively constant, and below unity (Wang et al., 2010). So it is expected that the stretched laminar flame speed, and subsequently the burning speed would be reduced from the unstretched level.

4.3.2 PSC cases

The introduction of the PSC jet introduced two additional modifiers to the flame propagation from the baseline case. Firstly, there is an increase in local air-to-fuel ratio due to the introduction of the fuel jet. Secondly, the flame kernel, and later the flame front, also undergo deformation due to local bulk movement and turbulent fluctuation induced by the injection. The combination of the two factors determined the overall combustion behavior. While it was clear, from Section 4.2, that the presence of PSC alone was sufficient to promote combustion in cases that were typically beyond the lean flammability limit of the homogeneous mixture, the degree of promotion could be inferred from analysis based on the Schlieren images, presented in Figures 4.22 to 4.25.

The enabling mechanisms for the SOI, EOI, and EOI×2 ignition methods were expected to be different. With the SOI spark timing, the interaction took place between an already developing flame front the head of the PSC jet, which could be idealized as a traveling spheroid composed of a mixture of jet and entrained gases (Turner, 1963), and the flame was carried along the jet as the flame developed, effectively increasing the flame surface area. The PSC jet tip reached the spark electrodes at about 0.5 ms after the spark onset for all SOI cases, as evidenced by the SOI Schlieren images in Figures 4.22 to 4.25.

In the EOI spark timing, the initiation of the flame kernel occurred in a rich and turbulent mixture. While it was expected that the flame kernel development be more stable (Johansson et al., 1995), the effects of flame displacement was also diminished compared to the SOI cases, due to the lack of jet momentum, as seen on the EOI cases in Figures 4.22 to 4.25. This was remedied with a second PSC injection, presented in the EOI×2 cases in Figures 4.23 to 4.25, where the flame propagated with the second PSC injection. The enhancement obtained from each mode of PSC injection and ignition method has been discussed in Section 4.2.3.

Referring to Figures 4.22 to 4.25 again, the development of the flame kernels could be readily identified from the Schlieren images for up to 1 ms after the spark onset. They were characterized by a near spherical shape, and anchored at the spark electrodes through the flame-holder effect. For all air-to-fuel ratios, a larger flame kernel could be observed for the SOI case than the two EOI cases at 1 ms after the spark signal. This was due to both the simultaneous expansion of the spark plasma and the PSC jet head, which allowed for a greater interaction surface.

Despite the presence of a rich, turbulent flow field near the ignition region, the EOI timing was not able to develop a the flame kernel as rapidly as the SOI cases. For the moderately lean cases, i.e., λ = 1.2 and 1.4 (Figure 4.22), the Schlieren images clearly showed a slightly slower flame front expansion in the corresponding EOI cases than SOI cases. The disparity in flame propagation continued to widen as λ increased. Therefore the presence of bulk movement, as demonstrated from the SOI cases, was of paramount importance in promoting flame propagation.

The EOI×2 timing compensated for the shortcomings in the single injection EOI timing. While ignition was still preferred to take place when the local air-to-fuel ratios was favorable, additional bulk flow would bring the flame kernel further into the bulk mixture. The dual

injection method was introduced at λ=1.6 (see Figure 4.23). While the double injection did not show significant improvement at λ = 1.6, compared to the corresponding SOI cases, the presence of the second injection helped propel the flame kernel further into the combustion chamber.

At λ = 1.8 and 2.0, the dual injection EOI cases demonstrated an improvement over the SOI cases in terms of early combustion. Under the SOI cases, even though there was still a plasma, the fuel-lean homogeneous mixture was not able to sustain a flame kernel prior to the direct interaction with the PSC jet. As the laminar flame speed was also substantially lower beyond the ultra-lean levels, hydrodynamic mixing became the primary burning mechanism. The dual injection EOI strategy allowed the flame to propagate with higher local turbulence, thus increasing the interaction with the bulk mixture.

The PSC cases, however, showed a critical aspect which facilitated combustion. Due to the presence of the jet, the ignited flame kernel showed a preference to propagate along the PSC jet, where the mixture is richer. Flame propagation along the jet, increased contact area with the bulk mixture, which also became ignited. This phenomenon became more pronounced in the leaner cases, where the burning rate in the bulk mixture was substantially slower. The tendency to consume the PSC jet fuel, under these cases, could readily be seen. Induced by bulk movement and additional turbulence, the flame was brought to the remaining bulk fluid.

4.4 The phases of PSC-enhanced combustion

The PSC strategy enhances spark ignition in two ways. First, the locally rich mixture introduced by the PSC injection alters the chemical kinetics at the time of the spark, and second, turbulence resulting from the injection also promotes an earlier transition to a fully turbulent flame front. However, from the results presented in Sections 4.2.3 and 4.3, the manner in which these two

factors contribute to the stability and enhancement of the ignition and combustion under PSC can be effectively regarded as a three-phase process:

- Maturation of the flame kernel,
- Propagation of the PSC flame front, *and*
- Penetration of the PSC flame into the bulk mixture.

Maturation. It has been generally accepted that a stable flame kernel is the key to a stable combustion (Aleiferis et al., 2004; Deshaies and Joulin, 1984; Johansson et al., 1995). The presence of a rich, local mixture appeared to be one of the most important factors in influencing the outcome of an ignition event (Andreassi et al., 2003b; Herweg and Maly, 1992). The ability of the PSC jet to foster a stable flame kernel even beyond the bulk mixture flammability, was the first and direct benefit of adopting such strategy, is demonstrated from the Schlieren images.

Propagation. On the other hand, the current experimental results show that flame kernel stabilization is only requisite to a stable combustion. To borrow terminology from electronics, a "conductive" path must be established between the flame kernel and the bulk mixture in order to promote combustion into the bulk mixture. The Schlieren images indicate the tendency for the PSC flame front to preferentially ignite along the PSC jet, particularly in the leaner cases, due to a favorable local air-to-fuel ratio along the jet. The presence of the PSC jet facilitates the propagation of the flame kernel into the bulk mixture.

Penetration. The penetration phase is characterized by the ignition of the bulk mixture from the propagating PSC flame. In moderately lean mixtures, the bulk mixture flame speed is still sufficiently high, so the penetration proceeds while the PSC flame is still propagating. As the bulk mixture is further leaned out, the low bulk mixture flame speed necessitates enhanced penetration through hydrodynamic mixing. In the context of the experiments, it is accom-

plished through a strong bulk flow. The results of the SOI and EOI×2 cases illustrate this technique.

4.5 Relevance to engine conditions

The bulk of the experiments have been performed in a quiescent environment, with the PSC jet being the only source of flow movement. The applicability of the current results under engine conditions is therefore of interest. Fundamentally, the two major deviations are the presence of charge movement and the continually changing pressure and temperature of the bulk mixture resulting from compression. Though geometry also plays an important role, geometric factors of the combustion chamber contribute directly to the charge movement, and geometric factors of the spark region can be compensated through design of PSC injection methods.

The presence of bulk movement, as indicated from the experimental results, allows the flame kernel to be advected into the bulk mixture. Further, reignition of the mixture is also another possibility at sufficiently high mean velocities Maly (1984), effectively increasing the size of the flame kernel. On the other hand, turbulent fluctuation also provides a stronger flame kernel growth and propagation. While flame wrinkling does, indeed, increase the flame surface area, the associated increase in heat loss also leads to a reduction in flame temperature, which might result in flame quenching. Correlations have been proposed by Abdel-Gayed and Bradley (1985) to relate local turbulence with the quenching limit:

$$\frac{u'}{S_L^0} \geq \begin{cases} 0.71\left(\dfrac{u'L_e}{\nu}\right), & \dfrac{u'L_e}{\nu} < 300 \\ \\ 3.1\left(\dfrac{u'L_e}{\nu \mathrm{Le}^2}\right), & \dfrac{u'L_e}{\nu} > 300 \end{cases} \tag{4.8}$$

In addition, for $Le \sim 1$ and negligible curvature effects, Chan et al. (2011) proposed a second quenching limit based on the ignition model of Herweg and Maly (1992), at which point the flame stretch was deemed too severe to sustain a flame front:

$$\left(\frac{\delta_L}{15L_e}\right)^{1/2}\left(\frac{u'}{S_L}\right)^{3/2} \geq 1. \tag{4.9}$$

Both Equations 4.8 and 4.9 contain a normalized term u'/S_L, inferring the increase in sensitivity of the quenching limit with decreasing flame speed. The introduction of a richer mixture would remedy the problem. So, while the SOI cases appear to sustain a stable flame kernel, this PSC ignition strategy would not be practical for lean-burn engines due to sensitivity of the initially ignited (bulk) mixture to local turbulence.

The compression of the engine cylinder modifies the bulk mixture flame speed due to changes in its thermodynamic state. In terms of the laminar flame speed, the effects of changing pressure and temperature could be summarized with the empirical relation below (Poinsot and Veynante, 2001):

$$S_L^0 = S_L(p_0, T_0)\left(\frac{p}{p_0}\right)^{\alpha(p)}\left(\frac{T}{T_0}\right)^{\beta(T)}, \tag{4.10}$$

where $\alpha(p), \beta(T)$ are fuel-specific functions, which can be found in Gu et al. (2000), as well as in Metghalchi and Keck (1980). While an increase in pressure results in a reduction in laminar flame speed, the empirical results indicated flame speed actually increases slightly with increasing pressure under turbulence (Lipatnikov and Chomiak, 2002).

From the CVCC experiments, the PSC jet has been shown to provide additional stability in the ignition phase, facilitating the combustion of air-fuel mixtures otherwise too lean to be ignited by conventional automotive ignition systems. Though the combustion takes place in

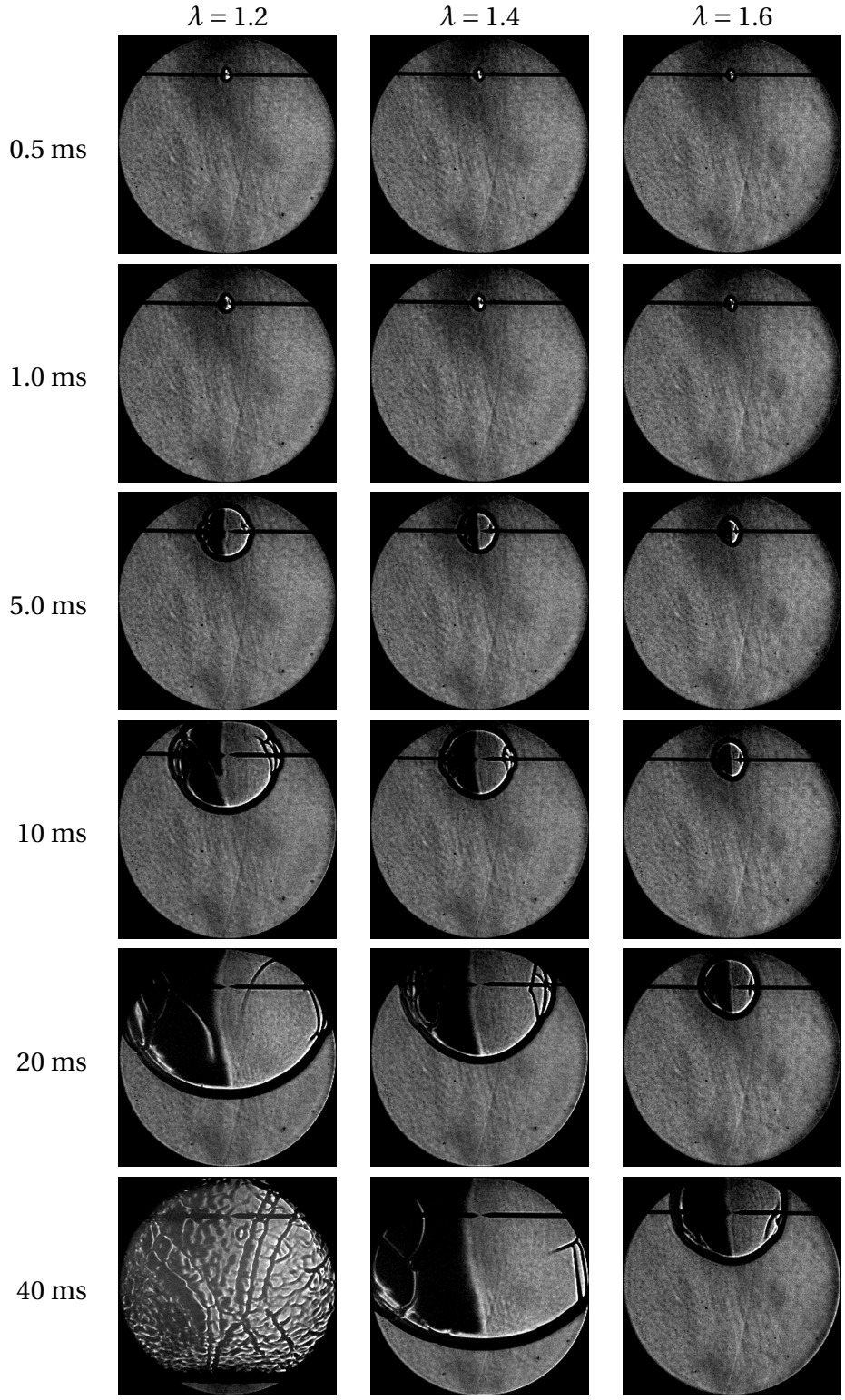

Figure 4.21: Flame kernel evolution for all baseline cases, time elapsed from spark onset.

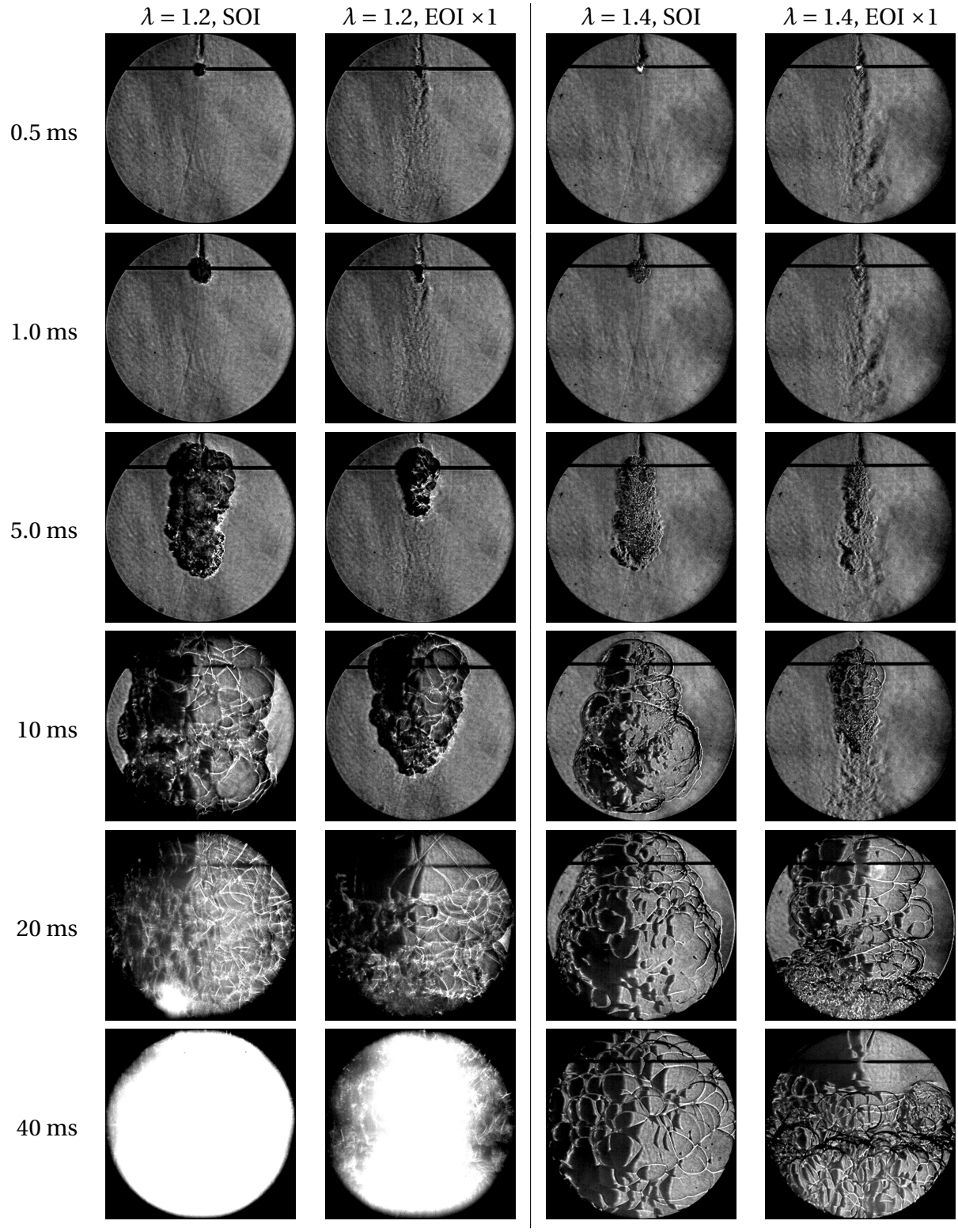

Figure 4.22: Flame front propagation under PSC for λ = 1.2 and 1.4, time elapsed from spark onset.

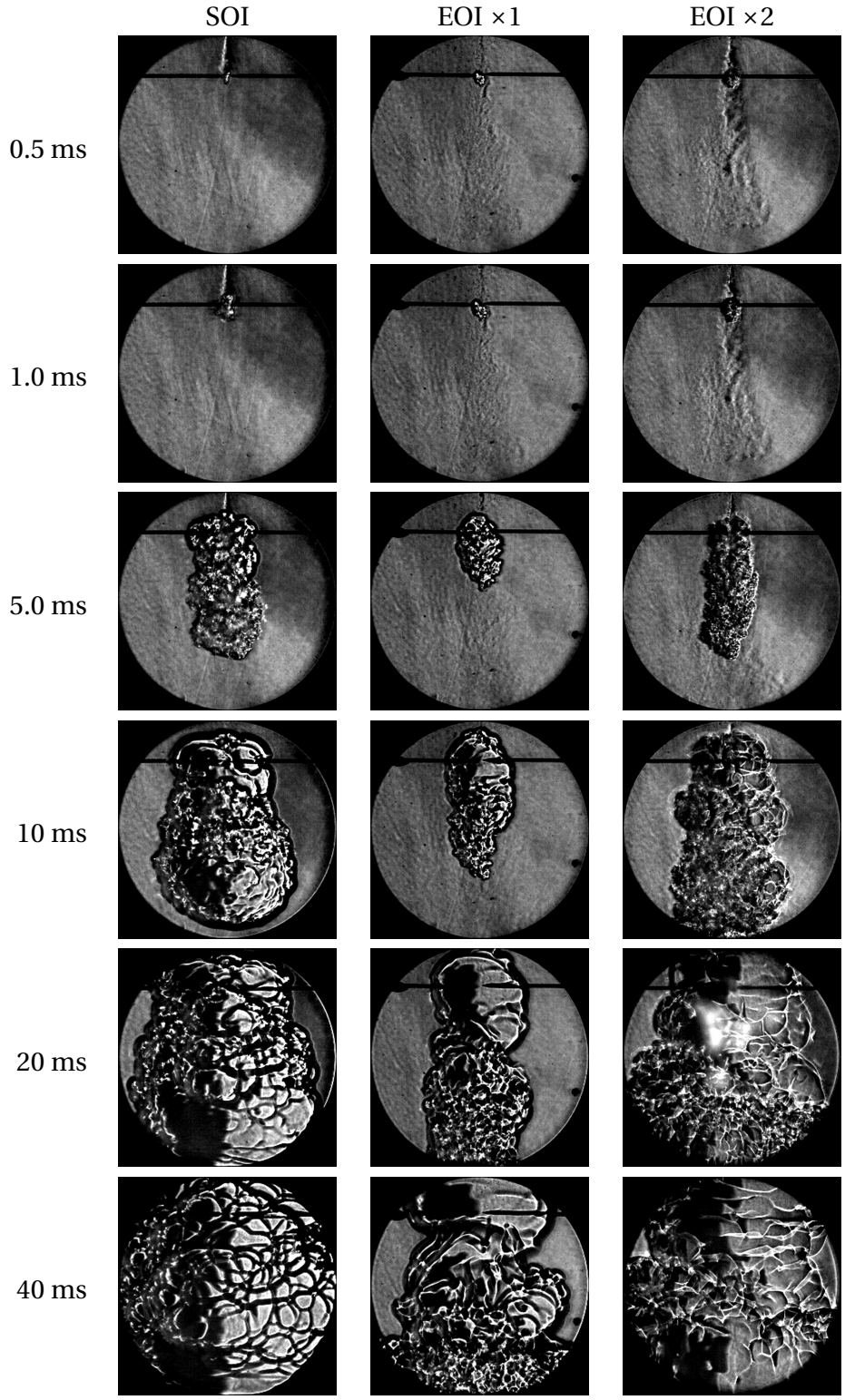

Figure 4.23: Flame front propagation under PSC for $\lambda = 1.6$, time elapsed from spark onset.

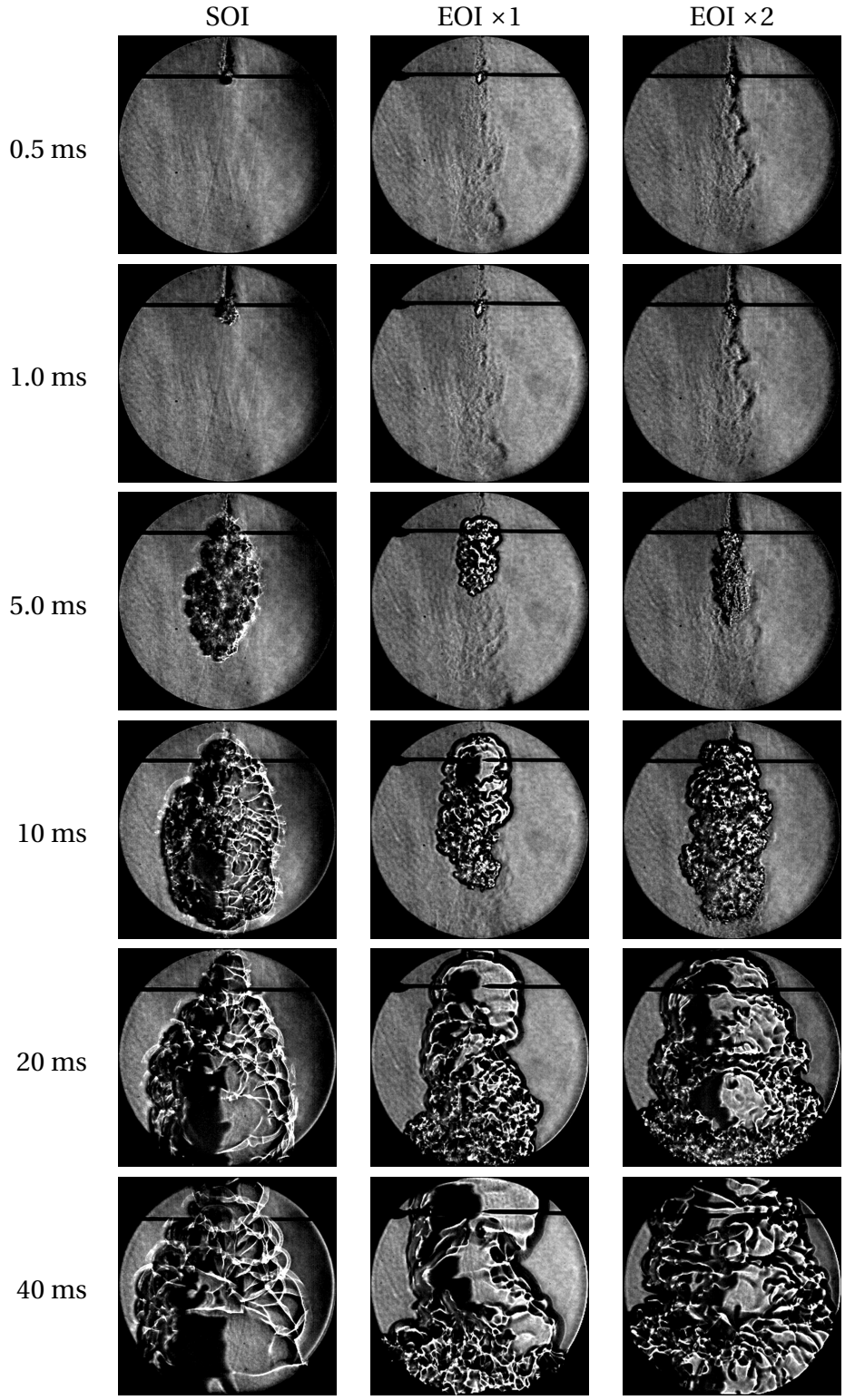

Figure 4.24: Flame front propagation under PSC for $\lambda = 1.8$, time elapsed from spark onset.

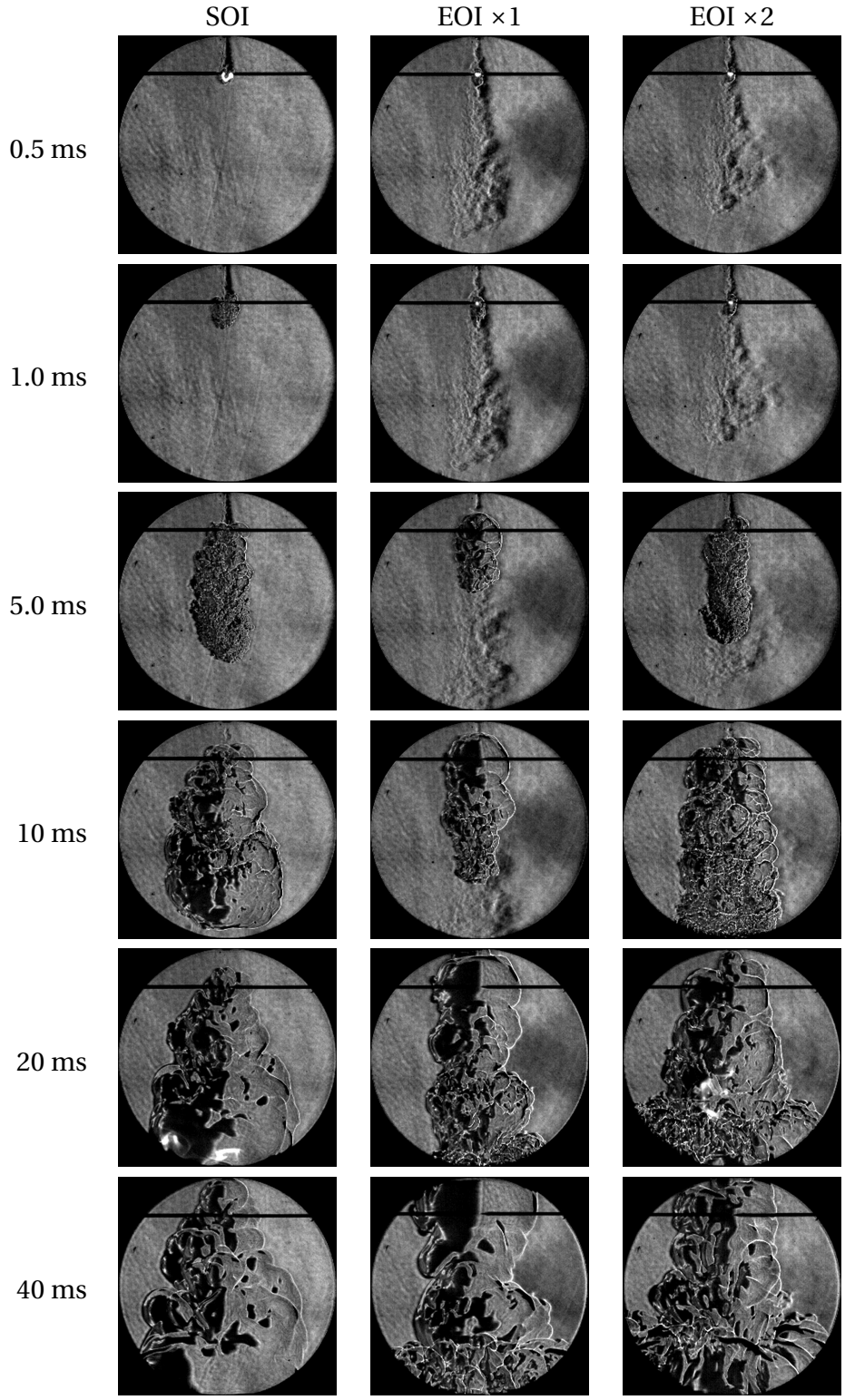

Figure 4.25: Flame front propagation under PSC for $\lambda = 2.0$, time elapsed from spark onset.

a quiescent environment, the CVCC results represent a conservative case, in a sense that the penetration of the PSC flame into the bulk fluid is much slower than it would be observed under engine conditions, where the flow field is expected to be fully turbulent everywhere. In the context of the PSC enabling mechanisms (Section 4.4), provided the flame kernel can reach maturity with the PSC injection, as well as to provide an adequate path for propagation, turbulence in the bulk mixture, such as that encountered under engine conditions, will result in additional enhancement in combustion.

4.6 Summary

Three different PSC ignition strategies (SOI, EOI, and dual injection EOI) were examined in the experimental study from moderately lean to beyond the ultra-lean levels. Baseline experiments, under quiescent, homogeneous conditions were also conducted. First and foremost, the introduction of the PSC injection facilitates consistent and stable combustion behavior, beyond the ultra lean levels. The combustion duration data indicated complete combustion could be achieved up to $\lambda \sim 1.8$ for all PSC cases. Slightly higher peak pressure and energy release could be achieved using the SOI spark timing for the moderately lean bulk mixtures, but additional stability could be attained beyond the ultra lean level with the dual injection EOI method.

The flame evolution under PSC were studied from the Schlieren photographs. Accelerated flame kernel development could be observed for all SOI cases, likely due to a larger interaction surface between the spark plasma and the PSC jet resulting from an increase in local turbulence activity. Premature extinction was expected under this PSC regime, however, when the bulk mixture was under turbulence. This is due to a heightened sensitivity for quenching under ultra-lean conditions. On the other hand, the single injection EOI spark timing, though provided a favorable ignition condition, proved to be slower in advecting the flame kernel. The

dual injection EOI spark timing remedied the issue.

In the ultra lean cases, due to a low bulk mixture flame speed, there was a tendency for the flame kernel to propagate along the PSC jet before igniting the bulk mixture. This observation gave rise to the three enabling mechanisms of the PSC ignition strategy. First was the facilitation of flame kernel maturation, which was requisite for a stable combustion. More importantly, the presence of a rich mixture introduced by the PSC jet allowed the flame kernel to self-propagate into the bulk mixture. This promoted the interaction between the flame kernel and the bulk mixture, allowing the flame to penetrate into the remaining unconsumed fuel. Bulk movement could also be introduced, either through the bulk charge or through a PSC injection. This further accelerated flame penetration, especially for the ultra-lean cases.

Chapter 5

PSC model development

As the enabling mechanisms for PSC have been identified experimentally, the second part of this investigation is to model these phenomena numerically. The commercial code FLUENT was used for the purpose. The discussion on modeling comprises three sections: turbulence, combustion, and spark ignition. The turbulence model must be able to properly predict the evolution of the PSC injection and the bulk flow movement. In addition, the rate of combustion and energy release should be adequately addressed through a physically representative reaction model. Finally, the ignition model should capture the expansion of the flame kernel as the flame front develops following the spark ignition.

5.1 PSC injection

In the idealized geometry (see Figure 3.1), the PSC jet is effectively a transient, compressible, axisymmetric turbulent jet. The jet consists of the injected gas, as well as ambient gas that is entrained into the jet body through turbulent shear. At the inception of the injection, entrianment takes place at the jet tip (Cossali et al., 2001). As the jet continues to develop, the entrainment shifts to the trail behind the jet tip. Turner (1963) first postulated such a jet as a traveling spheroid containing a mixture of jet and ambient gases. The ball is fed by a trailing conical jet, which entrains the ambient gas at the interface between the jet and the surroundings. This idealization, called the "vortex ball" model, is a self-similar, fully-developed representation, and has been used to successfully model entrainment and penetration of the

jet (Ouellette and Hill, 2000; Rubas et al., 1998). The physical description of the jet, as well as its vortex ball representation is presented in Figure 5.1.

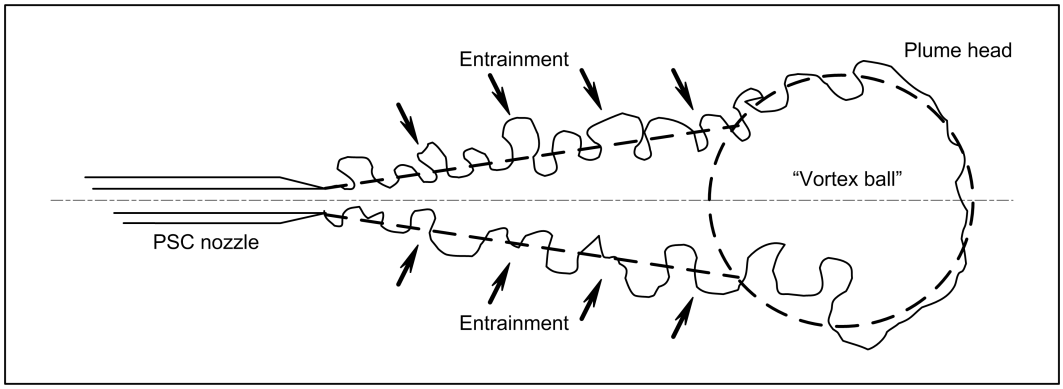

Figure 5.1: A round jet, and its vortex ball representation.

5.1.1 Mass flowrate profile estimation

Typically, existing analyses of the transient jet, such as Hill (1972) and Ouellette and Hill (2000), assumed a constant mass injection rate ($\dot{m}_j$). Since the PSC injection was to be modeled for the full injection period, changes in mass flowrate resulting from the opening and closing of the injector valve could not be ignored. Provided that the data on duration and the injected mass could be obtained, mainly by experimental means, the injection profile could be estimated. To this end, the injection profile was approximated to be elliptical, that is:

$$\frac{\dot{m}_j}{\dot{m}_0} = 1 - \sqrt{1 - \left(1 - \frac{t}{t_{\text{inj}}}\right)^2}, \tag{5.1}$$

with the imposed condition that:

$$\int_{t=0}^{t_{\text{inj}}} \dot{m}_j \, dt = m_{\text{inj}},$$

where $\dot{m}_0$ is the initial mass flowrate, and t_{inj} is the injection duration. For the PSC injection, t_{inj} = 9.9 ms and m_{inj} = 0.354 mg. This resulted in an initial mass flowrate of 0.165 mg/ms, and an average mass flowrate of 0.0354 mg/ms during the injection period. Note that the initial mass flowrate is non-zero, but such is the case of the approximation. Given that the supply voltage

has been increased from 12V to 350V, the rise time is expected to be sufficiently short, in relation to the injection duration, that it can be effectively regarded as instantaneous.

Though it is still only an idealization of actual injection profile, the elliptical profile has two advantages from an analytical point of view. First, the start and end of injection are clearly identified, as the mass flowrates at the endpoints are finite. Second, the function is can be completely defined with only two parameters, namely the injection duration and the total mass flow, both of which can be measured. The simplicity of this model can also be extended to model other injector types, given that the valve lift is not explicitly controlled by the command signal to alter the mass flowrate.

5.2 Fundamental conservation equations

The evolution of the PSC combustion in the CVCC could be resolved numerically as an axisymmetric problem involving turbulence. The instantaneous conserved scalar variable, ϕ, such as velocity component magnitude and energy, can be decomposed into a statistically stationary *mean* part ($\widetilde{\phi}$) and a *fluctuating* part (ϕ'') through a density weighted average (Favre averaging). The conservation equations for mass and momentum are presented here in tensor notation:

$$\left[\frac{\partial}{\partial t}+\frac{\partial \widetilde{u}_j}{\partial x_j}\right]\overline{\rho}=0, \tag{5.2}$$

$$\left[\frac{\partial}{\partial t}+\frac{\partial \widetilde{u}_j}{\partial x_j}\right]\left(\overline{\rho}\widetilde{u}_i\right)=-\frac{\partial \overline{p}}{\partial x_i}-\frac{\partial}{\partial x_j}\left(\overline{\rho}\widetilde{u_i''u_j''}\right). \tag{5.3}$$

The Reynolds stress term in Equation (5.3) can be modeled with the eddy viscosity approach:

$$\overline{\rho}\widetilde{u_i''u_j''}=-\mu_T\left(\frac{\partial \widetilde{u}_i}{\partial x_j}+\frac{\partial \widetilde{u}_j}{\partial x_i}-\frac{2}{3}\frac{\partial \widetilde{u}_k}{\partial x_k}\delta_{ij}\right)+\frac{2}{3}\overline{\rho}\widetilde{k}\delta_{ij}, \tag{5.4}$$

and

$$\mu_T = C_\mu \overline{\rho} \frac{\widetilde{k}^2}{\widetilde{\epsilon}}. \tag{5.5}$$

Meanwhile, the thermodynamic state of the flow is described through the conservation equations for enthalpy and species mass fractions:

$$\left[\frac{\partial}{\partial t} + \frac{\partial \widetilde{u}_j}{\partial x_j}\right](\overline{\rho}\widetilde{h}) = \frac{\partial}{\partial x_j}\left(\frac{\mu_T}{\mathrm{Pr}}\frac{\partial \widetilde{h}}{\partial x_j}\right), \tag{5.6}$$

$$\left[\frac{\partial}{\partial t} + \frac{\partial \widetilde{u}_j}{\partial x_j}\right](\overline{\rho}\widetilde{Y}_i) = \frac{\partial}{\partial x_j}\left(\frac{\mu_T}{\mathrm{Sc}_T}\frac{\partial \widetilde{Y}_i}{\partial x_j}\right) + \overline{\dot{\omega}}_i. \tag{5.7}$$

The reaction rate is modeled in the Arrhenius form:

$$\overline{\dot{\omega}}_i = A\overline{\rho}Y_{\mathrm{i}}\exp\left(-\frac{E_A}{RT}\right). \tag{5.8}$$

Lastly, dedicated transport equations for turbulent kinetic energy and dissipation rate are provided for model closure:

$$\left[\frac{\partial}{\partial t} + \frac{\partial \widetilde{u}_j}{\partial x_j}\right](\overline{\rho}\widetilde{k}) = \frac{\partial}{\partial x_j}\left(\frac{\mu_T}{\sigma_k}\frac{\partial \widetilde{k}}{\partial x_j}\right) - \overline{\rho}\widetilde{u_i'' u_j''}\frac{\partial \widetilde{u}_i}{\partial x_j} - \overline{\rho}\widetilde{\epsilon} \tag{5.9}$$

$$\left[\frac{\partial}{\partial t} + \frac{\partial \widetilde{u}_j}{\partial x_j}\right](\overline{\rho}\widetilde{\epsilon}) = \frac{\partial}{\partial x_j}\left(\frac{\mu_T}{\sigma_\epsilon}\frac{\partial \widetilde{\epsilon}}{\partial x_j}\right) - C_{\epsilon 1}\frac{\widetilde{\epsilon}}{\widetilde{k}}\overline{\rho}\widetilde{u_i'' u_j''}\frac{\partial \widetilde{u}_i}{\partial x_j} - C_{\epsilon 2}\overline{\rho}\frac{\widetilde{\epsilon}^2}{\widetilde{k}} \tag{5.10}$$

There are six model constants: C_μ, σ_k, σ_ϵ, $C_{\epsilon 1}$, $C_{\epsilon 2}$, and Sc_T. Each constant assumed to carry a single value, and are tabulated in Table 5.1.

Table 5.1: Typical values for the standard k-ϵ model constants.

Model constants	C_μ	σ_k	σ_ϵ	$C_{\epsilon 1}$	$C_{\epsilon 2}$	Sc_T
Numerical values	0.09	1.0	1.3	1.6	1.90	0.7

While the velocity field can be quite accurately predicted for plane jets, the spreading rate of the axisymmetric jet is often overestimated by about 40% (Pope, 1978) using the above model

constants. Unlike the plane jet, vortex stretching takes place in the axisymmetric jet, leading to a decrease in turbulent kinetic energy and dissipation rate, and consequently the spreading rate. Experimental observations suggest a 15% reduction in spreading rate from the plane jet (Pope, 1978). This phenomenon is called the *round jet / plane jet anomaly*. A remedy for this issue is to alter the single-valued constants in the turbulence model to increase the dissipation rate of turbulent kinetic energy, particularly by increasing the value of $C_{\epsilon 1}$ from the *standard* value of 1.45 to 1.60 (Pope, 1978). Poroseva and Bézard (1999) also proposed a change in $C_{\epsilon 1}$ to 1.47, but the resulting jet did not produce penetration characteristic that were comparable with the current experiment.

5.3 Combustion model

The eddy dissipation concept (EDC) model by Ertesvåg and Magnussen (2000) was used throughout to model turbulent combustion. Based on an earlier model by Magnussen and Hjertager (1976), the EDC model relies on the assumption that the reactions take place only at the Kolmogorov scales (Pope, 2000). The corresponding velocity (u^*) and length (L^*) scales are defined below:

$$u^* = \left[\left(\frac{C_{\epsilon 2}^3}{3C_{\epsilon 1}^2} \right) (\nu \epsilon) \right]^{1/4}, \tag{5.11}$$

$$L^* = \left(\frac{2}{3} \right) \left[\left(\frac{3C_{\epsilon 2}^3}{C_{\epsilon 1}^2} \right) \left(\frac{\nu^3}{\epsilon} \right) \right]^{1/4}. \tag{5.12}$$

In defining the two scales, it is assumed that ϵ can be determined from turbulence modeling, such as the k-ϵ model, and that ϵ is invariant for all length scales according to the turbulence cascade hypothesis. It can be further assumed that the mass ratio between the smallest and

largest turbulent scales, γ^*, can be defined as follows:

$$\gamma^* = \left(\frac{u^*}{u'}\right)^3 = \left(\frac{3C_{\epsilon 2}}{4C_{\epsilon 1}^2}\right)^{1/4} \left(\frac{\nu\epsilon}{k^2}\right)^{3/4}. \tag{5.13}$$

The specific mass transfer among the scales can be defined as:

$$\dot{m}^* = \left(\frac{2u^*}{L^*}\right) = \left[\left(\frac{3}{C_{\epsilon 2}}\right)\left(\frac{\epsilon}{\nu}\right)\right]^{1/2}. \tag{5.14}$$

Note that $1/\dot{m}^*$ has the dimension of time, and is indicative of the time scale of mass transfer. By multiplying Equations (5.13) and (5.14), and expression for mean rate of mass transfer from the surrounding fluid to the fine structures:

$$\dot{m} = \dot{m}^*\gamma^* = \left(\frac{3}{4C_{\epsilon 1}^2}\right)\left(\frac{12C_{\epsilon 2}}{C_{\epsilon 1}}\right)^{1/2} \left(\frac{\nu\epsilon}{k^2}\right)^{1/4} \left(\frac{\epsilon}{k}\right). \tag{5.15}$$

It is assumed that only a fraction of the fine structure χ is sufficiently heated for the reaction to take place:

$$\chi = \frac{\overline{Y}_{\text{prod}}(1 + r_{\text{fuel}})}{\overline{Y}_{\text{min}} + \overline{Y}_{\text{prod}}(1 + r_{\text{fuel}})}, \tag{5.16}$$

where $\overline{Y}_{\text{min}} = \min(\overline{Y}_{\text{fuel}}, \overline{Y}_{O_2}/r_{\text{fuel}})$, and r_{fuel} is the stoichiometric mass fraction of oxygen. Equations (5.13) to (5.16) may be used to compute the local average reaction rates (Magnussen, 2005):

$$\overline{\omega}_i = \frac{\overline{\rho}\dot{m}\chi}{1 - \gamma^*\chi}(\overline{Y}_i - Y_i^*). \tag{5.17}$$

It is assumed that the fine structures have a mass fraction Y_i^* that is calculated by further assuming that these fine structures behave as a well-stirred reactor with an assigned chemical mechanism. This gives the EDC model the flexibility to take into account any detailed reaction model.

Since a reliable combustion description can be obtained from the reduced mechanisms for premixed flames (Peters and Rogg, 1993; Smooke, 1991), a two-step mechanism (Table 5.2) has been adopted to minimize computational effort. The *in-situ* adaptive tabulation (ISAT) approach of Pope (1997) has been utilized to further reduce computational time by 25% to 30%, compared with direct integration over the combustion period.

Table 5.2: Arrhenius parameters for the two-step CH_4 combustion reactions.

Reaction	A [1/s]	n [ ]	E_A [J/kg mol]
$CH_4 + \frac{3}{2}O_2 \rightarrow CO + 2H_2O$	5.01×10^{11}	0	2.0×10^{8}
$CO + \frac{1}{2}O_2 \leftrightarrow CO_2$	2.24×10^{12}	0	1.7×10^{8}

5.3.1 Verification

Verification was also carried out to evaluate the sensitivity of the EDC model to changes in mixture composition. To this end, data were taken from Bentebbiche et al. (2005) for a premixed duct-shaped combustor with a rod-shaped flame holder, as shown in Figure 5.2. the inlet mass flowrate is 35 g/s, evaluated at equivalence ratios ϕ = 0.9 and ϕ = 0.75. The simulation was conducted using the commercial package FLUENT. Qualitatively, the present numerical results (Figure 5.3) were able to correctly capture the flame front location and the cone angle. The outcome of this qualitative study illustrates an important aspect of the EDC model, however, and it is the ability of the model to handle combustion under fuel-lean conditions. Therefore it can be considered suitable for the scope of the present investigation as the accuracy is deemed acceptable.

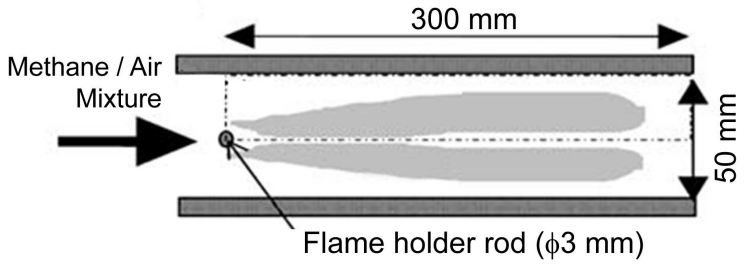

Figure 5.2: Combustor geometry of Bentebbiche et al. (2005).

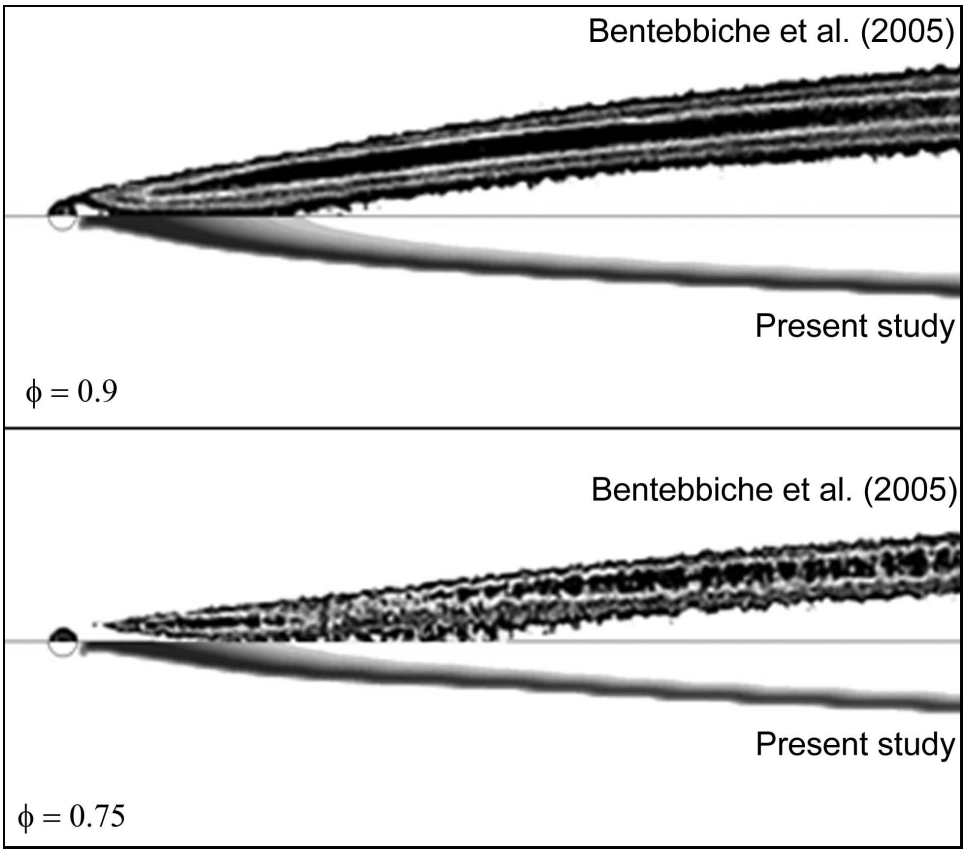

Figure 5.3: Qualitative comparison of reaction rate between the numerical results from the current study and Bentebbiche et al. (2005), for a equivalence ratios $\phi = 0.9$ and $\phi = 0.75$.

5.4 Ignition model

The spark ignition process can roughly be divided into three phases, namely, breakdown, arc, and glow discharge. In the *breakdown* phase, the ignition circuit is closed, and a charge builds up around the spark gap until the electrical potential is high enough to ionize the gas molecules across the spark electrodes. A plasma composed of ionized gases is thus formed and expands outwards, and a shock wave precedes the gas (Arpaci et al., 2003). This phase is, at most, a few nanoseconds in duration, and the appearance of the electrical arc marks the transition into the *arc* phase.

The degree of ionization is drastically reduced following breakdown, though electrical energy transfer still occurs across the spark gap, and heats up the surrounding gas through conduction, which forms spherical flame known as the flame kernel (Zel'dovich et al., 1984). The arc phase typically lasts for a few microseconds, but may be prolonged as long as the discharge current can be accommodated by the ignition circuit (Maly, 1984).

This is followed by the *glow discharge* phase. The remaining electrical energy is deposited in the ignition zone at low efficiency, as the level of ionization continues to decrease. The flame kernel growth is induced by the plasma expansion and ignition of surrounding unburnt mixture. The glow discharge phase persists in the order of milliseconds, and is typically the starting point of many spark ignition models (Herweg and Maly, 1992; Lipatnikov and Chomiak, 2002; Tan and Reitz, 2006).

Empirically, the efficiency of spark energy transfer during the glow discharge phase depends on the discharge method and the local flow conditions. The efficiency ranges from 10% to 30% of the total energy deposited (Tan and Reitz, 2006). Based on electrode spark measurements, Maly (1984) proposed the correlation below to estimate the energy transfer efficiency based on mean flow velocity in the vicinity, and the numerical values of the parameters are based on different spark discharge methods (arc or glow discharge), and are tabulated in Table 5.3.

$$\eta = \eta_0 + \frac{\left(\eta_\infty - \eta_0\right)\overline{u}^3}{A + \overline{u}^3}, \tag{5.18}$$

Table 5.3: Parameter values used in Equation (5.18).

	η_0 [ ]	η_∞ [ ]	A [m^3/s^3]
Continuous arc	0.36	0.50	500
Glow discharge	0.08	0.30	700

The term *kernel maturity* (Eichenberger and Roberts, 1999) is used to describe the period of flame kernel development. It is commonly accepted that a flame kernel is considered to have reached maturity when it is sufficiently large to be advected into the remaining air-fuel mixture in a self-sustaining manner. The criteria for flame kernel maturity may be inferred by the pressure history, kernel expansion speed, or by critical kernel size. The local integral length scale has been chosen Herweg and Maly (1992); Tan and Reitz (2006) as the criteria for flame kernel maturity for the model formulation, as conditions for flame kernel extinction could be determined under this approach (Chan et al., 2011).

5.4.1 Formulation

Spark ignition is a highly complex phenomena requiring proper consideration of energy transfer, plasma expansion, and early combustion behavior. However, A number of simplifying assumptions are made, most of which stem from the small time and length scales involved during flame kernel maturation:

1. To alleviate the need to fully model the breakdown and arc ignition phases, the spark ignition model is assumed to begin at the beginning of the glow discharge phase,

2. The thermodynamic properties of the burnt gas in the flame kernel are uniform in space and time.

3. The temperature of the flame kernel is assumed to be at the adiabatic flame temperature, *and*

4. Thermodynamic equilibrium is assumed, and the ideal gas relations apply in both the burnt (kernel) and unburnt gas regions.

Flame kernel growth. The model development is based on the formulation of Deshaies and Joulin (1984), Herweg and Maly (1992), and Tan and Reitz (2006). The growth rate of the flame

kernel is effectively the rate of fuel consumed by the flame kernel surface, which can be modeled as the superposition of the plasma expansion speed and the developing flame speed (Tan and Reitz, 2006):

$$\rho_b \frac{dV_k}{dt} + \underbrace{\frac{d\rho_b}{dt}}_{\text{zero}} V_k = \rho_u A_k S_b$$

$$\frac{dr_k}{dt} = \left(\frac{\rho_u}{\rho_b}\right)\left(S_p + S_T\right), \tag{5.19}$$

where S_p is the plasma expansion speed, and S_T is the developing flame speed. Both terms require modeling.

Plasma expansion. An expression for the plasma expansion speed can be derived by considering the energy balance in the flame kernel. Figure 5.4 shows the energy sources and sinks around a flame kernel. From the first law of thermodynamics:

$$\dot{U}_k = \dot{Q}_{\text{sp}} + \dot{Q}_{\text{rx}} - \dot{Q}_{\text{ht}} - \dot{H}_u - \frac{d}{dt}\left(pV_k\right)$$

$$m_k \dot{u}_k + \dot{m}_k u_k = \dot{Q}_{\text{sp}} + \dot{Q}_{\text{rx}} - \dot{Q}_{\text{ht}} - \left(m_u \dot{h}_u + \dot{m}_u h_u\right) - \left(p\dot{V}_k + \dot{p}V_k\right), \tag{5.20}$$

where U_k is the energy contained in the flame kernel, Q_{sp} is the energy input from the spark ignition, Q_{rx} reaction energy release, Q_{ht} is the heat transfer from the flame kernel to its surroundings, H_u is the enthalpy of the unburnt mixture. From assumption (3), the thermodynamic properties are time invariant for the period of flame kernel growth. So $\dot{\rho} = \dot{T} = \dot{p} = 0$. In addition, Q_{sp} and Q_{ht} can be amalgamated empirically. Equation (5.20) then becomes:

$$\dot{Q}_{\text{sp}} = \dot{m}_u h_u + \dot{m}_k u_k - p\dot{V}_k - \dot{Q}_{\text{rx}}.$$

Note that $\dot{m}_u = -\dot{m}_k$,

$$\begin{aligned}\dot{Q}_{\text{sp}} &= \dot{m}_k (u_k - h_u) + p\dot{V}_k - \dot{Q}_{\text{rx}} \\ &= \left(\rho_k \dot{V}_k + \dot{\rho}_k V_k\right)(u_k - h_u) + p\dot{V}_k - \dot{Q}_{\text{rx}} \\ &= \dot{V}_k \left[p + \rho_k (u_k - h_u)\right] - \dot{Q}_{\text{rx}}. \end{aligned} \tag{5.21}$$

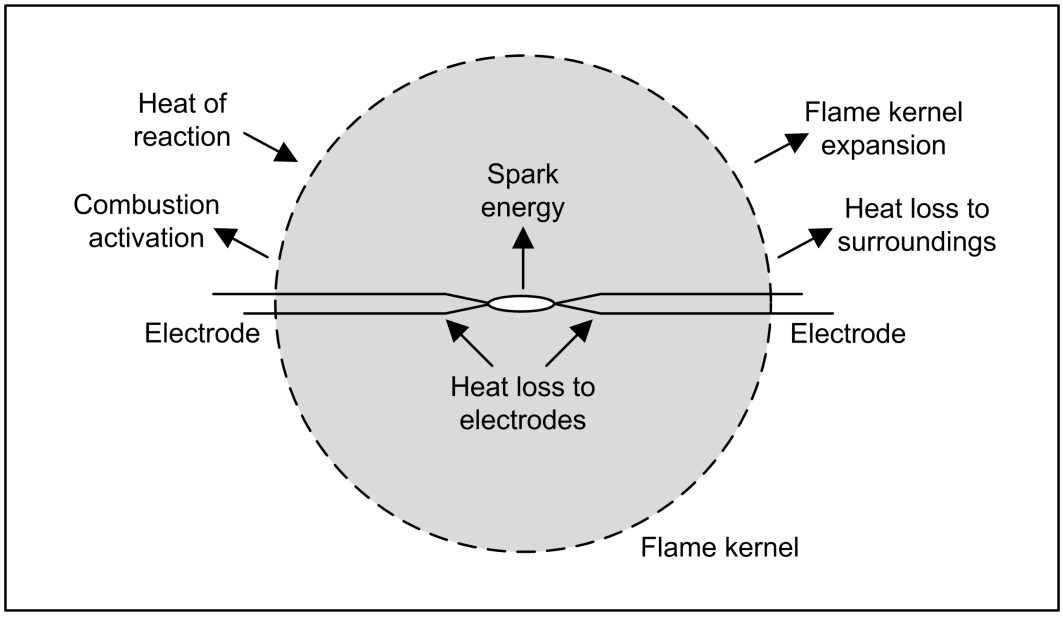

Figure 5.4: Energy balance of the spark ignited flame kernel.

The heat of reaction Q_{rx} can be modeled from Equation (5.21) by eliminating the contributions of spark energy:

$$\dot{Q}_{\text{rx}} = \dot{V}_{\text{fl}} \left[p + \rho_k (u_k - h_u)\right],$$

where $\dot{V}_{\text{fl}}$ is the volumetric expansion of the flame alone, without contribution of the spark energy. Substitution into Equation (5.21) yields:

$$\dot{Q}_{\text{sp}} = \left(\dot{V}_k - \dot{V}_{\text{fl}}\right)\left[p + \rho_k (u_k - h_u)\right].$$

The term $\dot{V}_k - \dot{V}_{\text{fl}}$ is the volumetric expansion of the flame kernel from spark energy alone, which can be modeled from Equation (5.19):

$$\dot{V}_k - \dot{V}_{\text{fl}} = A_k \left(\frac{\rho_u}{\rho_b} \right) S_p.$$

This gives rise to:

$$\dot{Q}_{\text{sp}} = A_k \left(\frac{\rho_u}{\rho_b} \right) S_p \left[p + \rho_k (u_k - h_u) \right],$$

and the closed form expression of the plasma expansion speed thus becomes:

$$S_p = \frac{\dot{Q}_{\text{sp}}}{A_k \left[\left(\rho_u / \rho_b \right) p + \rho_u (u_k - h_u) \right]}, \tag{5.22}$$

which is the result of Deshaies and Joulin (1984).

Developing flame speed. As previously mentioned, the integral length scale approach will be used to derive the expression for the developing flame speed. Following Bray (1990), Herweg and Maly (1992) proposed a modified definition for turbulent burning velocity at moderate to high turbulence levels (i.e., $u' \geq S_L^0$):

$$\frac{S_T}{S_L} = I_0 + \frac{2\sqrt{D_T \dot{\omega}}}{S_L},$$

with the following models for the turbulent diffusion coefficient (D_T) and reaction rate ($\dot{\omega}$) presented below without proof:

$$D_T = \left[u' \left(\frac{\| u \|_2}{\| u \|_2 + S_L} \right) \right] \left\{ L_e \left[1 - \exp\left(-\frac{r_k}{L_e} \right) \right] \right\} \left[1 - \exp\left(-\frac{\| u \|_2 + S_L}{L_e} t \right) \right], \tag{5.23}$$

$$\dot{\omega} = \frac{1}{2} \left(I_0 \frac{u'}{L_e} \right) \left(\frac{u'}{S_L} \right)^{5/3}. \tag{5.24}$$

Provided that $u' \sim S_L$, the expression for S_T/S_L then becomes:

$$\frac{S_T}{S_L} = I_0 + {I_0}^{1/2}\left(\frac{\|u\|_2}{\|u\|_2 + S_L}\right)^{1/2}\left[1-\exp\left(-\frac{r_k}{L_e}\right)\right]^{1/2}\left[1-\exp\left(-\frac{\|u\|_2 + S_L}{L_e}t\right)\right]^{1/2}\left(\frac{u'}{S_L}\right)^{5/6}. \quad (5.25)$$

The flame strain rate, I_0 can be expressed in terms of Karlovitz and Lewis numbers (Chung and Law, 1988; Law et al., 1986):

$$I_0 = 1 - \mathrm{Ka}\left[\frac{1}{\mathrm{Le}} + \left(\frac{\mathrm{Le}-1}{\mathrm{Le}}\right)\left(\frac{T_A}{2T_{\mathrm{ad}}}\right)\right]. \quad (5.26)$$

The Karlovitz number (Ka) can be represented as a superposition of flame curvature and wrinkling (Herweg and Maly, 1992):

$$\mathrm{Ka} = \frac{\delta_L}{S_L}\left(\frac{2}{r_k}\frac{dr_k}{dt} + \frac{u'}{l_T}\right),$$

where l_T is the Taylor microscale. Given that, $S_T \sim S_L$ at the inception of kernel growth, $\dot{r}_k \sim (\rho_u/\rho_b)S_L$. So the expression for Ka can be further expanded:

$$\mathrm{Ka} = \left(\frac{\delta_L}{S_L}\right)\left(\frac{u'}{l_T}\right) + 2\left(\frac{\rho_u}{\rho_b}\right)\left(\frac{\delta_L}{r_k}\right). \quad (5.27)$$

Under isotropic turbulence, the Taylor microscale term (u'/l_T) can be rewritten in terms of the integral length scale (Taylor, 1938):

$$\left(\frac{u'}{l_T}\right)^2 = \left(\frac{3}{2}\right)\left(\frac{C_\mu}{\nu}\right)\left[\frac{(u')^3}{15L_e}\right].$$

Further following manipulation of δ_L (Liñán and Williams, 1993):

$$\delta_L \sim \left(\frac{2\nu}{PrS_L}\right),$$

Equation (5.27) becomes:

$$\mathrm{Ka} = \underbrace{\left(\frac{3C_\mu}{Pr}\right)^{1/2}}_{\sim 1}\left(\frac{\delta_L}{15L_e}\right)^{1/2}\left(\frac{u'}{S_L}\right)^{3/2} + 2\frac{\delta_L}{S_L}\left(\frac{\rho_u}{\rho_b}\right).$$

Substitution back into Equation (5.26) gives rise to

$$I_0 = 1 - \left[\left(\frac{\delta_L}{15L_e}\right)^{1/2}\left(\frac{u'}{S_L}\right)^{3/2} + 2\left(\frac{\delta_L}{S_L}\right)\left(\frac{\rho_u}{\rho_b}\right)\right]\left[\frac{1}{\mathrm{Le}} + \left(\frac{\mathrm{Le}-1}{\mathrm{Le}}\right)\left(\frac{T_A}{2T_{\mathrm{ad}}}\right)\right]. \tag{5.28}$$

For lean natural gas mixture, Le~1, so Equation (5.28) can be further simplified to:

$$I_0 = 1 - \left[\left(\frac{\delta_L}{15L_e}\right)^{1/2}\left(\frac{u'}{S_L}\right)^{3/2} + 2\left(\frac{\delta_L}{S_L}\right)\left(\frac{\rho_u}{\rho_b}\right)\right]. \tag{5.29}$$

Therefore the evolution of the spark-ignited flame kernel can be characterized using Equations (5.20), (5.22), (5.25), and (5.29).

5.4.2 Implementation and verification

The ignition algorithm was implemented in the C++ programming language. The thermodynamic properties and equilibrium conditions were calculated using Cantera (Goodwin, 2007), using detailed kinetics provided by GRI-Mech 3.0 (Smith et al., 1999), with 53 species and 325 elementary reactions. The thermophysical properties of the different species were determined using the NASA thermophysical database (McBride et al., 1993). The laminar flame speed (S_L) for natural gas was calculated directly as a one-dimensional stationary premixed flame problem at different pressures, temperature, and air-to-fuel ratios.

Since the flame speed calculation using detailed kinetics is a computationally expensive task, the laminar flame speed and the corresponding adiabatic flame temperature were computed *a priori*, and compiled into a look-up table. This was achieved by developing a separate

code with Cantera and GRI-Mech 3.0. The results of the laminar flame speed calculations were in excellent agreement with the results of Law (1993) and Vagelopoulos et al. (1994).

The operation of the ignition code was verified using the Schlieren data obtained from Herweg and Maly (1992), which used propane as the working fuel. The parabolic correlation of Metghalchi and Keck (1980) was used to estimate the laminar flame speed of propane, instead of the tabulated laminar flame speed mentioned above. The kernel expansion rates ($\dot{r}_k$) are presented in Figure 5.5. The different RPM values affected the turbulent fluctuation as well as the mean flow velocity through the spark electrodes. This, in turn, also introduced changes to the Karlovitz number, as indicated in Equation (5.27). These values could be found in Herweg and Maly (1992).

Though, in the original formulation of the ignition of Herweg and Maly (1992), the rates of change in engine cylinder pressure and temperature were also considered, the current model assumes that these changes have an insignificant effect in flame kernel growth. The results in Figure 5.5 confirmed these assumptions. Deviations in kernel expansion speed could be observed at the inception of ignition, due to the model assumption of uniform kernel temperature at the adiabatic flame temperature, which subsequently underestimated the plasma expansion speed. Otherwise, the developing flame speed were properly represented, and sufficient agreement could be found between the experimental and numerical data.

5.5 Summary

The models for PSC injection, ignition, and combustion have been rigorously discussed and verified. The jet model made use of the standard k-ϵ model with corrections made to the model constants to reduce overprediction in injection spread (Pope, 1978; Poroseva and Bézard, 1999). An elliptical injection profile was adopted to simulate the mass injection. To improve computa-

tional efficiency, a 1-D ignition model was developed based on the model of Deshaies and Joulin (1984), Herweg and Maly (1992) and Tan and Reitz (2006). For the main combustion event, the Eddy Dissipation Concept (EDC) model was used (Ertesvåg and Magnussen, 2000), using a two-step reaction mechanism for methane to represent natural gas combustion. Test cases were taken from experimental sources and the model results were found to be in good agreement with the corresponding experimental data. This provides confidence for the utilization of these models for the simulation the PSC ignition and combustion under engine conditions, as well as for the constant volume combustion chamber.

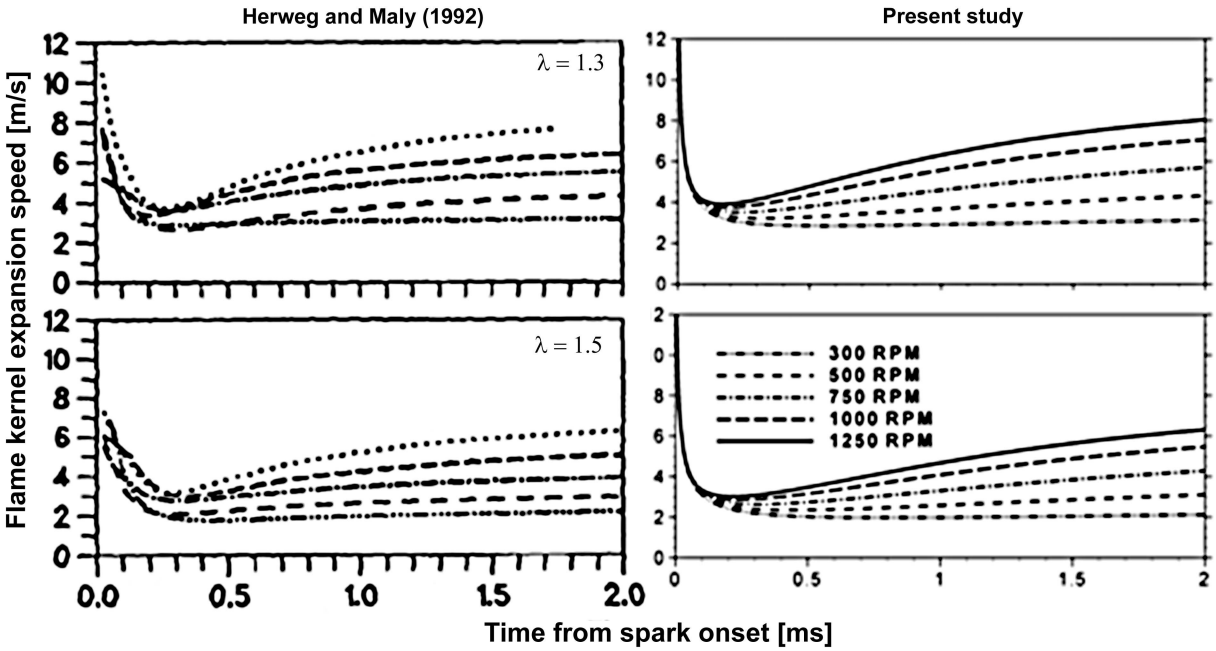

Figure 5.5: Comparison between experimental (Herweg and Maly, 1992) and numerical kernel growth data using the current ignition model.

Chapter 6

Simulation results

The numerical framework described in Chapter 5 were applied to model the CVCC and engine experiments. Initial and boundary conditions were prescribed accordingly to reflect experimental conditions. The numerical results were inspected on three distinct areas. First and foremost was the pre-ignition evolution of the PSC jet in the CVCC. Verification of the numerical results could be inferred by using experimentally obtained penetration and entrainment data. This led to a discussion on the results of early combustion under PSC, for which experimental results were also available for comparison. The numerical framework was then extended to model PSC combustion under engine conditions.

6.1 Combustion chamber simulation results

The purpose of the CVCC experiments is to identify the basic enabling mechanisms for the PSC ignition strategy. There are three primary concerns in the formulation of the simulation strategy. First, due to the relative simplicity of the computational geometry, the spark ignition process could be fully modeled using only an energy deposition approach (Lacaze et al., 2009b). The combustion event was modeled numerically with the Eddy Dissipation Concept (Magnussen, 2005; Magnussen and Hjertager, 1976) model. Meanwhile, it was also important to numerically produce the proper evolution of the PSC injection. This could be accomplished mainly by using a representative injection profile.

6.1.1 Computation domain and operating conditions

An axisymmetric computation domain was used to model the CVCC, as shown in Figure 6.1. The axial length of the solution domain is 50.8 mm, same as of the CVCC. In the meantime, to maintain the same volume as the combustion chamber, the radius of the solution domain was set to 47.1 mm. All crevices and recess regions (such as recess to the viewports) were omitted to simplify computation. The grid consists of 20000 control volumes, with an average mesh spacing of 0.351 mm in each direction. Higher grid density were introduced axially along the injector nozzle, and radially along the spark ignition zone to improve the resolution in critical, rapid changing regions such as the ignition zone, and the core of the PSC jet. The grid was fine enough to fully resolve the local integral length scale throughout the computational domain. The spark ignition zone is located 10 mm downstream of the PSC nozzle, with a gap of 1 mm, symmetric about the central axis. The commercial CFD code FLUENT was used for the simulations. The solution was second-order accurate in space and time, at a constant time step of 0.5 μs, which was sufficiently small to resolve the Kolmogorov time scale. The numerical solution was considered to have converged when the normalized residuals reached below 10^{-3}.

The initial pressure and temperature were set to 7 bar (abs.) and 300 K respectively. The mixture composition was adjusted based on the relative air-to-fuel ratios, while air was assumed to be 21% diatomic oxygen and 79% diatomic nitrogen by volume. Methane was used as the representative component for natural gas. A decaying elliptical injection profile was assumed for the PSC injection, defined in Equation (5.1). The no-slip boundary condition was prescribed at the chamber walls. The walls were also assumed adiabatic, as the main focus was the combustion behavior immediately after ignition. In addition, the heat transfer coefficient had to be obtained experimentally for each case, which was not explicitly determined as the combustion pressure history provided insufficient information.

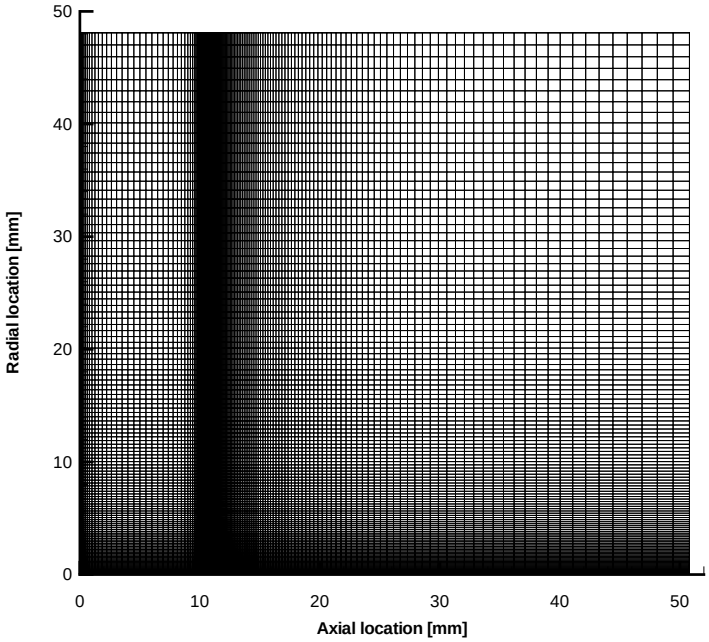

Figure 6.1: Numerical solution domain of the CVCC.

6.2 Pre-ignition PSC jet development

Since the Schlieren images only provided information on the physical evolution of the jet (i.e., penetration and spread), additional information could be inferred from validated numerical data. An examination the formation of the PSC jet provided some insight in relation to the enabling mechanisms discussed in Chapter 4. Particular interest were placed on fuel concentration distribution.

6.2.1 Comparison with experimental data

The pre-ignition evolution of the PSC injection were captured experimentally using the Schlieren visualization system. Figure 6.2 shows a direct comparison in jet development between the a particular set of Schlieren data and the numerical results. To facilitate the comparison, a normalized density variable ($\tilde{\rho}$) was employed so that the numerical data could be represented

as a relative change in density from the ambient value:

$$\tilde{\rho} = 1 - \left(\frac{\rho - \rho_{\text{jet}}}{\rho_{\infty} - \rho_{\text{jet}}} \right) \tag{6.1}$$

Note that, in Equation (6.1), that the ambient density (ρ_{∞}) is typically higher than the PSC jet density at the nozzle (ρ_{jet}). Therefore, a subtraction from unity was performed to normalize the density with respect to the PSC jet. The sensitivity of the Schlieren system was between 1% to 5% in density deviation (Ouellette, 1996). Using $\tilde{\rho}$ also had the advantage of normalizing the jet development data to be standardized across different ambient air-to-fuel ratios.

Referring to Figure 6.2, early into the injection (at 2 ms after SOI), the simulated results had a tendency to overpredict the penetration. This is likely due to the use of the approximated, decaying elliptical injection profile, which might have overpredicted the mass flow rate at the beginning of the injection. The deviation quickly diminished in subsequent time steps, showing excellent agreement between the simulated and experimental data. Otherwise, the numerical model was able to properly predict the amount of jet spread, which was indicative of entrainment.

In addition to direct visual comparison, ensemble data on jet penetration and spread were extracted from each image using the feature detection algorithm described in Section 3.4.3. The jet development was tracked over 88 frames, at 10000 frames per second, and each frame contained 120 samples. The uncertainty in experimental measurement were expressed in a 95% confidence interval. The comparison between the average experimental (Schlieren) and numerical results of the PSC jet penetration and spread is shown in Figure 6.3. There was a slight discrepancy near the beginning of the injection, as previously noted. Though the accuracy of the injection profile might be brought into question, but its effects was not severe, as indicated

in Figure 6.2. For the remainder of the injection, both the experimental and numerical data were in excellent agreement.

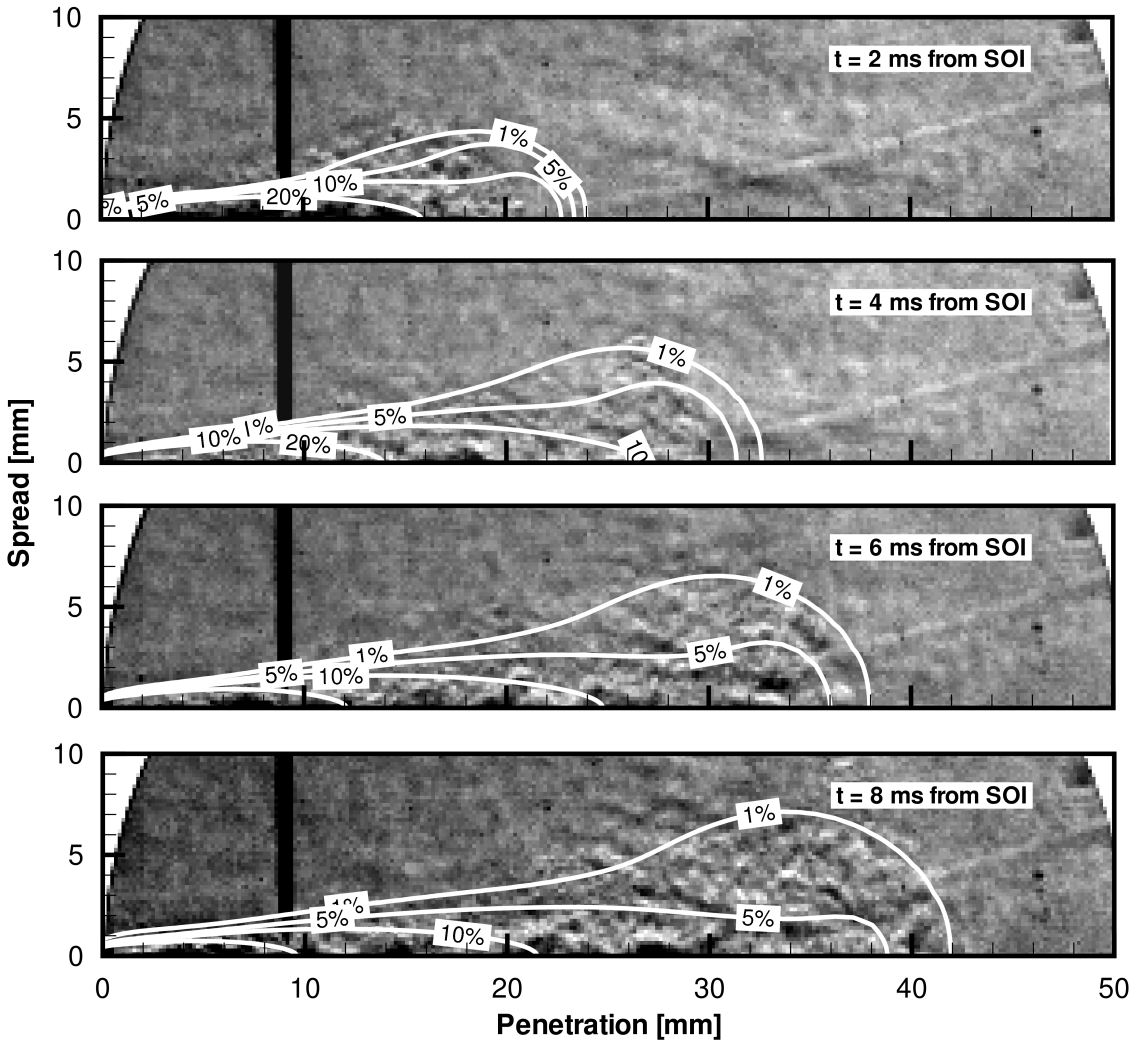

Figure 6.2: Visual comparison between the Schlieren and simulated results. The white lines represent density contours ($\tilde{\rho}$) from the simulations.

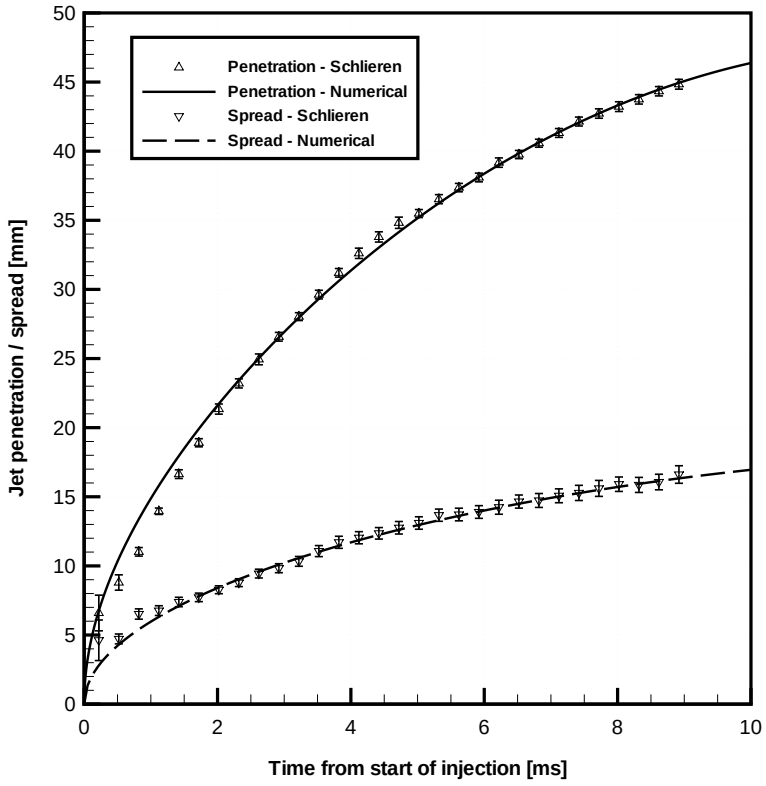

Figure 6.3: Comparison between Schlieren and simulated results for the penetration and spread of the PSC injection.

6.2.2 PSC jet formation and fuel distribution

Following the verification of the simulated jet results, additional observations could be made from the numerical data of the PSC jet. Specifically, the manner in which the PSC jet modified the local fuel concentration and flow field were of particular interest. They were instrumental in establishing the PSC enabling mechanisms, which had been introduced in Section 4.4. The discussion will focus on the pre-ignition behavior of the PSC jet, and, since due to a co-axial injection / ignition configuration, the observations will be inferred from the centerline values.

When the spark signal coincided with the start of the injection (i.e., SOI spark timing), a flame kernel immediately developed as the PSC jet approached the spark ignition zone. Visual examination from the Schlieren images indicated that the interaction between the flame kernel

and the PSC jet tip occurred within the first 0.5 ms from the spark onset. The centerline mean velocity profile is presented in Figure 6.4. During the early stages of injection, a high bulk flow velocity could be observed near the nozzle, resulting from the injection. As pointed out by Maly (1984), under *sustained* high energy deposition, a sufficiently high bulk flow velocity (> 15 m/s) could lead to reignition of additional fresh mixture. The SOI ignition timing allowed the flame kernel to interact with the jet while it had a high flow velocity, prompting more mixture to be ignited.

When the ignition took place near the end of the injection (i.e., EOI spark timing), the jet no longer carried sufficient momentum and the flame kernel growth was restricted to near the ignition zone. Thus, with only one PSC injection, the combustion process thus became slower in the EOI cases observed in the SOI cases for λ = 1.2 to 1.6. This was accompanied by a corresponding decrease in the experimental peak pressure (and heat release), as observed in Figures 4.6 to 4.8, despite having a higher initial energy release (Figures 4.12, 4.14, and 4.16). The reverse was true, however, for the ultra-lean cases (λ = 1.8 and 2.0). Under the EOI spark timing, the PSC jet was already established at the time of the spark, providing a rich mixture as well as a propagation path for stable flame kernel development. This resulted in a more effective penetration into the bulk mixture, which increased the peak combustion pressure, as seen in Figures 4.17 and 4.19.

Additional hydrodynamic influence can be inferred from the local turbulent behaviors at the ignition zone. In the context of eddy viscosity turbulence models, the two critical parameters are the turbulent kinetic energy (k) and the integral length scale (L_e), defined as:

$$L_e = C_\mu \frac{k^{3/2}}{\epsilon}. \tag{6.2}$$

where C_μ is a single valued constant, empirically set to 0.09 for generality, and ϵ is the dissipation rate of turbulent kinetic energy. Figure 6.5 shows the axial distribution of the calculated turbulent kinetic energy of the PSC jet. When the jet tip passes through the ignition zone (at 0.25 to 1.0 ms after SOI), the local turbulent kinetic energy rapidly increased. As entrainment began to take toll, the turbulent fluctuation also diminished as the turbulent kinetic energy cascaded into smaller scales and eventually dissipated. The integral length scale, presented in Figure 6.6, reflected the length of the cascade process. For the early injection, the high turbulent kinetic energy was accompanied with a low integral scale. Bradley et al. (1994) had pointed out that the low integral scale reflected that turbulent fluctuation took place in the lower frequency of the turbulent spectrum. Thus, a hypothetical, developing flame kernel would experience excessive wrinkling, leading to premature extinction.

Another critical factor in the modification of the local ignition conditions is the air-to-fuel concentration. The axial distributions of the relative air-to-fuel ratio at different points of the injection are presented in Figure 6.7. While the jet fuel was ultra-rich ($\lambda < 0.4$) at the location of spark ignition, a transition in fuel concentration could be observed between 0.25 ms and 0.5 ms after the SOI, when the jet tip first reached the spark location. The fuel concentration decreased slightly, as the injection continued, as a result of entrainment with the bulk mixture. While the local mixture was rich, the spark plasma would still be able to ignite the portion of the jet within the flammability limits as the ignition plasma was expanding. Provided that the local turbulence did not excessively reduce the flame kernel temperature, the plasma would ignite the PSC jet.

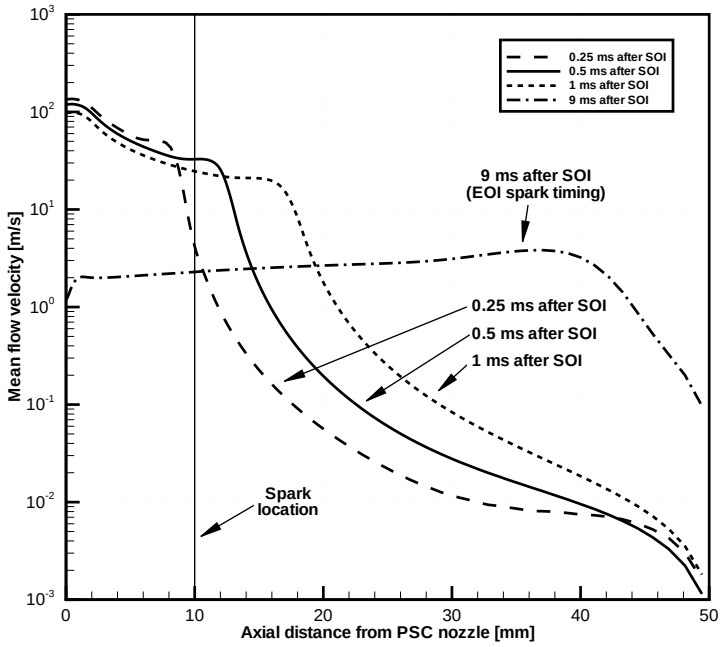

Figure 6.4: Distribution of axial mean flow velocity of the PSC jet along the axis of symmetry.

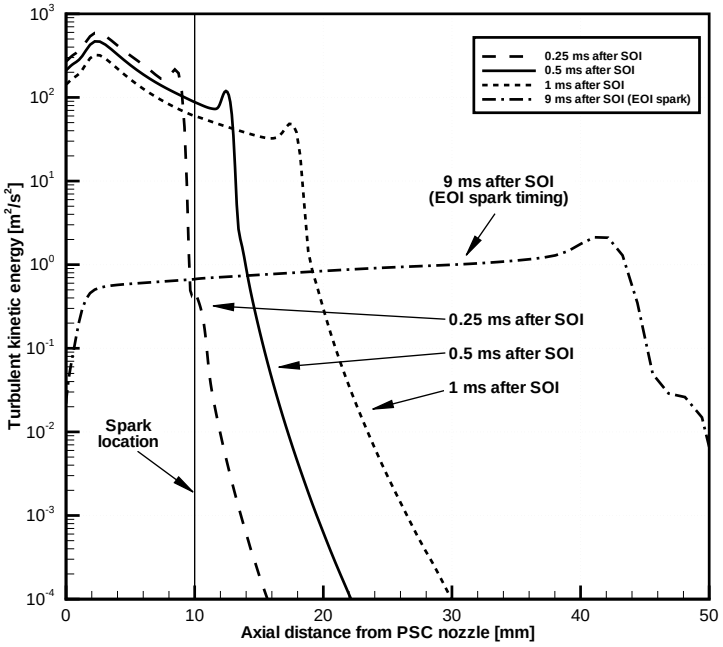

Figure 6.5: Distribution of turbulent kinetic energy of the PSC jet along the axis of symmetry.

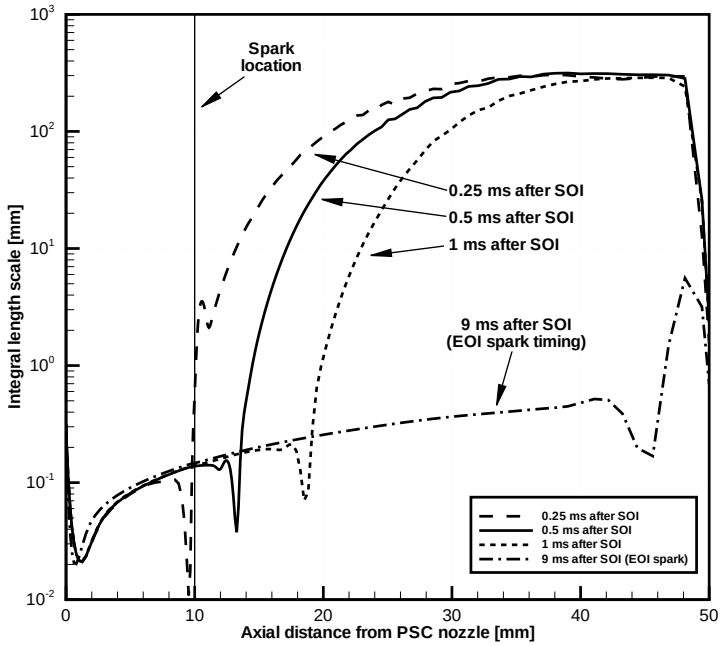

Figure 6.6: Distribution of integral length scale of the PSC jet along the axis of symmetry.

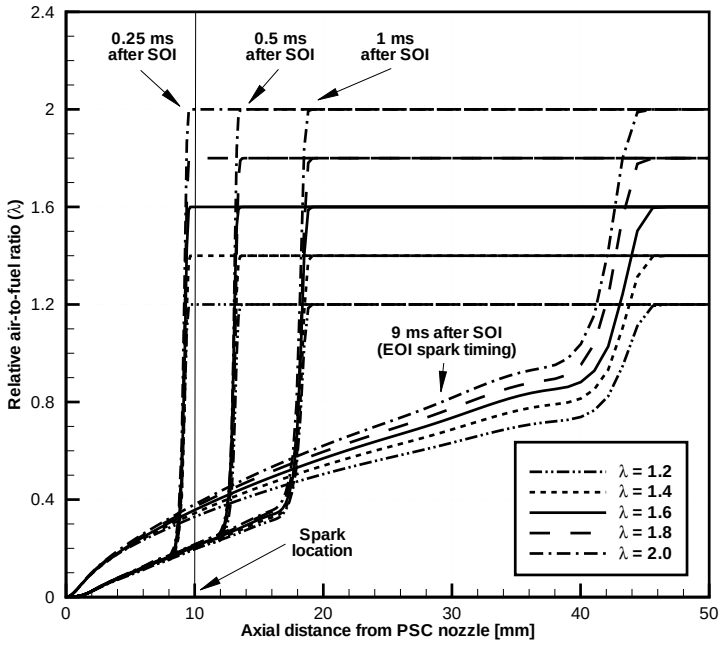

Figure 6.7: Distribution of relative air-to-fuel ratio (λ) of the PSC jet along the axis of symmetry.

6.3 Constant volume PSC combustion

Once the numerical results of the pre-ignition PSC jet evolution were ascertained, models for ignition and combustion could be introduced. Due to the length of the spark discharge, the energy would have been exposed to varying flow conditions and fuel distributions. As a result, the spark ignition was modeled as a direct deposition of energy. The time step was sufficient small ($\Delta t = 5\mu s$) that the energy transfer and the resulting chemical energy release could be resolved. The SOI, EOI, and EOI×2 spark ignition timings were modeled. The EDC combustion model was used for all cases.

Figures 6.8 and 6.9 show a qualitative comparison of the flame front location between the numerical and experimental data for the PSC cases. A representation of the simulated flame front could be visualized using isotherms near the autoignition temperature of methane (~ 900 K). For the moderately lean cases (λ = 1.2 to 1.6), the numerical results overpredicted the penetration rate of the PSC flame front into the bulk mixture. This is likely due to the treatment of the reaction rate in the EDC model, and its inability to properly render the transition from a turbulent flame from the PSC jet to the laminar, substantially quiescent flame in the bulk mixture. The issue of overprediction appeared to have diminished in the ultra-lean cases (λ = 1.8 and 2.0). As the bulk mixture was further leaned out, the combustion rate became more heavily dependent on the propagation of the PSC jet flame. The overprediction in penetration could still be observed in certain ultra-lean cases, particularly at the end-of-injection ignition timing.

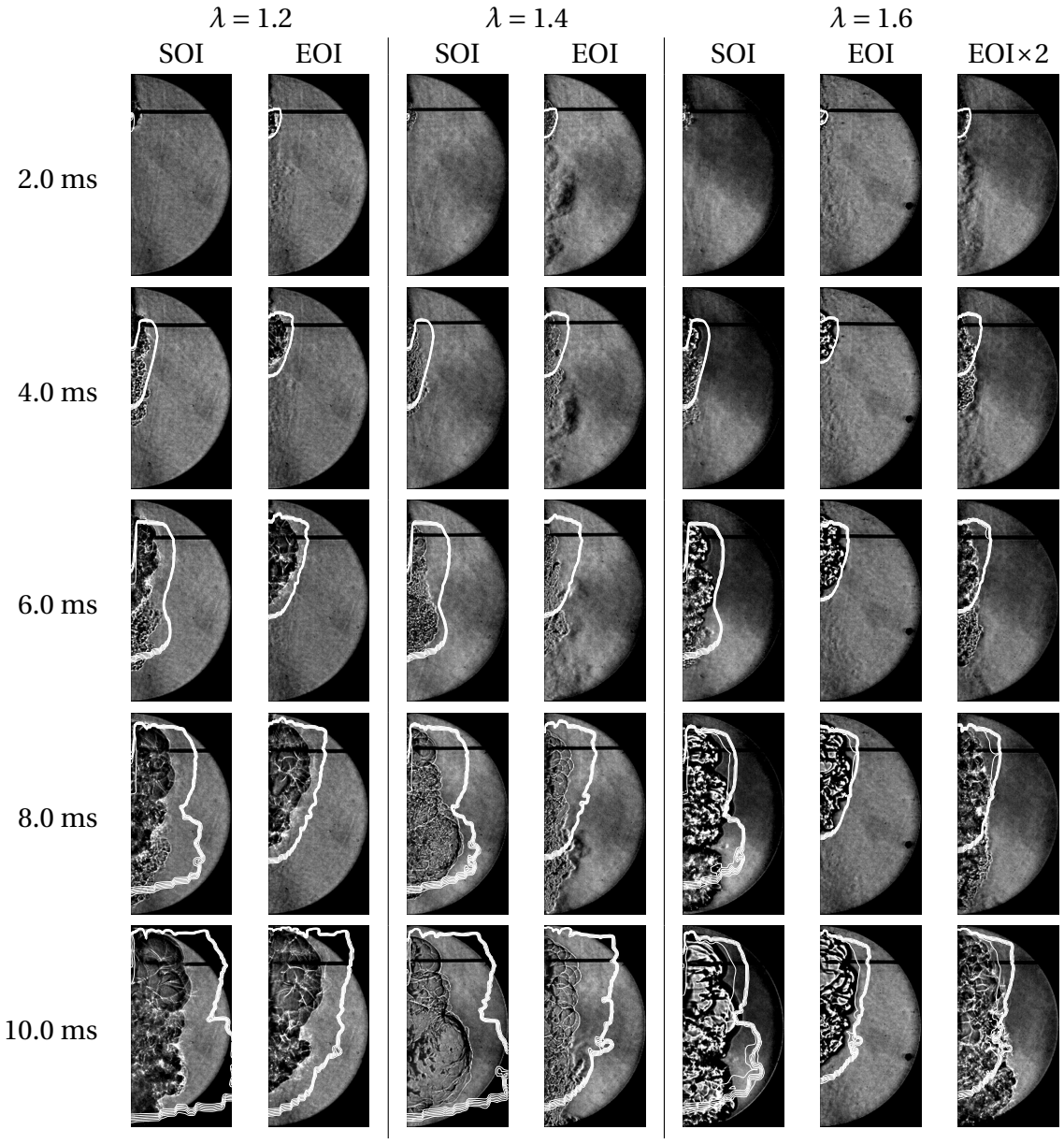

Figure 6.8: Comparison between simulated (white outline) and experimental data for all PSC cases at λ = 1.2, 1.4, and 1.6, at specific times elapsed from spark onset. The simulated outlines are isotherms identifying the flame front location.

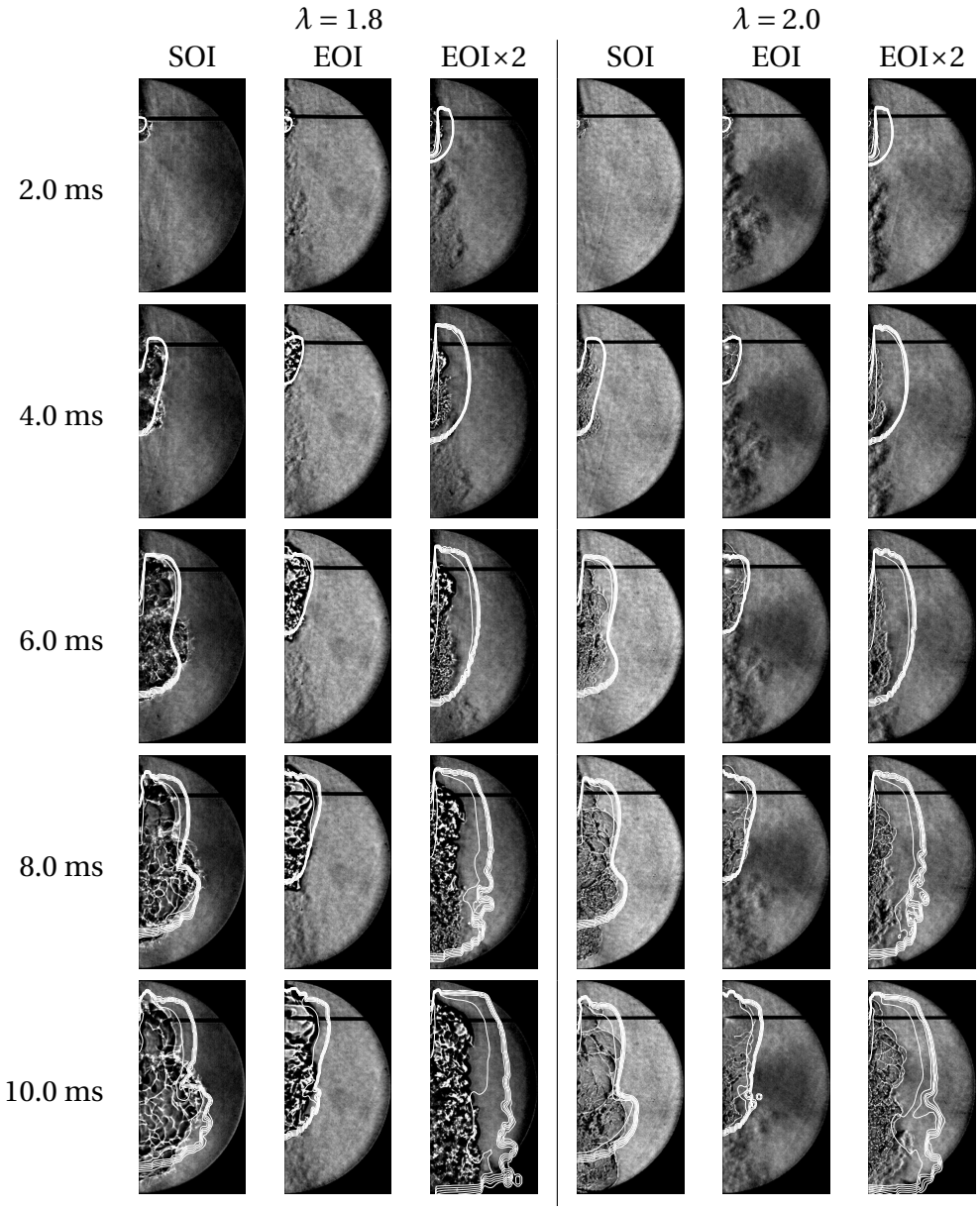

Figure 6.9: Comparison between simulated (white outline) and experimental data for all PSC cases at λ = 1.8 and 2.0, at specific times elapsed from spark onset. The simulated outlines are isotherms identifying the flame front location.

6.4 Combustion engine simulation results*

The development of a numerical framework to model the injection, ignition and combustion processes of a PSC-equipped internal combustion engine has been conducted jointly between the University of British Columbia and the Università degli Studi di Roma “Tor Vergata” in Italy (Andreassi et al., 2003a,b, 2004; Reynolds et al., 2005). Special attention was given to the coupling between the three processes. The PSC injector spark plug was modeled with detail, as it is crucial in obtaining a representative PSC plume distribution (Chan et al., 2007; Mezo et al., 2008).

6.4.1 Experimental setup

The PSC ignition system was implemented on a Ricardo Hydra single cylinder research engine (SCRE) as described by Reynolds and Evans (2004a). The corresponding specifications are presented in Table 6.1. The natural gas PSC-charge was injected using a modified Bosch XR4CS spark plug, metered by an Omega SV 121 solenoid valve through a capillary tube. The test cycles were performed on the SCRE for homogeneous and PSC spark ignition operations at 2000 RPM with wide open throttle (WOT) and varying overall air-to-fuel ratio (λ) so part-load operation could be achieved without throttling losses. The spark advance was adjusted to provide the mean best torque. the statistical data for each operating point were obtained over 100 consecutive engine cycles, as summarized in Table 6.2. The PSC injection pressure and timing with respect to the signal remained unchanged, and are presented in Table 6.3.

*This section is a modified version of the journal article entitled "Numerical and experimental characterization of a natural gas engine with partially stratified charge spark ignition" by E.C. Chan, M.H. Davy, G. de Simone and V. Mulone, to appear in the ASME Journal of Engineering for Gas Turbine and Power in 2010.

Table 6.1: Specifications of the Ricardo Hydra SCRE.

Number of valves	4
Firedeck geometry	Flat
Configuration	SI with PSC
Fuel	CNG
Bore × stroke [mm]	81.4 × 88.9
Connecting rod [mm]	158.0
Compression ratio	9.25
Displacement [cc]	463
Volume at TDC [cc]	56.1

Table 6.2: Specifications of the Ricardo Hydra SCRE.

Operation	**Premixed**		**PSC**	
Overall air-to-fuel ratio (λ)	1.0	1.53	1.53	1.68
Spark timing [°BTDC]	25	51	45	53
Mean IMEP [bar]	8.47	6.13	5.96	5.37
CoV IMEP [%]	0.759	2.83	1.74	4.30

Table 6.3: PSC injection parameters.

PSC fuel (no mixture)	CNG
Capillary tube length [mm]	480
Capillary tube diameter [mm]	0.571
Inlet pressure [bar]	25
Mean mass flowrate [g/h]	40
SOI [° before spark timing]	10
Injection signal width [CAD]	8

6.4.2 Computational model details

The computational domain used to represent the behavior of the Ricardo Hydra SCRE is shown in Figure 6.10. A very fine mesh was constructed around the PSC spark plug injector (Figure 6.11) to capture the development of the PSC plume. The computational grid consists of approximately 306 000 cells, with an average grid spacing of 0.287 mm in the vicinity of the injector, 1 mm for the combustion chamber, and 1.42 mm for the intake and exhaust manifolds. The grid is considered to be sufficiently small to resolve the local integral length scale.

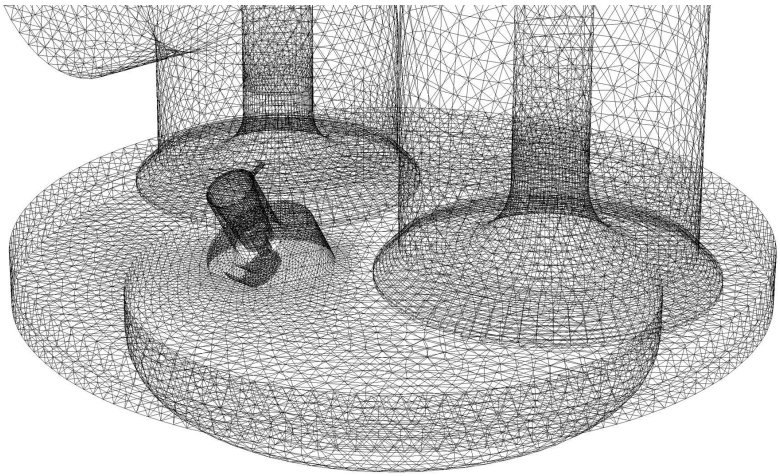

Figure 6.10: Computational grid for the Ricardo Hydra PSC simulation at TDC.

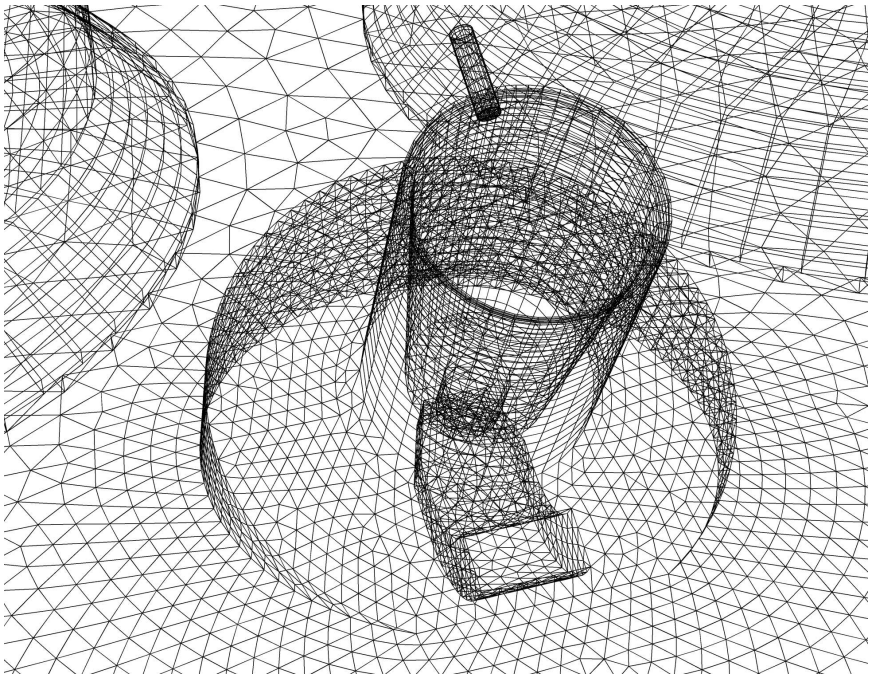

Figure 6.11: Mesh details in the vicinity of the PSC spark plug.

The ignition model (Section 5.4.1) was incorporated into the CFD model as a user-defined function. during the simulation, local flow and fuel conditions in the ignition zone were collected at the spark timing. From the information, the ignition code calculated the flame kernel temperature, radius, and maturity time, which were returned to the simulation at the

maturity timing. The patching of the flame kernel data also activated the combustion model. Each simulation was executed for multiple cycles until the cyclical residual gas fraction reached an asymptotically stable value. Although this procedure was computationally intensive, it eliminated the uncertainty in residual gas fraction, as it could not be measured easily in engine experiments.

6.4.3 Limits of spark ignition

From Section 5.4.1, the laminar flame strain rate I_0, can be expressed as a linear combination of geometric and turbulent factors. Recall Equation (5.27):

$$Ka = \left(\frac{\delta_L}{S_L^0}\right)\left(\frac{u'}{l_T}\right) + 2\left(\frac{\rho_u}{\rho_b}\right)\left(\frac{\delta_L}{r_k}\right).$$

Note that the geometric contribution vanishes as the flame kernel radius, r_k, increases. This suggests that the flame kernel maturation is dominated by local flow and mixture conditions. The resultant criterion for a successful ignition event is thus

$$U' \equiv \left(\frac{\delta_L}{15L_e}\right)^{1/3}\left(\frac{u'}{S_L}\right) < 1.$$

The term U' is termed *turbulent ignition parameter*. As U' approaches unity, I_0 approaches zero, resulting in an asymptotic increase in kernel maturation time (Figure 6.12). This behavior in kernel maturity can be normalized with U', as shown in Figure 6.13. Thus, U' is an indicator for the success of ignition. Furthermore, the laminar flame speed, S_L, is seen to affect the sensitivity of U', thus a flame kernel will file to mature even at low turbulence levels when the mixture is extremely rich or lean.

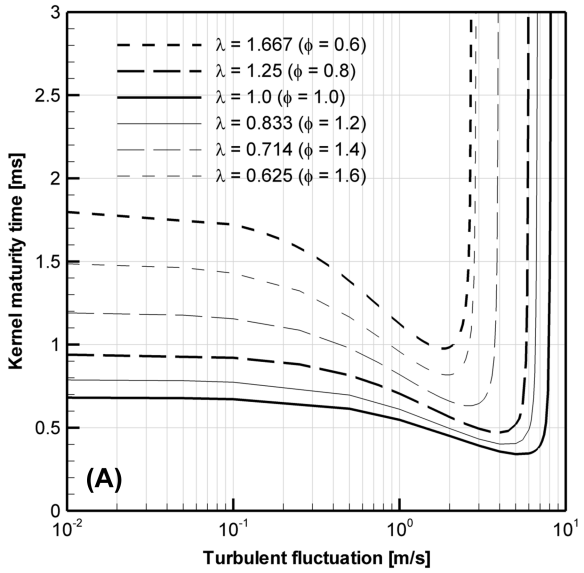

Figure 6.12: Kernel maturity time as a function of turbulent fluctuation at different air-fuel ratios.

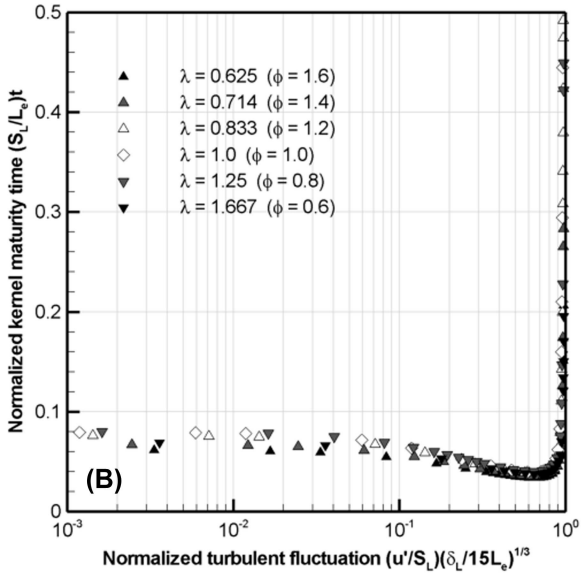

Figure 6.13: Normalized kernel maturity time as a function of the turbulent ignition parameter U'.

6.4.4 Results and discussion

Figure 6.14 shows the comparison between the numerical and experimental pressure traces and the energy release rates for both the homogeneous and PSC cases. The experimental results were represented by a bound at two standard deviations abut the mean, along with the scatter of peak pressure for all the samples. For the homogeneous cases, the peak pressure and energy release rate decrease were expected with the increase in λ. The introduction of PSC (at λ=1.53) resulted in a significant decrease in coefficient of variation (CoV) indicated mean effective pressure (IMEP), as shown in Table 6.2, indicating a more stable engine operation. Furthermore, under PSC, it was also possible to extend the lean operation to λ = 1.68 while maintaining the peak pressure and heat release levels with relatively low CoV IMEP, at only 4.3%.

The simulated data presented in both figures were in excellent agreement with the experimental mean. This was indicative of the ability of the ignition code to properly predict the kernel maturity time; and the turbulent combustion model to reliably represent the coupling between chemical kinetics, the turbulent field and the overall rate of reaction. The slight discrepancy between the numerical data and experimental mean could be attributed to the representation of wall heat transfer, volumetric efficiency, and fuel selection in the model.

Furthermore, the effects of PSC and kernel growth could be quantified with the ignition model. Table 6.4 shows the results from the ignition model based on the data collected from the simulation at the spark timing. The time reported to reach maturity ranged from 0.35 ms to 0.7 ms, roughly 6 to 8.4 crank angle degrees (CAD) at 2000 RPM. There was no observable deviation in numerical cylinder pressure from the experimental mean during kernel growth, which suggested the validity of the negligible pressure rise assumption (Section 5.4.1) for the ignition model. The turbulent ignition parameter is also useful in predicting ignition behavior. For the homogeneous cases, the increase in λ resulted in a rapid increase in the turbulent

ignition parameter, U', leading to a longer kernel maturity time (t_k) and lower flame kernel temperature (T_k). From Table 6.4, the magnitude of U' for both the PSC cases were comparable with the homogeneous stoichiometric case. The local fuel enrichment allowed the flame kernel to develop more rapidly and at a substantially higher temperature than with an equivalent homogeneous mixture.

Figure 6.15 shows the progress of combustion from -10° to +2° TDC for the simulation cases considered. The overall combustion speed and temperature were dependent on λ as expected. As leaner mixtures has slower flame speeds and cooler flame temperatures than stoichiometric mixtures, the effect on flame thickening also became more evident, corresponding to a low Damköhler number. This confirmed the ability of the EDC turbulent combustion model to predict the transition to a thickened flame regime. The presence of PSC, as previously indicated, modified the local fuel concentration, and allowed the flame kernel to develop at a higher temperature and flame speed, particularly for the ultra-lean case (λ = 1.68), where the flame kernel would fail to mature. However, as the PSC flame kernel penetrated into the bulk mixture, the burnt mixture temperature was substantially lower, and thus exhibits higher diffusion than the homogeneous cases. This results in lower NO_x production.

Table 6.4: Specifications of the Ricardo Hydra SCRE.

Simulation case	U'	t_k [ms (CAD)]	r_k [mm]	T_k [K]
Premixed, λ = 1.0	0.216	0.351 (4.21)	2.10	2113
Premixed, λ = 1.53	0.724	0.624 (7.49)	2.77	1865
PSC, λ = 1.53	0.407	0.397 (4.76)	2.70	2114
PSC, λ = 1.68	0.291	0.348 (4.18)	2.78	2270

6.5 Summary

The results of the PSC numerical simulations had shown good agreement with existing experimental results. The PSC injection was modeled using the standard k-ϵ model with a decaying elliptical injection profile. The numerical results matched the experimental data in terms of

the penetration and entrainment of the PSC jet. Further inspection of flow behaviors along the centerline of the jet suggested that flame displacement and reignition are the principal mechanisms for PSC flame initiation.

The early onset of PSC combustion was also modeled. Using the Eddy Dissipation Concept (EDC) combustion model, the maturation and propagation phases of PSC flame development could be captured properly, while an overprediction could be observed in penetration rate for the moderately lean cases. This is believed to be a consequence of lacking an adequate reaction model for the transition from turbulent to laminar flames.

Moreover, a comprehensive, open geometry model of the PSC-enabled, Ricardo Hydra SCRE has been developed and tested with respect to corresponding experimental data. The simulated pressure and energy release results (Figure 6.14) were in good agreement with the experimental data, validating the turbulence, combustion, and ignition submodels. The ability of the flame kernel to survive to maturity could be measured with the turbulent ignition parameter (U') and, from a design standpoint, the results obtained from the numerical engine study allowed the establishment of a comprehensive numerical framework that would ultimately help further the optimization of PSC geometry and operating parameters.

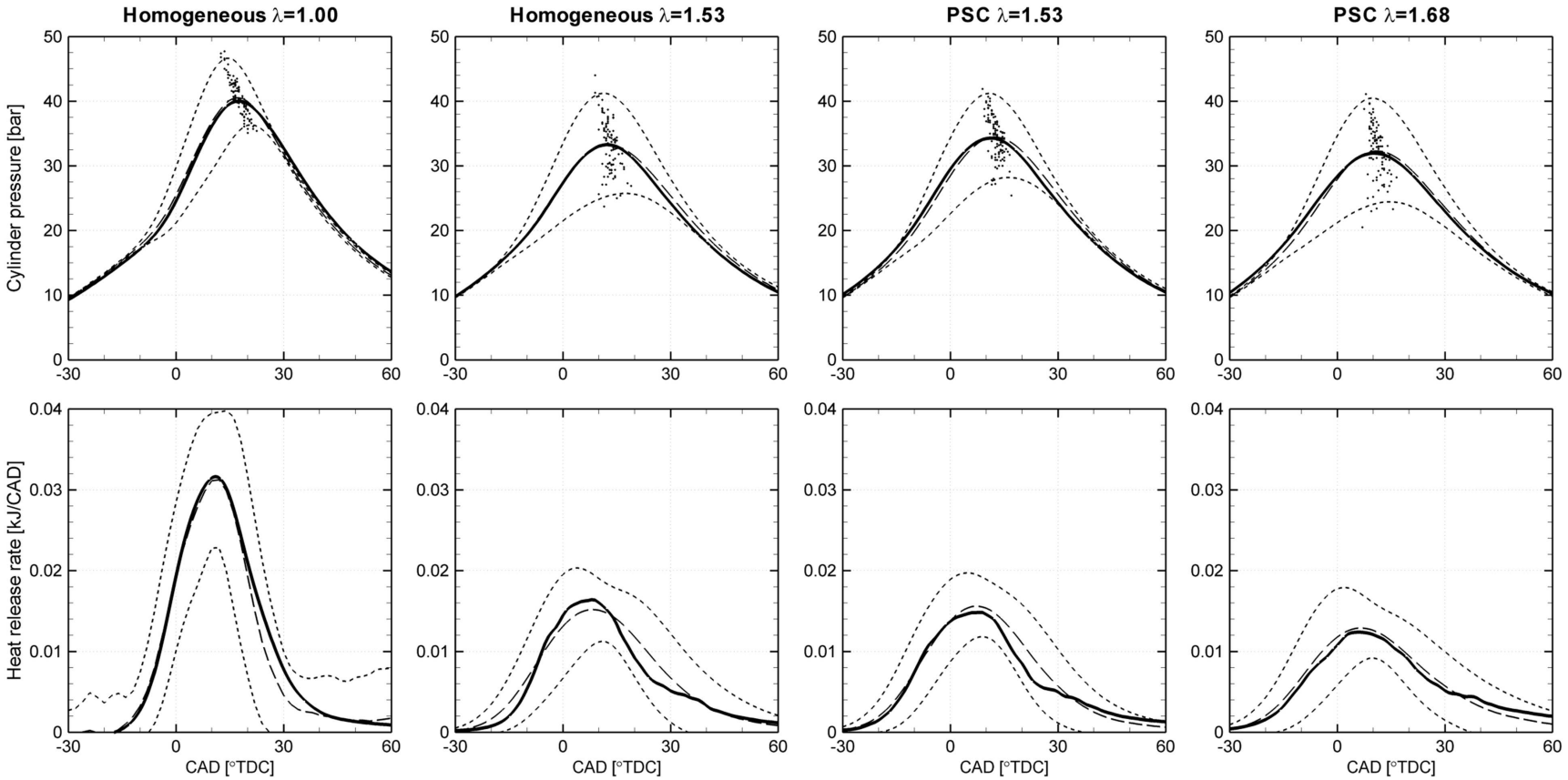

Figure 6.14: Pressure trace and heat release rate of homogeneous and PSC combustion cases for the Ricardo Hydra SCRE. All cases are performed at 2000 RPM and WOT with 100 consecutive samples (key: — numerical result; – – experimental mean value; - - - 2 SD bound about the experimental mean; ... experimental peak pressure scatter)

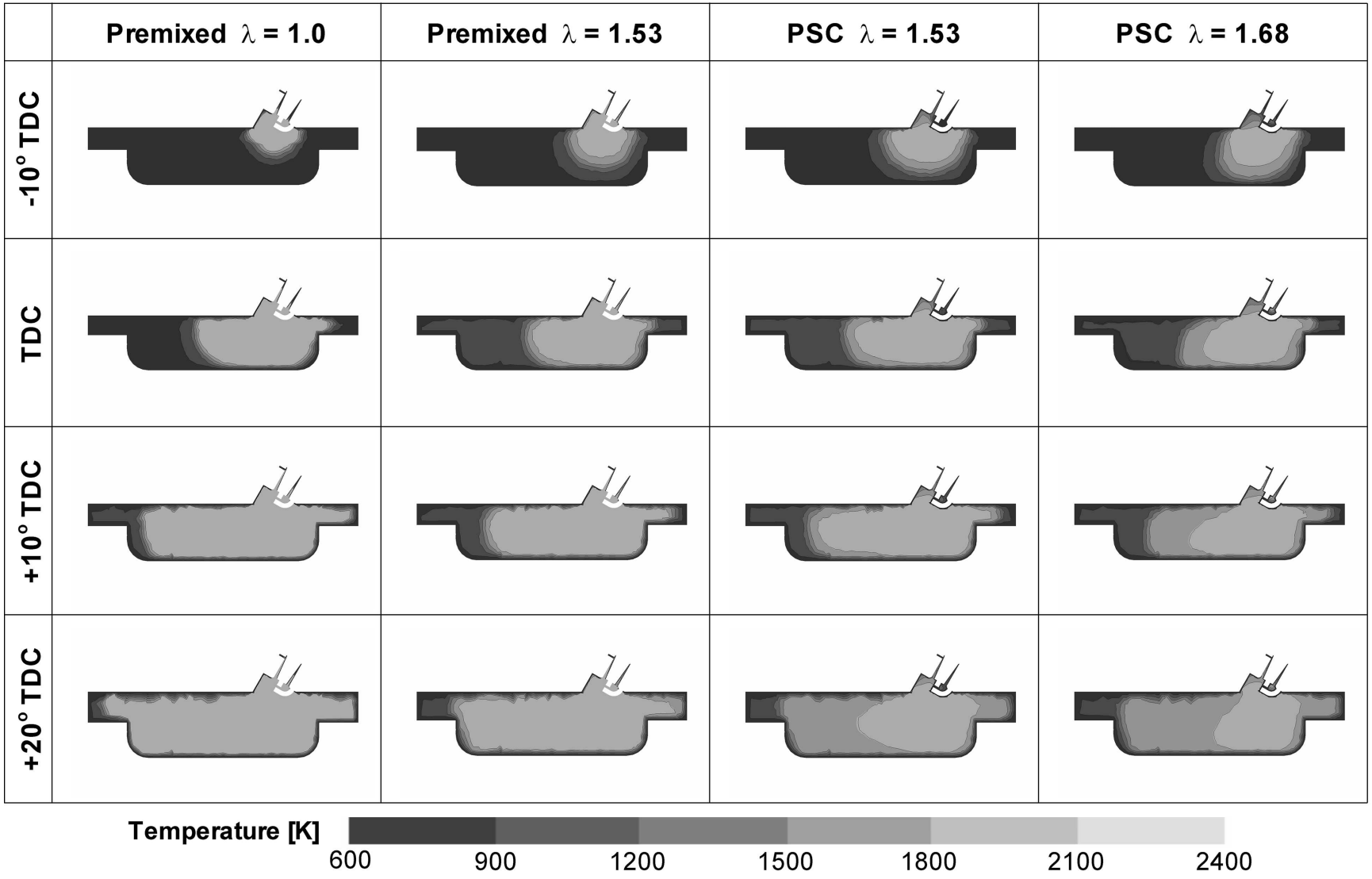

Figure 6.15: Temperature distribution for all operating cases during the combustion period.

Chapter 7

Conclusions

The objective of this research centers on identifying the principal enabling mechanisms pertaining to the partially stratified charge (PSC) spark ignition strategy in a homogeneous air-fuel environment. Particular emphasis has been placed on the development of the flame kernel, as well as early combustion behavior. Simplifications were introduced to idealize the PSC injection and ignition system to minimize confounding effects resulting from specific injection geometries and bulk charge movement. The same idealizations also restrict the PSC injection as the sole factor for turbulence generation and fuel stratification.

An optically accessible constant volume combustion chamber (CVCC) was designed and built for this study. The PSC injection, ignition, and the combustion events were captured using high-speed Schlieren motion photography. A modified commercial CNG / LPG port injector was used to provide the PSC injection. The three parameters of interest are first, the spark timing relative to the injection, the overall air-fuel ratio (λ), and the method of PSC injection. In addition to the Schlieren images, the pressure history was also recorded as an indicator of combustion quality.

The spark ignition in the CVCC was also modeled numerically, using the standard k-ϵ model in an axisymmetric solution domain. A decaying elliptical injection profile was used to model the injection. The energy deposition approach was used to initiate ignition, and the Eddy Dissipation Concept (EDC) model was used to model the combustion process, using a two-step methane reaction mechanism. The modeling framework was also applied to the simulation

of a PSC-equipped internal combustion engine, which utilized the open-geometry concept to resolve charge movement and residual gas fraction. A semi-analytical ignition model was also implemented to characterize the maturation of the flame kernel.

7.1 Significant findings

The current research represents a significant departure from the existing works on PSC in two ways. First, it is the only comprehensive study to employ a simplified geometry, providing a fundamental insight into the interaction between the PSC injection and the bulk mixture alone. Second, the current study was able to demonstrate, under PSC, that stable combustion could be achieved at an ultra-lean level. A number of additional observations were also made from this study.

7.1.1 Enabling mechanisms of PSC

Traditionally, it was believed that the stabilization of flame kernel growth was essential for a stable PSC operation. This derived from the believe that, once ignited, locally fuel-rich flame kernels would contain higher energy than fuel-lean kernels, allowing the flame surface to wrinkle while still maintaining a sufficiently high temperature to ignite the surrounding unburnt mixture. Based on the experimental results, while flame kernel stabilization is important, a stable flame kernel does not necessarily lead to subsequent combustion, especially with a lean bulk mixture. This is because the flame propagates much more slowly in fuel-lean mixtures. Additional mechanisms must therefore be introduced to facilitate transition of the PSC flame kernel into the bulk mixture.

Specifically, from the experiment, three enabling mechanisms were identified, and proved to be mutually beneficial in enhancing combustion beyond the ultra-lean level:

Maturation. This refers to the aforementioned process of flame kernel maturation. The PSC fuel jet helps stabilize ignition through the introduction of a fuel pocket near the ignition zone. This reduces the sensitivity of the flame kernel to turbulent fluctuations, decreasing the probability of extinction resulting from heat loss through flame wrinkling.

Propagation. The second phase of PSC combustion is characterized by the preferential consumption of the richer PSC jet. The propagation phase served to enhance interaction between ignited PSC jet flame with the bulk mixture by increasing flame surface area.

Penetration. The transition from the PSC flame to the bulk mixture. The increased flame surface from the propagation phase increases the amount of bulk mixture to be initially ignited, which accelerates the consumption of the lean mixture.

7.1.2 PSC injection enhancements

Based on the three phases of PSC combustion, an effective propagation strategy could facilitate penetration of the PSC flame into the bulk mixture. This accelerates the propagation phase. Additional energy release could be achieved from combustion of the ultra lean bulk mixture.

7.1.3 Implications on engine conditions

The CVCC experiments did not explicitly account for bulk charge movement, turbulence, and a changing chamber volume, all of which occur under engine conditions. While increased pressure, temperature, and turbulence lead to a corresponding increase in the fully-developed turbulent flame speed, excessive turbulence would likely hinder flame kernel growth. However, provided that a flame kernel could be established, enhancement could be observed in the turbulent flow field.

For the purpose of quantifying the flame kernel sensitivity to turbulence, the turbulent ignition parameter (U') was introduced. Analysis of the ignition model indicated leaner mixtures were more sensitive to turbulent fluctuations. The PSC fuel allows ignition to take place in a richer mixture, which stabilizes flame kernel growth under turbulence. This was later confirmed in engine simulations, where, under PSC, ignition conditions could be found to be compatible with stoichiometric, homogeneous spark ignition.

7.1.4 Implications on optimal PSC design

The current PSC design, as seen from existing combustion chamber experiments and engine simulations, aims to maintain a fuel rich charge near the spark ignition zone. As mentioned in 7.1.1, the maintenance of a stable flame kernel was insufficient to improve the overall combustion. Future designs should aim to facilitate all three phases of PSC combustion, particularly the propagation phase. A possible recommendation would be to reorienting the PSC jet ports in such a way that the ignition paths can be established between the flame kernel and the bulk mixture. Moreover, the concept of dual PSC injection, should also be investigated, since experimental evidence demonstrated the additional bulk charge energy release using the dual injection approach, particularly in ultra-lean mixtures.

7.2 Additional findings

A number of additional observations were also made throughout the research. These findings are integral in reaching the goals of the present research and are noted below.

7.2.1 Analytical limit of ignition

It is expected, in a locally turbulent flow field, there exists a limit beyond which the spark ignited flame kernel would fail to grow and propagate. This is confirmed by the observation of an

asymptotic relationship between the turbulent ignition parameter (U') and the time required for the flame kernel to reach maturity. This relationship is strongly dependent on the local turbulent fluctuation, as well as the local laminar flame speed. Not surprisingly, the flame kernel becomes increasing more sensitive to turbulence the further the air-fuel mixture deviates from stoichiometric composition.

7.2.2 Injector design

The customized PSC injection system was instrumental in obtaining repeatable experimental results. The modifications served to increase the operating pressure range, and to reduce the injection mass and duration. The modified injector was able to provide a sufficient amount of fuel for ignition to occur in a stable manner, but did not significantly affect the overall air-to-fuel ratio. This represents a major achievement from existing PSC research, where lack of a fully controllable injection had been of primary concern.

7.2.3 Image processing

The use of image processing techniques are instrumental for quantifying and streamlining vast amount of experimental data into useful summary results. The usefulness of this approach is demonstrated in its use for verifying the numerical PSC jet penetration and entrainment behaviors.

7.3 Future research directions

Several points of interests have surfaced during the research project, which might serve as starting points for additional projects, either at an application or a fundamental level.

7.3.1 PSC-related research

A number of novel ideas have been proposed as a direct result of the present research. The PSC system was found to facilitate ultra-lean bulk mixture combustion if the injection allowed the PSC flame kernel to be propagated directly into the mixture. Moreover, the rate of this propagation could be accelerated by using an additional injection shortly after the initial injection, allowing the flame to be displaced more quickly into the bulk mixture. The impacts of these concepts have yet to be evaluated under engine conditions.

7.3.2 PSC in a fully turbulent flow field

The combustion chamber PSC experiments have so far been focused on a quiescent bulk mixture. A turbulent flow field was, however, more typical under engine conditions. Though the present study suggest additional improvement with a turbulent bulk mixture, this has yet to be quantified. The use of turbulent generating devices in the constant volume combustion chamber (such as a fan or a moving grid), or optically accessible engines, would be reasonable starting points in extending the current study for a fully turbulent setting.

7.3.3 Transitional flame modeling

The Eddy Dissipation Concept model was able to capture the PSC maturation and penetration phases reasonably accurately. For moderately lean cases, the lack of consideration for the turbulent-to-laminar transition resulted in an overprediction in combustion rate. A numerical model that could predict reaction behavior in this transitional zone would prove useful. Additional accuracy can also be achieved using more detailed simulation techniques such as direct numerical and large eddy simulations.

7.3.4 Lewis number effects

The present research has been limited to natural gas combustion, while a Lewis number of near unity. Fuels of non-unity Lewis numbers, especially for fuels such as hydrogen, with a Lewis number of less than one, exhibit vastly different response in flame propagation to localized stretching. The current study can be adopted, with minor modifications, for use with other gaseous fuels.

7.3.5 Developing jet modeling

Due to the modification performed, the PSC injector does not reach the fully developed, self-similar jet flow that most analytical and semi-analytical models are based on. As indicated in the present research, the entrainment mechanism in the developing jet is different from that in the fully-developed jet. They can be mathematically modeled as asymptotic limits, and the transition can be modeled based on the contributions between the two.

References

R.G. Abdel-Gayed and D. Bradley. *Combust. Flame*, 62:61–68, 1985.

R.G. Abdel-Gayed, D. Bradley, and F.K.K. Lung. *Combust. Flame*, 76:213–218, 1989.

S.F. Ahmed and E. Mastorakos. *Combust. Flame*, 146:215–231, 2006.

S.F. Ahmed, R. Balachandran, T. Marchione, and E. Mastorakos. *Combust. Flame*, 151:366–385, 2007.

P.G. Aleiferis, A.M.K.P. Taylor, K. Ishii, and Y. Urata. *Combust. Flame*, 136:283–302, 2003.

P.G. Aleiferis, A.M.K.P. Taylor, K. Ishii, and Y. Urata. *Proc. IMechE.*, 218(D):411–425, 2004.

T. Alger, B. Mangold, D. Mehta, and C. Roberts. SAE 2006-01-0224, 2006.

R.F. Alvani and M. Fairweather. *Trans. IChemE.*, 80(A):917–923, 2002.

L. Andreassi, S. Cordiner, V. Mulone, C. Reynolds, and R.L. Evans. SAE NA 2003-01-44, 2003a.

L. Andreassi, S. Cordiner, and V. Rocco. *Int. J. Engine Res.*, 4(3):179–192, 2003b.

L. Andreassi, S. Cordiner, V. Mulone, C. Reynolds, and R.L. Evans. ASME ICEF2004-912, 2004.

V.S. Arpaci, Y. Ko, M.T. Lim, and H.S. Lee. *Combust. Flame*, 135:315–312, 2003.

C.P. Barrington-Leigh. PhD thesis, Stanford, 2000.

R.J.M. Bastiaans, J.A.M. de Swart, J.A. van Oijen, and L.P.H. de Goey. *LNCS*, 56:371–383, 2007.

E.M. Bazelyan and Yu.P. Paizer. *Spark discharge*. CRC, 1998.

J.-L. Beduneau, B. Kim, L. Zimmer, and Y. Ikeda. *Combust. Flame*, 132:653–665, 2003.

A. Bentebbiche, K. Bouhadef, D. Veynante, and E. Esposito. *Forsch. Ingenieurwes*, 69:236–245, 2005.

A.D. Birch, D.R. Brown, and M.G. Dodson. *Proc. Combust. Inst.*, 18:1755–1780, 1981.

A.D. Birch, D.R. Brown, M.G. Dodson, and F. Swaffield. *Combust. Sci. Tech.*, 36:249–261, 1984.

D. Bradley, M. Lawes, M.J. Scott, and E.M.J. Mushi. *Combust. Flame*, 99:581–590, 1994.

K.N.C. Bray. CUED / A-Thermo / TR. 32, Cambridge, 1990.

B.S. Brown and J. Veliath. Personal communication, 2008.

G. Brown. Master's thesis, UBC, 2003.

J.F. Canny. *IEEE Trans. Pattern Anal. Mach. Intell.*, 8(6):679–698, 1986.

J. Chakraborty, E. Mastorakos, and R.S. Cant. *Combust. Sci. Tech.*, 179(1-3):293–317, 2007.

E.C. Chan, R.L. Evans, M.H. Davy, and S. Cordiner. SAE 2007-1-1913, 2007.

E.C. Chan, M.H. Davy, G. de Simone, and V. Mulone. *J. Eng. Gas Turbines Power*, 133:To be published, 2011.

Z. Chen and Y. Ju. *Combust. Theor. Model.*, 11(3):427–453, 2007.

A. Chepakovich. Master's thesis, UBC, 1993.

S.H. Chung and C.K. Law. *Combust. Flame*, 72:325–336, 1988.

S.S. Chung, J.Y. Hua, J.S. Park, M.J. Lee, and J.K. Yeom. SAE 2003-01-3212, 2003.

G.E. Cossali, A. Coghe, and L. Araneo. *AIAA J.*, 39(6):1113–1122, 2001.

J. Cox. Personal communication, 2009.

C. Crigorescu, N. Petkov, and M.A. Westenberg. *Image Vision Comput.*, 22:609–622, 2004.

J.D. Dale and A.K. Oppenheim. SAE 810146, 1981.

C.F. Daniels and B.M. Scilzo. SAE 960606, 1996.

D. Dardalis, R.D. Matthews, D. Lewis, and K. Davis. SAE 982447, 1998.

G. de Simone. Master's thesis, Uni. Roma II, 2008.

B. Deshaies and G. Joulin. *Combust. Sci. Tech.*, 37:99–116, 1984.

A.L. Dicks. *J. Power Sources*, 61:113–124, 1996.

G.G. Dober and H.C. Watson. SAE 2000-01-1263, 2000.

E. Eckermann and P.L. Albrecht. *World history of the automobile.* SAE, 2001.

E. Effelsberg and N. Peters. *Combust. Flame*, 50:351–360, 1983.

D.A. Eichenberger and W.L. Roberts. *Combust. Flame*, 118:469–478, 1999.

O. Ekici, O.A. Ezekoye, M.J. Hall, and R.D. Matthews. *J. Fluids Eng.*, 129:55–65, 2007.

I.S. Ertesvåg and B.F. Magnussen. *Combust. Sci. Tech.*, 159:213–235, 2000.

R.L. Evans. US Patent 6032640, 2000.

R.L. Evans. *Int. J. Environ. Stud.*, 63(4):441–452, 2006.

L. Fan and R.D. Reitz. SAE 2000-01-2809, 2000.

Z. Gete. Master's thesis, UBC, 1991.

L. Gillespie, M. Lawes, C.G.W. Sheppard, and R. Woolley. SAE 2000-01-0192, 2000.

I. Glassman. *Combustion*. Academic Press, 1996.

R.C. Gonzalez and R.E. Woods. *Digital image processing*. Prentice Hall, 2002.

D.G. Goodwin. Cantera 1.7.0. CalTech, 2007.

D.D. Gorby. Master's thesis, UBC, 2007.

X. Gu, M.Z. Haq, M. Lawes, and R. R. Woolley. *Combust. Flame*, 121:41–58, 2000.

J. Hacochen, M.R. Belmont, J.C. Thomas, and R. Thurley. SAE 932717, 1993.

R. Herweg and R.R. Maly. SAE 922243, 1992.

J.B. Heywood. *Internal combustion engine fundamentals*. McGraw-Hill, 1988.

B.J. Hill. *J. Fluid Mech.*, 51(4):773–779, 1972.

C.M. Ho and D.A. Santavicca. SAE 872100, 1987.

K. Hotta, Y. Yoshikawa, K. Okuma, O. Moriue, and E. Murase, 2007.

K.W. Jenkins, M. Klein, N. Chakraborty, and R.S. Cant. *Combust. Flame*, 145:415–434, 2006.

B. Johansson, H. Neij, M. Aldén, and G. Julhlin. SAE 950108, 1995.

G. Jomaas, C.K. Law, and J.K. Bechtold. *J. Fluid Mech.*, 583:1–26, 2007.

G.T. Kalghatgi. *Combust. Flame*, 60:299–308, 1985.

M. Kettner, J. Fischer, A. Nauwerck, J. Tribulowski, U. Spicher, and A. Velji. SAE 2004-01-0035, 2004.

W. Khan. Reduction of emissions from 2-3 wheelers. Asian Development Bank, 2001.

S.R. King. SAE 920593, 1992.

G. Kolb. *Fuel processing for fuel cells*. Wiley-VCH, 2008.

T. W. Kuo and R.D. Reitz. SAE 920425, 1992.

G. Lacaze, B. Cuenot, T. Poinsot, and M. Oschwald. *Combust. Flame*, 156:1166–1180, 2009a.

G. Lacaze, E.S. Richardson, and T. Poinsot. *Combust. Flame*, 156:1993–2009, 2009b.

L.D. Landau. *Acta Physicochim. URSS*, 19:77–85, 1944.

C.K. Law. *Reduced kinetic mechanisms for applications in combustion systems.* Springer, 1993.

C.K. Law. *Combustion physics.* 2006.

C.K. Law, D.L. Zhu, and G. Yu. *Symp. (Int.) Combust.*, 21:1419–1426, 1986.

J. Lawrence and H.C. Watson. SAE 980044, 1998.

A. Liñán and F.A. Williams. *Fundamental aspects of combustion.* Oxford, 1993.

A.N. Lipatnikov and J. Chomiak. *Prog. Energy Combust. Sci.*, 28:1–74, 2002.

J.-M.S. Logan. Master's thesis, UBC, 2010.

J.X. Ma, D.R. Alexander, and D.E. Poulain. *Combust. Flame*, 112:492–506, 1998.

B.F. Magnussen. In *ECCOMAS Thematic Conf. Comput. Combust.*, 2005.

B.F. Magnussen and B.H. Hjertager. *Symp. (Int.) Combust.*, 16:719–729, 1976.

S. Maji, P.B. Sharma, and M.K.G. Babu. SAE 2004-28-0038, 2004.

R.R. Maly. *Fuel economy*, chapter Spark ignition. Plenum, 1984.

C. Mandilas, M.P. Ormsby, C.G.W. Sheppard, and R. Woolley. *Proc. Combust. Inst.*, 31:1443–1450, 2007.

T.T. Maxwell and J.C. Jones. *Alternative fuels.* SAE, 1995.

B.J. McBride, S. Gordon, and M.A. Reno. NASA TM-4513, 1993.

G.P. McTaggart-Cowan. PhD thesis, UBC, 2006.

M. Metghalchi and J.C. Keck. *Combust. Flame*, 38:143–154, 1980.

A.Z. Mezo. Master's thesis, UBC, 2008.

A.Z. Mezo, M.H. Davy, and R.L. Evans. In *CI/CS Spring Technical Meeting*, 2008.

N. Muradov. *J. Power Sources*, 118:320–324, 2003.

E. Murase, S. Ono, K. Hanada, and A.K. Oppenheim. SAE 942048, 1994.

G.P. o'Hara. *US Gov. Rep. Announce. Index*, 84(11):129–149, 1984.

S. Osher and J.A. Sethian. *J. Comput. Phys.*, 79:12–49, 1988.

P. Ouellette. PhD thesis, UBC, 1996.

P. Ouellette and P.G. Hill. *ASME J. Fluids Eng.*, 122:743–752, 2000.

N. Ozdor, M. Dulger, and E. Sher. SAE 940987, 1994.

A. Parisini. Master's thesis, Uni. Roma II, 2008.

F. Paschen. *Ann. Phys.*, 273(5):69–75, 1889.

B.D. Peters and G.L. Borman. SAE 700064, 1970.

B.D. Peters and A.A. Quader. SAE 780234, 1978.

N. Peters. *Turbulent combustion*. Cambridge, 2000.

N. Peters and B. Rogg. *Reduced kinetic mechanisms for applications in combustion systems*. Springer, 1993.

T. Poinsot and D. Veynante. *Theoretical and numerical combustion*. R.T. Edwards, 2001.

S.B. Pope. *AIAA J.*, 16(3):279–281, 1978.

S.B. Pope. *Combust. Theor. Model.*, 1:41–63, 1997.

S.B. Pope. *Turbulent flows*. Cambridge, 2000.

E.P. Popov. *Engineering mechanics of solids*. Prentice Hall, 1990.

S.V. Poroseva and H. Bézard. *CFD J.*, 2001:627–633, 1999.

A. Prieur and R. Tilagone. SAE 007-01-0037, 2007.

C. Reynolds. Master's thesis, UBC, 2001.

C. Reynolds and R.L. Evans. *Int. J. Engine Res.*, 5(1):105–114, 2004a.

C. Reynolds and R.L Evans. In *CI/CS Spring Technical Meeting*, 2004b.

C.C.O. Reynolds, R.L. Evans, L. Andreassi, V. Mulone, and S. Cordiner. SAE 2005-01-0247, 2005.

E.S. Richardson and E. Mastorakos. *Combust. Sci. Tech.*, 179(1-2):21–37, 2007.

F.B. Ricou and D.B. Spalding. *J. Fluid Mech.*, 11:21–32, 1961.

Robert Bosch GmbH. *Automotive handbook, 7. Ed.* Wiley, 2007.

C. Robinet, P. Higelin, B. Moreau, O. Pajot, and J. Andrzejewski. SAE 1999-01-062, 1999.

P.J. Rubas, M.A. Paul, G.C. Martin, R.E. Coverdill, R.P. Lucht, J.E. Peters, and K.A. DelVecchio. SAE 980143, 1998.

R. Sangras, O.C. Kwon, and G.M. Faeth. *J. Heat Transfer*, 124:460–469, 2002.

R.R. Saraf, S.S. Thipse, and P.K. Saxena. SAE 2008-32-0024, 2008.

G.S. Settles. *Schlieren and shadowgraph techniques.* Springer, 2001.

L.G. Shapiro and G.C. Stockman. *Computer vision.* Prentice Hall, 2002.

G.P. Smith, D.M. Golden, M. Frenklach, N.W. Moiarty, B. Eiteneer, M. Goldenberg, C.T. Bowman, R.K. Hanson, S.H. Song, W.C. Gardiner, V.V. Lissianski, and Z. Qin. GRI-Mech 3. 0. U.C. Berkeley, 1999.

M.T.E. Smith, A.D. Birch, D.R. Brown, and M. Fairweather. *Proc. Combust. Inst.*, 21:1403–1408, 1986.

M.D. Smooke. *Reduced kinetic mechanisms and asymptotic approximations for methane-air flames.* Springer, 1991.

J.H. Song and M.G. Sunwoo. SAE 2000-01-0960, 2000.

F.G. Spreadbury. *Electrical ignition equipment.* Constable & Co., 1954.

S.M. Starikovskaia, E.N. Kukaev, A.Yu. Kuksinand M.M. Nudnova, and A.Yu. Starikovskii. *Combust. Flame*, 139:177–187, 2004.

H. Tagare and R.J.P. Figueiredo. *IEEE Trans. Pattern Anal. Mach. Intell.*, 12(12):1186–1190, 1990.

Z. Tan and R.D. Reitz. *Combust. Flame*, 145:1–15, 2006.

G.I. Taylor. *Proc. R. Soc. London, Ser. A*, 164:546, 1938.

M. Thiele, J. Warnatz, A. Dreizler, S. Lindenmaier, R. SchießL, U. Maas, A. Grant, and P. Ewart. *Combust. Flame*, 128:74–87, 2002.

J.F. Thomas and R.H. Staunton. SAE 1999-01-1511, 1999.

D.S.K. Ting and M.D. Checkel. *J. Eng. Gas Turbines Power*, 123:175–181, 2001.

J.S. Turner. *J. Fluid Mech.*, 13:356–368, 1963.

M. Umiersky and B. Hüchtebrock. SAE NA 2003-01-45, 2003.

C.M. Vagelopoulos, F.N. Egolfopoulous, and C.K. Law. *Symp. (Int.) Combust.*, 25:1341–1347, 1994.

C. Vázquez-Espí and A. Liñán. *Combust. Theor. Model.*, 6(2):297–315, 2002.

J.S. Wallace. SAE 892144, 1989.

S.-F. Wang, H. Zhang, J. Jarosinki, A. Gorczakowski, and J. Podfilipski. *Combust. Flame*, 157: 667–675, 2010.

C.S. Weaver. SAE 892133, 1989.

F.J. Weinberg. *Optics of flames.* Butterworths, 1963.

C.M. White, R. R. Steeper, and A. E. Lutz. *Int. J. Hydrogen Energy*, 31:1292–1305, 2006.

K.A. Whitney and B. K. Bailey. SAE 941903, 1994.

D.H. Williams and R.L. Evans. In *CI/CS Spring Technical Meeting*, 2006.

WLPGA. *Statistical review of global LP gas*. World LP Gas Association, 2007.

N. Wu. Personal communication, 2009.

O. Yaşar. *ICCS LNCS*, 2073:1147–1155, 2001.

Y. B. Zel'dovich, G. I. Barenblatt, B.V. Librovich, and G. M. Makhviladze. *Mathematical theory of combustion and explosions*. Plenum, 1984.

V. L. Zimont and A. N. Lipatnikov. *Chem. Phys. Rep.*, 14(7):993–1025, 1995.

Appendix A

The Constant volume combustion chamber

The constant volume combustion chamber (CVCC) was commissioned in December 2007 to investigate the enabling mechanisms of the partially stratified charge (PSC) injection / ignition strategy. The idealized PSC configuration (Section 3.1) was adopted in order to eliminate geometry-dependent effects, such as impingement and recirculation, that would result from using a regular spark plug. The design phase took place between January to May 2008. The final design as was approved by Prof. R.L. Evans in June 2008. Geometric dimensioning and tolerancing (GD&T) were performed at the discretion Mr. M. Fengler.

The construction phase begin in July 2008, under the care of machinist Mr. R. Genschorek. Mr. J.-M.S. Logan and the author participated in the fabrication of non-critical components, and minor modifications to accommodate additional visualization experiments. The quartz windows were supplied by Rainbow Research Optics. All parts for the CVCC were ready by November, 2008. With other experimental components became operational in August 2009, particularly the electronic and data acquisition systems, baseline tests were subsequently conducted.

The following pages contain the construction plan for the CVCC, dated July 15, 2008, which includes an assembly view, as well as the plans for all the individual components. The author would also like to thank Mr. R. Parry of CERC, as well as Mr. H. Schremp of UBC civil engineering, for their valuable opinions.

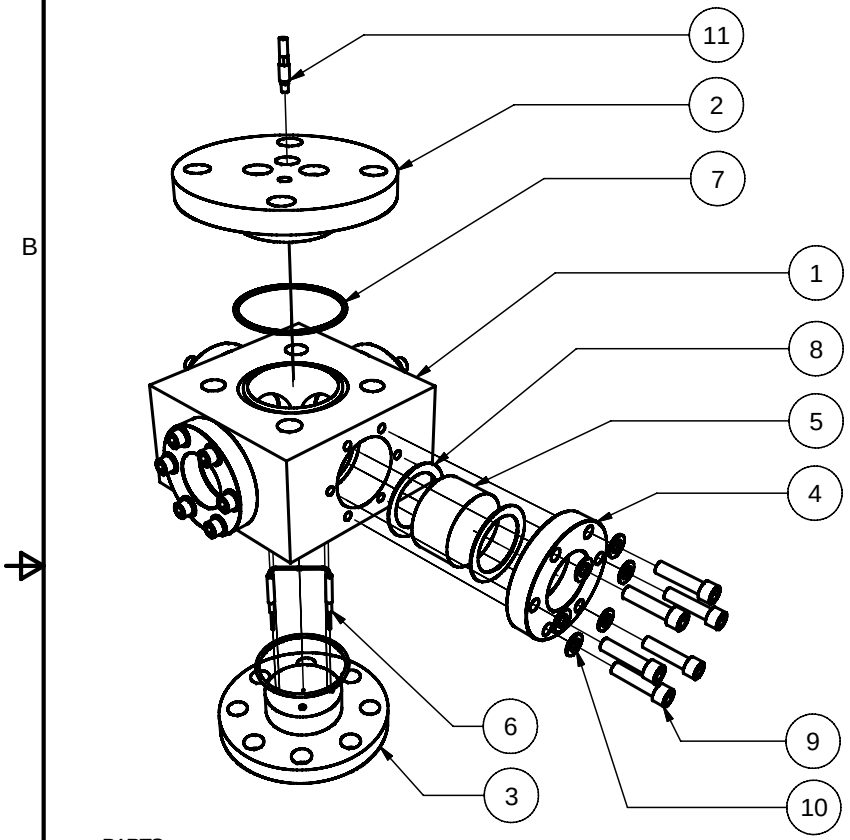

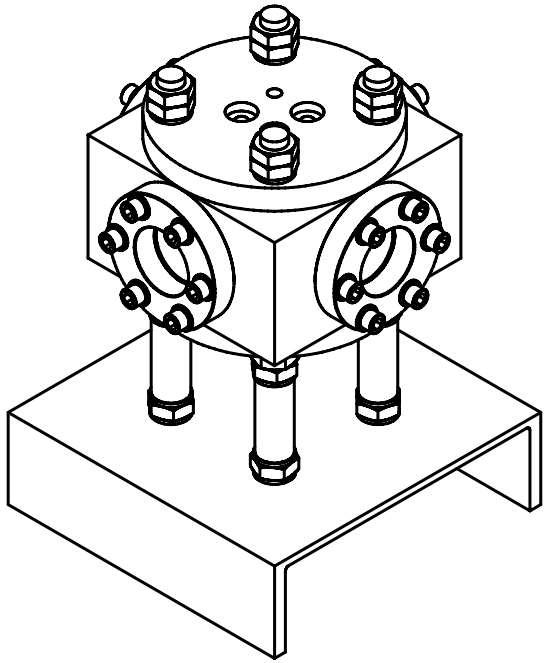

Assembled view with mounting bracket

PARTS

(1) Combustion chamber proper (see drawing 1)
(2) Instrumentation flange (see drawing 2)
(3) PSC flange (see drawing 3)
(4) Quartz window flange (see drawing 4)
(5) Quartz window (Ø65mm x 38mm)
(6) PEEK insulated tungsten electrodes
(7) O-ring AS568B-238
(8) Silicon rubber gasket (1.6mm thickness)
(9) Hex cap screw 3/8-16
(10) Washer for 3/8 screws
(11) Piezoelectric pressure transducer PCB 112A05

DRAWN ECC	10/06/2008	UBC - CLEAN ENERGY RESEARCH CENTER
CHECKED		
QA		TITLE
MFG		CONSTANT VOLUME COMBUSTION CHAMBER
APPROVED		SIZE A / DWG NO CVCC - OVERALL ASSEMBLY / REV
		SCALE / SHEET 1 OF 1

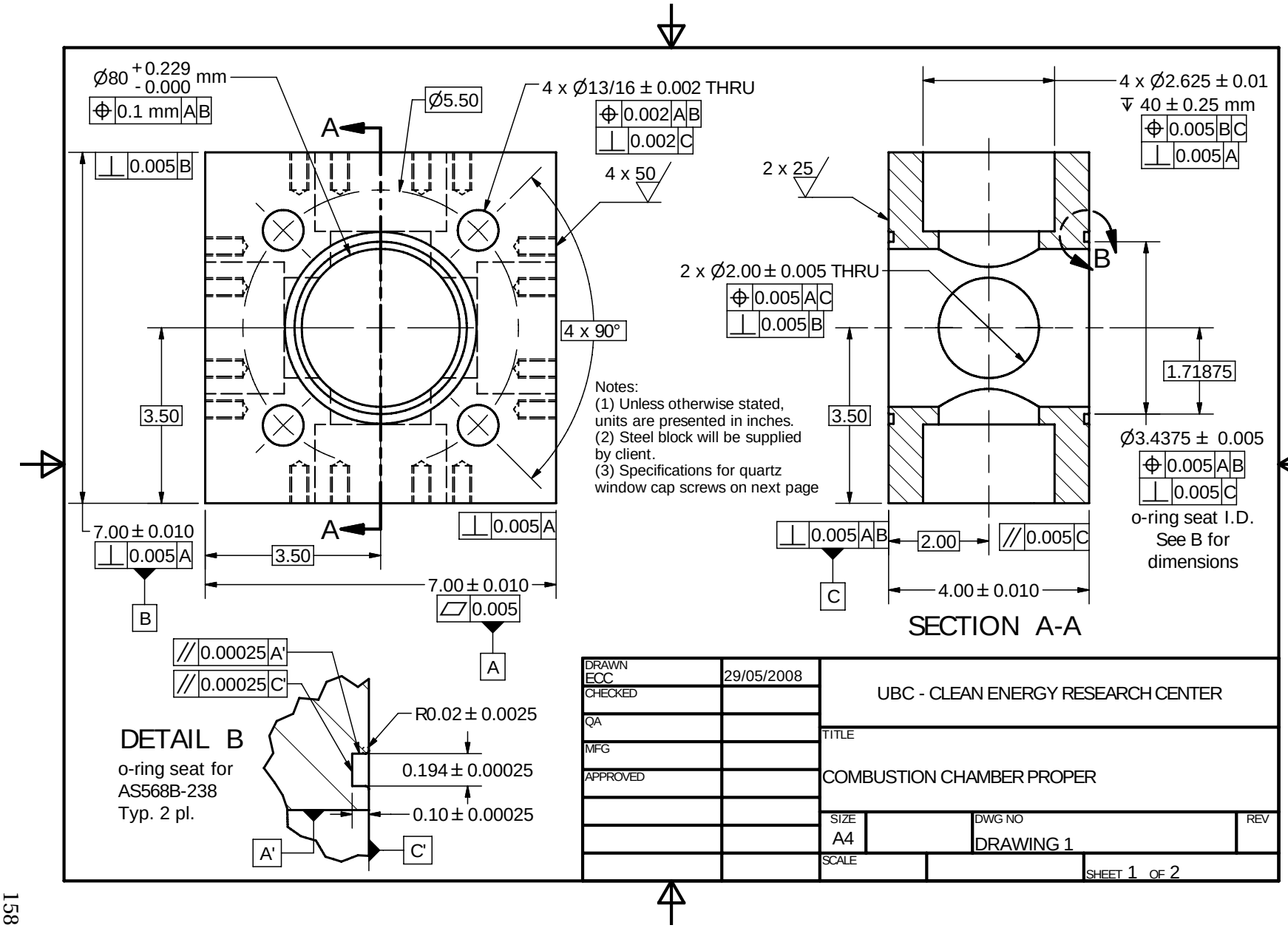
Ø80 +0.229 -0.000 mm
⌖ 0.1 mm A B
Ø5.50
4 x Ø13/16 ± 0.002 THRU
⌖ 0.002 A B
⊥ 0.002 C
4 x 50
⊥ 0.005 B
4 x 90°
3.50
7.00 ± 0.010
⊥ 0.005 A
B
3.50
7.00 ± 0.010
⊥ 0.005 A
⊥ 0.005 A
A
A
Notes:
(1) Unless otherwise stated, units are presented in inches.
(2) Steel block will be supplied by client.
(3) Specifications for quartz window cap screws on next page
4 x Ø2.625 ± 0.01
↧ 40 ± 0.25 mm
⌖ 0.005 B C
⊥ 0.005 A
2 x 25
2 x Ø2.00 ± 0.005 THRU
⌖ 0.005 A C
⊥ 0.005 B
B
1.71875
3.50
Ø3.4375 ± 0.005
⌖ 0.005 A B
⊥ 0.005 C
o-ring seat I.D.
See B for
dimensions
⊥ 0.005 A B
C
2.00
// 0.005 C
4.00 ± 0.010
SECTION A-A
// 0.00025 A'
// 0.00025 C'
R0.02 ± 0.0025
0.194 ± 0.00025
0.10 ± 0.00025
A'
C'
DETAIL B
o-ring seat for
AS568B-238
Typ. 2 pl.
DRAWN ECC 29/05/2008
CHECKED
QA
MFG
APPROVED
UBC - CLEAN ENERGY RESEARCH CENTER
TITLE
COMBUSTION CHAMBER PROPER
SIZE A4
DWG NO DRAWING 1
REV
SCALE
SHEET 1 OF 2

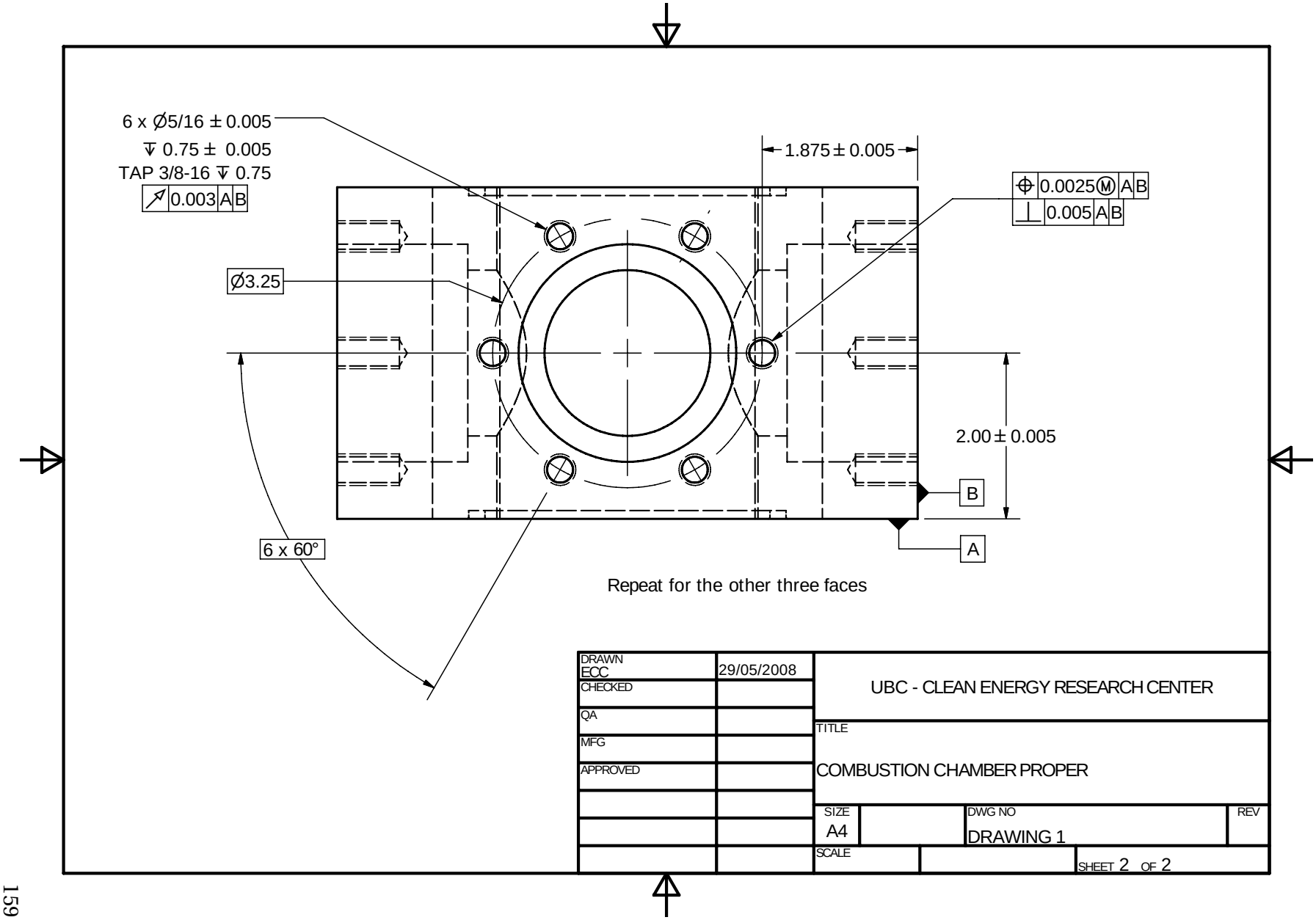
6 x Ø5/16 ± 0.005
↧ 0.75 ± 0.005
TAP 3/8-16 ↧ 0.75
0.003 A B
1.875 ± 0.005
0.0025 Ⓜ A B
0.005 A B
Ø3.25
2.00 ± 0.005
B
A
6 x 60°
Repeat for the other three faces
DRAWN ECC 29/05/2008
CHECKED
QA
MFG
APPROVED
UBC - CLEAN ENERGY RESEARCH CENTER
TITLE
COMBUSTION CHAMBER PROPER
SIZE A4
DWG NO DRAWING 1
REV
SCALE
SHEET 2 OF 2

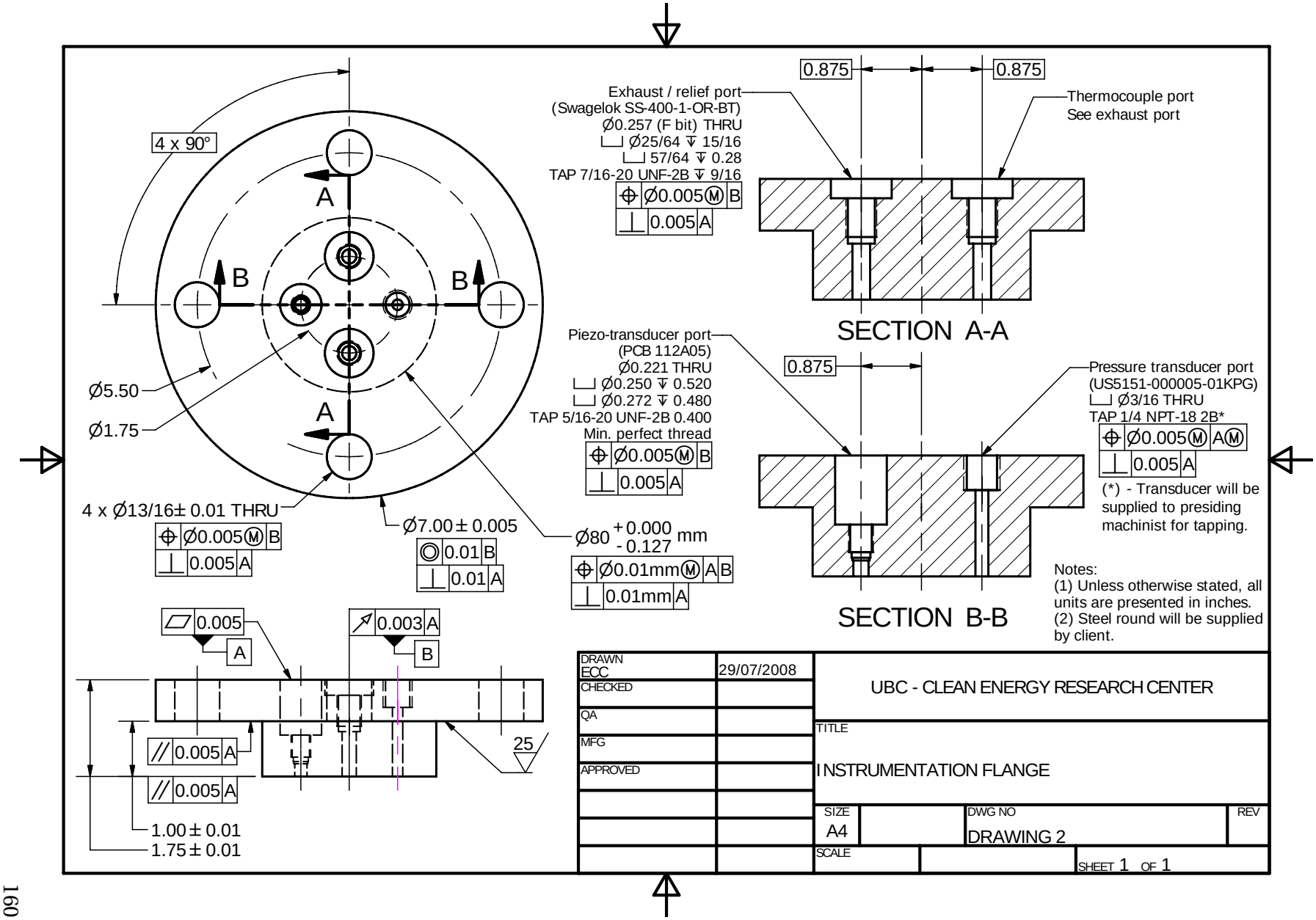
4 x 90°
A
B
B
A
Ø5.50
Ø1.75
4 x Ø13/16± 0.01 THRU
Ø0.005 M B
0.005 A
Ø7.00 ± 0.005
0.01 B
0.01 A
Ø80 +0.000 -0.127 mm
Ø0.01mm M A B
0.01mm A
Exhaust / relief port
(Swagelok SS-400-1-OR-BT)
Ø0.257 (F bit) THRU
⌴ Ø25/64 ↧ 15/16
⌴ 57/64 ↧ 0.28
TAP 7/16-20 UNF-2B ↧ 9/16
Ø0.005 M B
0.005 A
0.875
0.875
Thermocouple port
See exhaust port
SECTION A-A
Piezo-transducer port
(PCB 112A05)
Ø0.221 THRU
⌴ Ø0.250 ↧ 0.520
⌴ Ø0.272 ↧ 0.480
TAP 5/16-20 UNF-2B 0.400
Min. perfect thread
Ø0.005 M B
0.005 A
0.875
Pressure transducer port
(US5151-000005-01KPG)
⌴ Ø3/16 THRU
TAP 1/4 NPT-18 2B*
Ø0.005 M A M
0.005 A
(*) - Transducer will be supplied to presiding machinist for tapping.
SECTION B-B
Notes:
(1) Unless otherwise stated, all units are presented in inches.
(2) Steel round will be supplied by client.
0.005 A
0.003 A B
0.005 A
0.005 A
25
1.00 ± 0.01
1.75 ± 0.01
DRAWN ECC 29/07/2008
CHECKED
QA
MFG
APPROVED
UBC - CLEAN ENERGY RESEARCH CENTER
TITLE
INSTRUMENTATION FLANGE
SIZE A4
DWG NO DRAWING 2
REV
SCALE
SHEET 1 OF 1

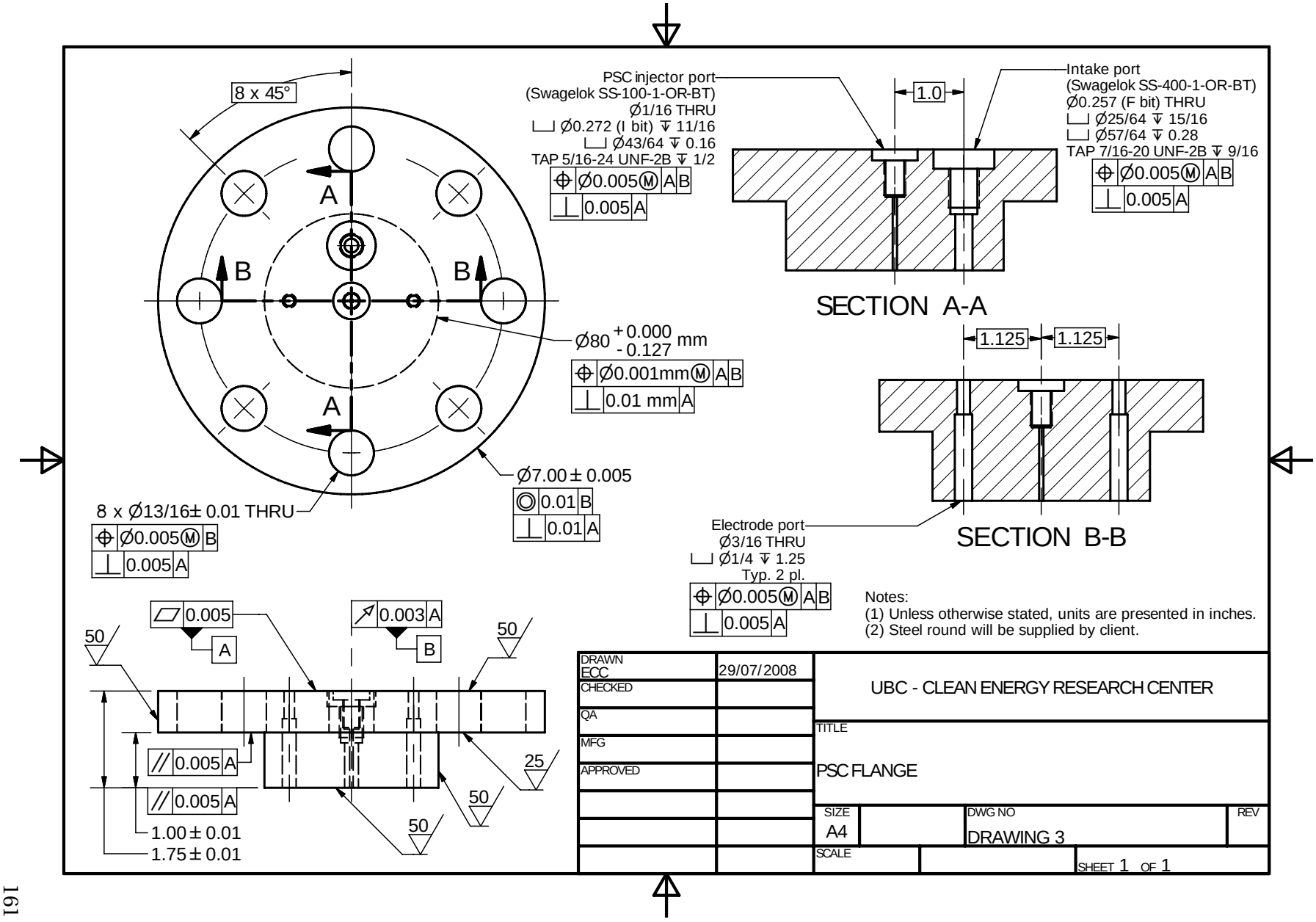
8 x 45°
A
B
B
A
PSC injector port
(Swagelok SS-100-1-OR-BT)
Ø1/16 THRU
⌴ Ø0.272 (I bit) ↧ 11/16
⌴ Ø43/64 ↧ 0.16
TAP 5/16-24 UNF-2B ↧ 1/2
⌖ Ø0.005Ⓜ A B
⊥ 0.005 A
Intake port
(Swagelok SS-400-1-OR-BT)
Ø0.257 (F bit) THRU
⌴ Ø25/64 ↧ 15/16
⌴ Ø57/64 ↧ 0.28
TAP 7/16-20 UNF-2B ↧ 9/16
⌖ Ø0.005Ⓜ A B
⊥ 0.005 A
1.0
SECTION A-A
Ø80 +0.000 -0.127 mm
⌖ Ø0.001mmⓂ A B
⊥ 0.01 mm A
1.125
1.125
SECTION B-B
Ø7.00 ± 0.005
◎ 0.01 B
⊥ 0.01 A
8 x Ø13/16± 0.01 THRU
⌖ Ø0.005Ⓜ B
⊥ 0.005 A
Electrode port
Ø3/16 THRU
⌴ Ø1/4 ↧ 1.25
Typ. 2 pl.
⌖ Ø0.005Ⓜ A B
⊥ 0.005 A
Notes:
(1) Unless otherwise stated, units are presented in inches.
(2) Steel round will be supplied by client.
0.005 A
0.003 A
50
50
25
50
50
// 0.005 A
// 0.005 A
1.00 ± 0.01
1.75 ± 0.01
DRAWN ECC 29/07/2008
CHECKED
QA
MFG
APPROVED
UBC - CLEAN ENERGY RESEARCH CENTER
TITLE
PSC FLANGE
SIZE A4
DWG NO DRAWING 3
REV
SCALE
SHEET 1 OF 1

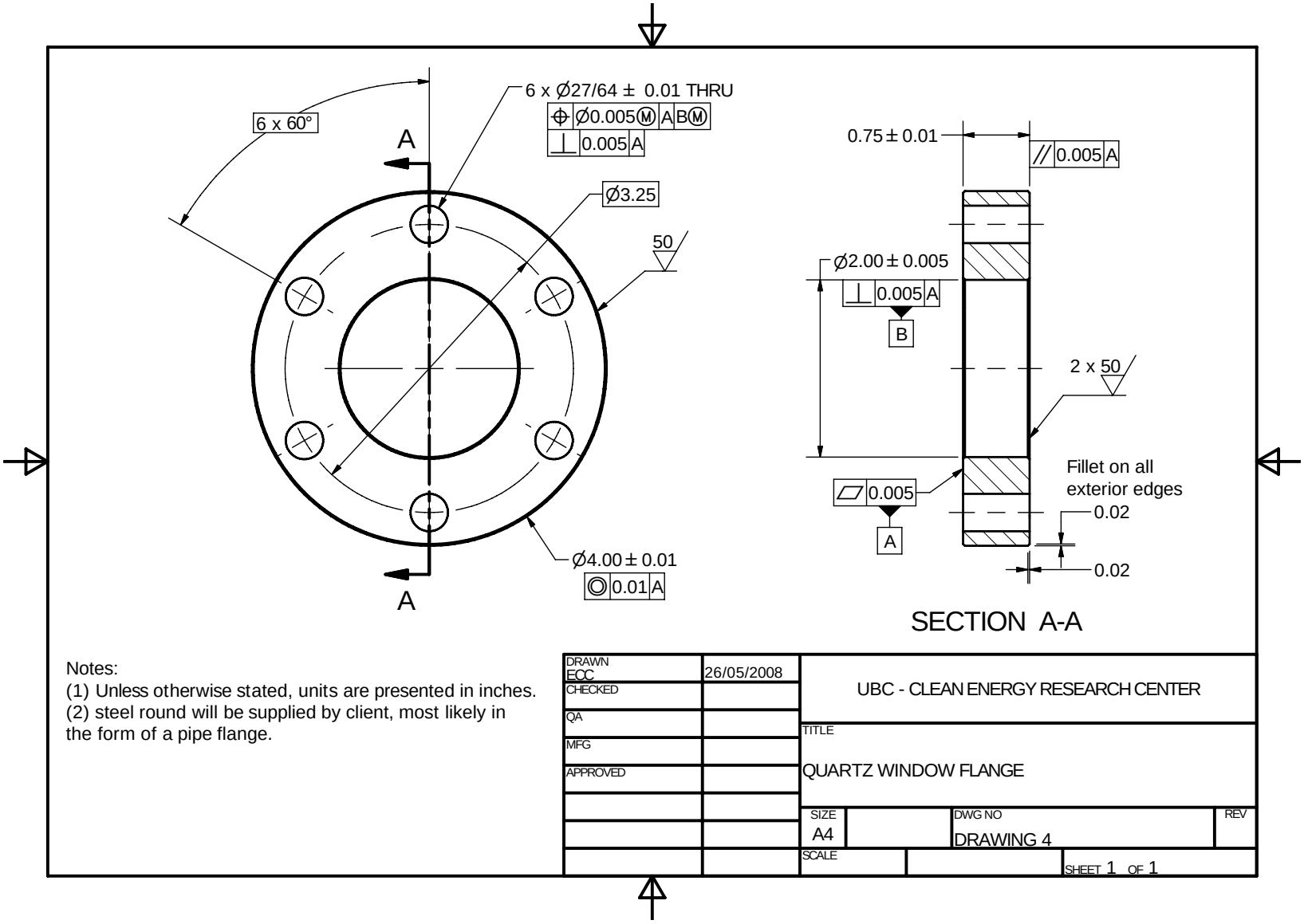

Notes:
(1) Unless otherwise stated, units are presented in inches.
(2) steel round will be supplied by client, most likely in the form of a pipe flange.

DRAWN ECC	26/05/2008	UBC - CLEAN ENERGY RESEARCH CENTER
CHECKED		
QA		TITLE: QUARTZ WINDOW FLANGE
MFG		
APPROVED		SIZE A4 | DWG NO DRAWING 4 | REV
		SCALE | SHEET 1 OF 1

Appendix B

Finite element analysis of CVCC components

A finite element analysis was performed on the quartz and body components of the CVCC to verify the strength of the finished product, to ensure a safe design. The model was performed using the commercial FEA package ANSYS due to its flexibility in mesh control and availability of higher-order finite elements. Second-order triangular (2D, 6-node) and tetrahedral (3D, 10-node) were used throughout. Effects of temperature on material properties are expected to be negligible, and therefore not included in the analysis. It was found that, while the metallic parts could easily handle 300 bars of internal pressure, the quartz disc would rupture at about 240 bar, obtained by scaling between the two load scenarios. With an expected operating pressure of 40 bar, the incident pressures considered represent a more-than-healthy factor of safety. Thus, based on the finite element model results, the CVCC would not experience significant problems at its expected operating pressure.

B.1 Quartz window

The geometry for the quartz window, presented in Figure B.1, was used in formulating the finite element model. The problem can be effectively regarded as axisymmetric and therefore a two-dimensional analysis was performed to reduce computational effort. The material properties of fused silica (quartz) and silicone rubber are tabulated in Table B.1. Internal chamber pressures of 200 and 300 bar were applied to the model.

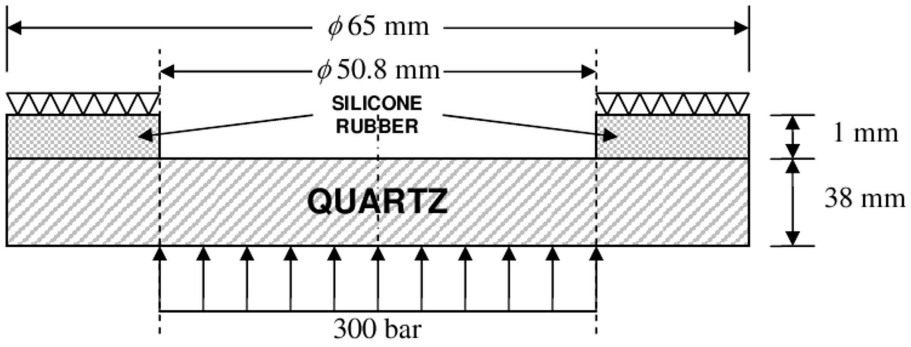

Figure B.1: Geometry of the quartz window for the finite element analysis.

Table B.1: Material properties for quartz and silicone rubber.

Property	**Fused silica**[a]	**Silicone rubber**[b]
Density	2200 kg/m^3	1320 kg/m^3
Young's modulus	72.7 GPa	89.6 - 145 MPa[c]
Poisson's ratio	0.16	0.48 - 0.49[d]
Modulus of rupture	52.4 MPa (Abraded)	–

[a]From Dow Corning literature.
[b]From o'Hara (1984).
[c]A value of 120 MPa was used for the FE analysis.
[d]A value of 0.485 was used for the FE analysis.

The stress distribution are shown in Figures B.2 and B.3, based on the Rankine (first principal stress) and von Mises (distortion energy) criteria. The peak pressures based on each criterion are also tabulated in Table B.2. The von Mises stress reported a rupture at the quartz / silicone interface with an incident pressure of 300 bar. Scaling between the two incident load cases suggested a minimum failure stress of 240 bar. The maximum displacement in the quartz window is low enough for both cases (no more than 60 microns at 300 bar), that the *elastic* deformation of the window caused no critical concern.

Table B.2: Peak stress magnitudes for the quartz window based on the Rankine and von Mises criteria.

Load	**Rankine**	**Von Mises**
200 bar	309 bar	463 bar
300 bar	463 bar	695 bar

B.2 CVCC body components

The CVCC body components consists of three parts: the combustion chamber, the cylinder flanges, and the four flanges restraining the quartz windows. An internal chamber pressure of 300 bar was applied to the model. In the model, bolt holes were idealized as displacement constraints. Further, symmetry conditions were employed to each part to reduce model size. All metallic parts were constructed with mild steel, and the property values (Table B.3) could be obtained from most text books on solid mechanics (Popov, 1990).

Table B.3: Material properties for mild steel (Popov, 1990).

Density	7850 kg/m^3
Young's modulus	210 GPa
Yield strength	250 MPa
Poisson's ratio	0.3

For the results, the von Mises stress was considered. Stress concentration was observed at the bolt holes, where the displacement constraints were prescribed. These areas could be disregarded as the bolts and washers would help distribute the stress in the vicinity. The calculated stress levels of each CVCC component laid well below the yield stress, as shown in Figures B.4 to B.6.

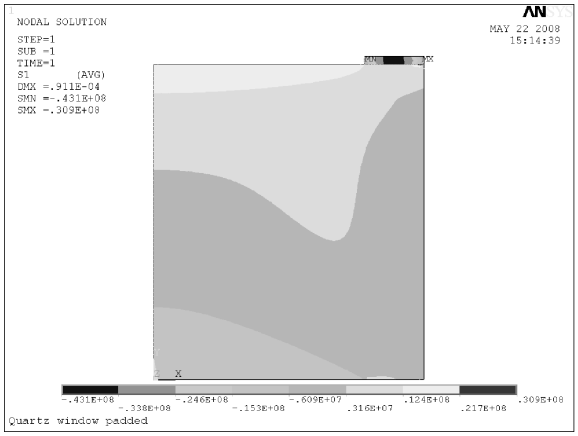

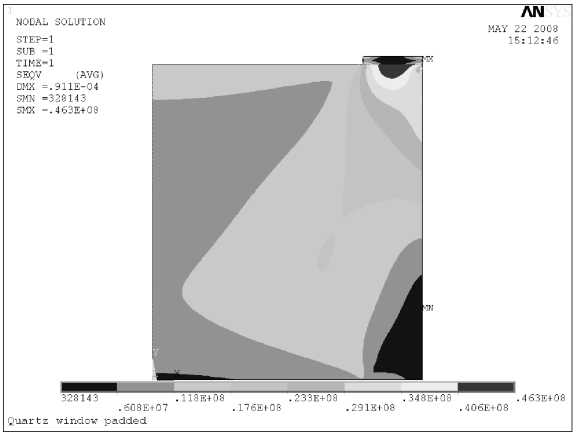

Figure B.2: Finite element results for an incident load of 200 bar. (Left) First principal stress. (Right) von Mises stress.

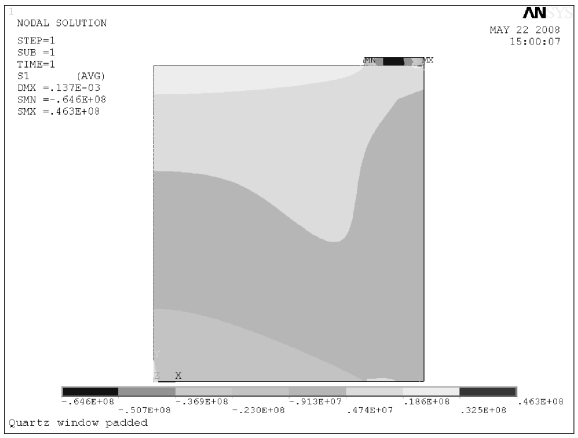

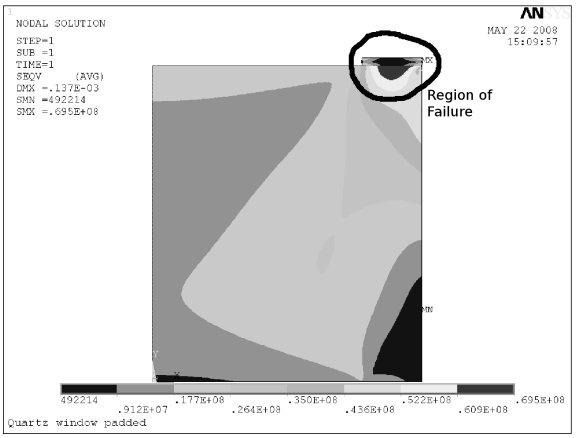

Figure B.3: Finite element results for an incident load of 300 bar. (Left) First principal stress. (Right) von Mises stress.

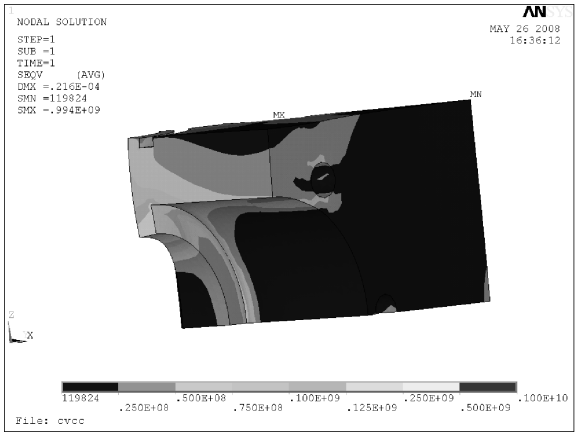

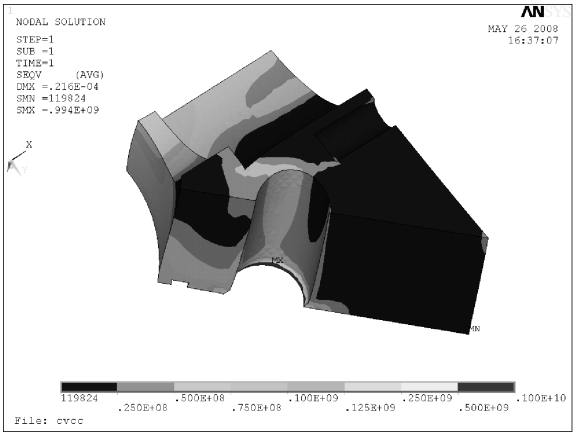

Figure B.4: Finite element analysis results of the CVCC body. (Left) Frontal view. (Right) interior mid-plane.

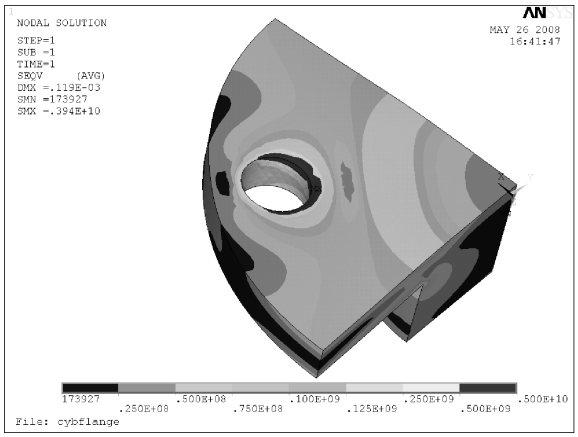

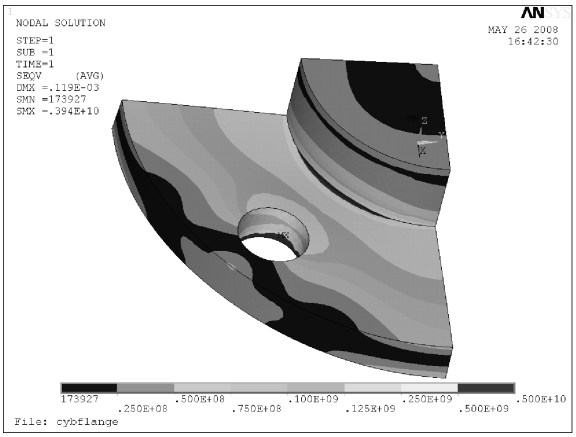

Figure B.5: Finite element analysis results of the cylinder flange. (Left) Exterior view. (Right) Interior view.

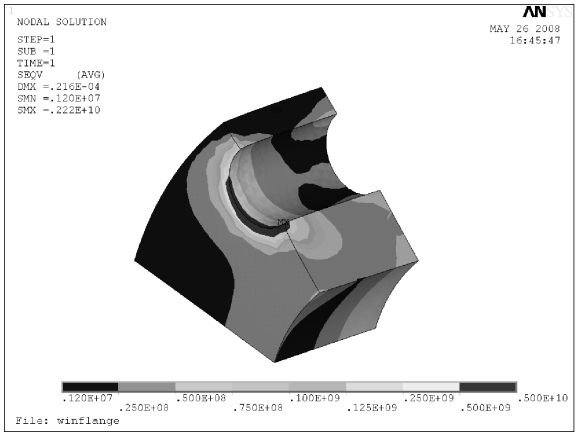

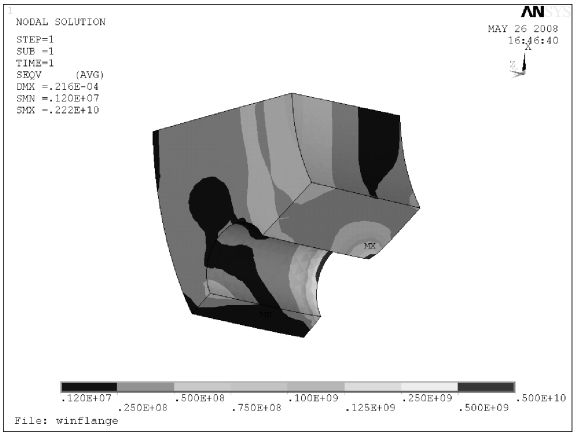

Figure B.6: Finite element analysis results of the window flange. (Left) Exterior view. (Right) Interior view.

Appendix C

Natural gas composition and summary

Determining the composition of the city natural gas supply had been a challenging issue for the UBC engine group in general, especially because the composition data was needed to calculate the molecular weight, stoichiometric air-to-fuel ratio, as well as other relevant parameters. Though sporadic data are available in theses such as Reynolds (2001), Gorby (2007), and McTaggart-Cowan (2006), recency and consistency in said data were still highly desirable. Early, short-lived, attempts were made with Brown and Veliath (2008) from Westport Innovations and Cox (2009) from Terasen Gas to obtain a history of natural gas composition. A relationship was later established with Wu (2009) from Westport Innovations to set up a daily natural gas composition database at the Clean Energy Research Centre.

Molar composition for the natural gas samples were measured using an Agilent MicroGC gas chromatographic analyzer. The table below contains the monthly average of volumetric (molar) methane content, the effective carbon and hydrogen composition representing the fuel sample. The mean molecular weight, stoichiometric ratio, and lower heating value (LHV) are also tabulated so that the energy content of the mixture can be calculated. Detailed information can be obtained directly from the database, which is currently maintained by the Clean Energy Research Centre. The author would like to acknowledge the efforts of Mr. J. Veliath from Westport Innovations for providing the gas chromatography data, and Dr. Wu Ning for facilitating their access.

Table C.1: Natural gas composition and summary.

Date	%CH_4 (vol.)	C_{eff}	H_{eff}	MW [g/mol]	$AFR_{\lambda=1}$	LHV [MJ/kg]
2007-09	0.9644	1.032	4.050	16.70	16.93	49.16
2007-10	0.9689	1.027	4.039	16.62	16.95	49.20
2007-11	0.9661	1.022	4.021	16.65	16.83	49.86
2007-12	0.9647	1.025	4.030	16.69	16.84	49.89
2008-01	0.9613	1.028	4.035	16.76	16.81	48.80
2008-02	0.9628	1.025	4.027	16.72	16.80	48.77
2008-03	0.9684	1.026	4.024	16.59	16.89	49.04
2008-04	0.9679	1.024	4.032	16.61	16.91	49.09
2008-05	0.9696	1.025	4.036	16.58	16.96	49.25
2008-06	0.9633	1.019	4.012	16.69	16.76	48.65
2008-07	0.9659	1.023	4.026	16.65	16.86	49.94
2008-08	0.9688	1.027	4.039	16.62	16.95	49.20
2008-09	0.9605	1.023	4.018	16.51	16.98	49.30
2008-10	0.9566	1.014	3.988	16.41	16.93	49.16
2008-11	0.9594	1.019	4.005	16.53	16.90	49.06
2008-12	0.9637	1.022	4.018	16.56	16.91	49.11
2009-01	0.9553	1.017	3.996	16.51	16.88	49.01
2009-02	0.9463	1.006	3.954	16.33	16.88	49.01
2009-03	0.9469	1.006	3.957	16.34	16.89	49.04
2009-04	0.9427	1.002	3.939	16.23	16.92	49.13
2009-05	0.9476	1.009	3.964	16.32	16.94	49.20
2009-06	0.9436	0.9910	3.910	16.04	16.97	49.25
2009-07	0.9418	0.9946	3.917	16.14	16.91	49.10
2009-08	0.9481	0.9991	3.938	16.20	16.93	49.15
2009-09	0.9437	0.9996	3.934	16.21	16.92	49.12
2009-10	0.9467	1.003	3.948	16.29	16.89	49.05
2009-11	0.9542	1.011	3.977	16.42	16.89	49.02
2009-12	0.9510	1.020	4.001	16.60	16.83	48.88

Appendix D

User guide for SPARK-UDF

SPARK-UDF is a spark ignition simulation program based on the kernel growth model of Tan and Reitz (2006) and the developing flame speed model of Herweg and Maly (1992). It computes the evolution of the flame kernel from the glow discharge phase (~ 1 μs) to the time it reaches maturity (~ 1 ms), the energy contained within the kernel, and the mixture composition, using local flow and thermodynamic data. The code will function as a FLUENT user-defined function (UDF) in 2-D axisymmetric or 3-D simulations, or, with minimal manipulation, a standalone executable.

The main ignition model was written in the C++ programming language, using the Cantera development framework (Goodwin, 2007), while the FLUENT UDF interface was written in the C programming language. The reaction mechanics were represented by GRI-Mech 3.0 (Smith et al., 1999), and the thermodynamic properties are calculated from the NASA database (McBride et al., 1993). SPARK-UDF was compiled with gcc and g++ on the Linux operating system, but the code can be ported to platforms where both Cantera and FLUENT are fully supported, such as Microsoft Windows and OS/X.

D.1 Program and file structure

As a standalone object oriented program, SPARK-UDF has clearly defined objects that represent segregated concepts based on physical relevance. New objects are created based on existing ones through object inclusion (as opposed to multiple inheritance) as a conservative means of

object encapsulation, thus keeping the code manageable. The relationship between all objects is illustrated in Figure D.1. Meanwhile, the program structure of SPARK-UDF as a FLUENT UDF is presented on Figure D.2. since the interface to the FLUENT UDF is written in the C programming language, special considerations must be taken to seamlessly integrate the C++ components that are pertinent to the main ignition code and Cantera. The source code is organized in a such a way that each major function group, either an object or a function, are separated into files under the corresponding names. Smaller functions are collected into single files based on functionality. The execution flow of the FLUENT UDF is monitored and maintained using global variable structures. The directory structure of SPARK-UDF is illustrated in Figure D.3.

D.2 System requirements and compilation

To run SPARK-UDF as a standalone program, a minimum of Cantera 1.7.0 must be installed with support for GRI-Mech 3.0. In addition, FLUENT 1.6.2 and above must also be installed if SPARK-UDF is to be executed as a FLUENT UDF. The appropriate environment variables for Cantera and FLUENT must also be properly configured on the system. Compilation scripts (make files) for both settings are available as part of the package.

For compiling the UDF, adjust the modifiable section of the file named `makefile` under the `./libudf/src` directory to reflect any changes in the location and version of FLUENT and Cantera. Then return to the `./libudf` directory and issue the command `make` to generate the libraries for 2-D and 3-D double-precision FLUENT simulations. Please make sure the directories `2ddp` and `3ddp` already exist in the `./libudf/lnx86` directory before compiling the libraries.

Meanwhile, the standalone executable can be generated by issuing the command `make -f Makefile.standalone` directly in the directory `./libudf/src`. The executable is called `spark`, and it requires two input files, `input.sparkudf` and `methane.sl` in the same directory for execution. The simplest way is to copy the executable file into the `./libudf` directory.

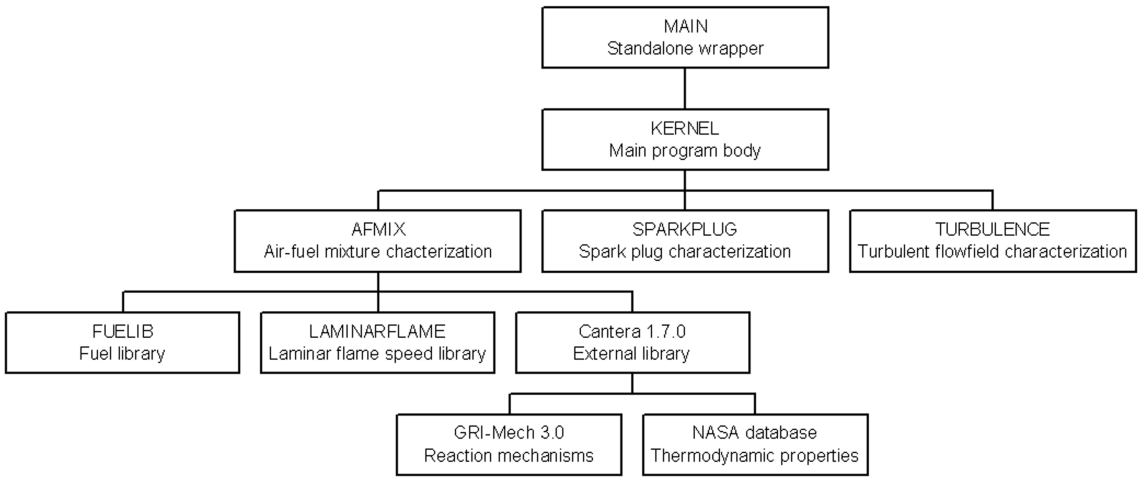

Figure D.1: Program structure of SPARK-UDF as a standalone executable.

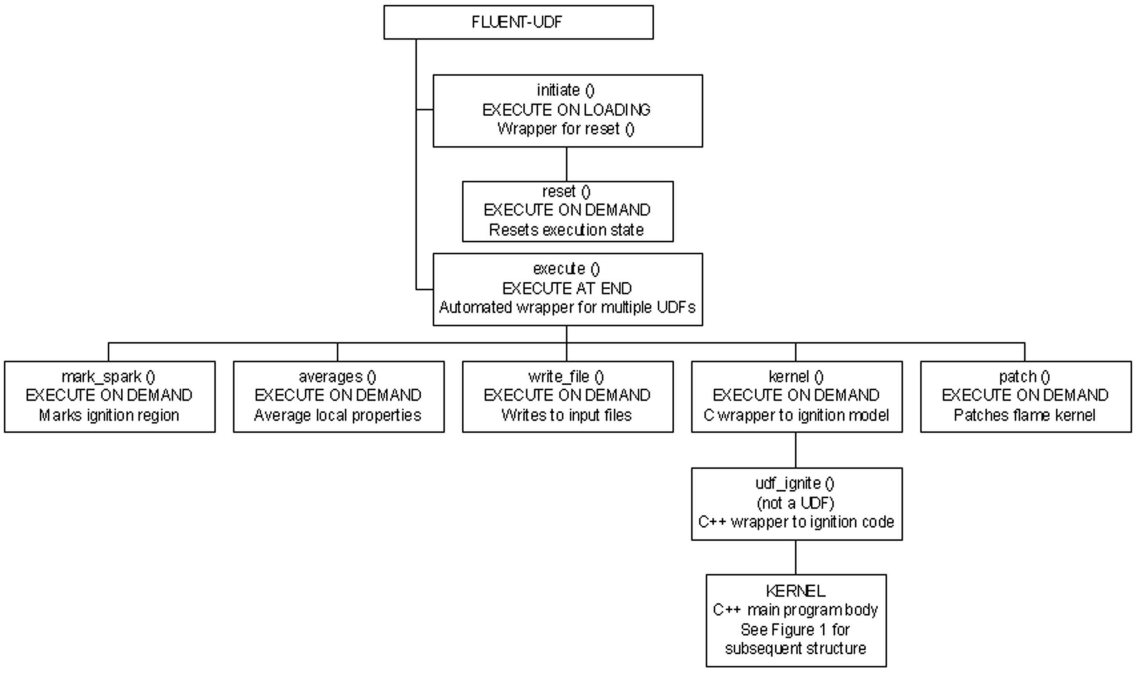

Figure D.2: Program structure of SPARK-UDF as a FLUENT UDF.

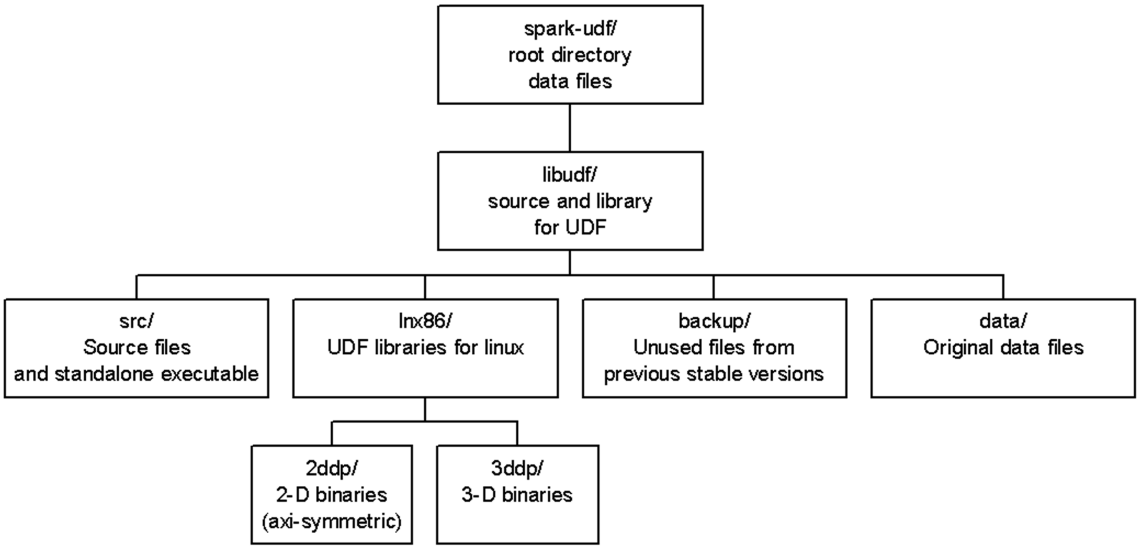

Figure D.3: Directory structure of SPARK-UDF.

D.3 Data files

The data files used in SPARK-UDF falls into three categories, which are explained below:

Input files . These files are needed for the FLUENT UDF or the standalone executable, and must be located in the `./libudf` directory. Each input file should contain sufficient explanation on each parameter:

- `udfinput.spark` : basic information on spark timing and location,
- `input.spark` : complete input parameters for the spark ignition simulation, *and*,
- `methane.sl` : tabulated flame speed library for methane.

Intermediate files . These files are either generated to communicate between FLUENT and the UDF:

- `input.sparkudf` : has the same content as *input.spark*, except it is generated by FLUENT. The standalone executable will also take this file as input, *and*,

- `output.sparkudf` : output file generated from the UDF to modify the data in the FLUENT simulation.

Output file . The only output file, `outfile.txt`, contains detailed data on the evolution of the flame kernel. It is generated from SPARK-UDF for the purpose of diagnostics and post-processing.

D.4 Basic usage

When it is used as a FLUENT UDF, SPARK-UDF must be loaded into FLUENT after opening the simulation. The library should automatically initiate. Ensure the UDF function `execute ()` is linked as an `EXECUTE_AT_END` UDF. Once the simulation is started, the ignition and patching functions will occur at the appropriate time steps. If the simulation is to be rerun in the same FLUENT session, SPARK-UDF needs be reset. This can be accomplished by manually running the `EXECUTE_ON_DEMAND` UDF called `reset ()`.

For diagnostic purposes, the ignition model can also be executed as `EXECUTE_ON_DEMAND` UDFs upon initiation of solver variables, either by initiation or by loading an existing data file. The following UDFs can be executed *in order they are presented*:

- `mark_spark()` : marks ignition region,
- `averages()` : computes locally averaged flow and thermodynamic properties,
- `write_file()` : writes the averaged quantities into an input file,
- `kernel()` : executes the ignition model, *and*,
- `patch()` : patches the ignition region with ignition model results.

Please note that SPARK-UDF can only be used with the 2-D axisymmetric or 3-D simulation problems. In addition, for axisymmetric problems, the spark location must be located along the axis of symmetry, such that only a single coordinate component is necessary. The UDF `reset` can be invoked at anytime to reset the execution state of SPARK-UDF. On the other hand, for the standalone executable, all that is required is that the two input files, namely `sinput.sparkudf` and `methane.sl` are located in the same directory as the executable `spark`, as mentioned in Section D.2.

D.5 Known problems

Even though SPARK-UDF is intended to minimize user intervention as much as humanly possible, some problems, albeit minor, are anticipated. It is hoped that these issues can be solved with improved hardware and software support*. First, a significant performance degradation was noted when the equivalence ratio (ϕ) was between 1.0 and 1.025. This is speculated to be either an equilibrium convergence issue with Cantera, or a precision issue with GRI-Mech 3.0. Should the calculated equivalence ratio fall within this range, hard-coded values was reassigned so that the equivalence ratio would be close, but still outside of this range.. No significant deviation in numerical solution was observed with the work-around.

Second, the UDF might occasionally return an `EOF on stderr` error in FLUENT when executing the main ignition code with the UDf `kernel`. This is speculated to be a memory conflict between FLUENT and the SPARK-UDF function `KERNEL::get_lhv()`, which calculates the lower heating value. As a remedy, the method in question was bypassed, and a constant value (50.1 MW/kg) had been hard-coded during code initiation. this solution was expected to have negligible effects on solution accuracy.

*At the time of writing this documentation, SPARK-UDF was developed and tested on a 700 MHz notebook PC with only 256 Mb of RAM.